RAMAN OPTICAL FREQUENCY COMB GENERATION IN HYDROGEN-FILLED

HOLLOW-CORE FIBER

by

CHUNBAI WU

A DISSERTATION

Presented to the Department of Physics
and the Graduate School of the University of Oregon
in partial fulfillment of the requirements
for the degree of
Doctor of Philosophy

December 2010

"Raman Optical Frequency Comb Generation in Hydrogen-filled Hollow-core Fiber," a dissertation prepared by Chunbai Wu in partial fulfillment of the requirements for the Doctor of Philosophy degree in the Department of Physics. This dissertation has been approved and accepted by:

_____

Dr. Steven van Enk, Chair of the Examining Committee

_____

Date

Committee in Charge: Dr. Steven van Enk, Chair
                             Dr. Michael G. Raymer
                             Dr. Daniel A. Steck
                             Dr. David M. Strom
                             Dr. Andrew H. Marcus

Accepted by:

_____

Dean of the Graduate School

An Abstract of the Dissertation of

Chunbai Wu   for the degree of   Doctor of Philosophy

in the Department of Physics   to be taken   December 2010

Title: RAMAN OPTICAL FREQUENCY COMB GENERATION IN HYDROGEN-

FILLED HOLLOW-CORE FIBER

Approved: _____

Dr. Michael G. Raymer

In this dissertation, we demonstrate the generation of optical Raman frequency combs by a single laser pump pulse traveling in hydrogen-filled hollow-core optical fibers. This comb generation process is a cascaded stimulated Raman scattering effect, where higher-order sidebands are produced by lower orders scattered from hydrogen molecules. We observe more than 4 vibrational and 20 rotational Raman sidebands in the comb. They span more than three octaves in optical wavelength, largely thanks to the broadband transmission property of the fiber.

We found that there are phase correlations between the generated Raman comb sidebands (spectral lines), although their phases are fluctuating from one pump pulse to

another due to the inherit spontaneous initiation of Raman scattering. In the experiment, we generated two Raman combs independently from two fibers and simultaneously observed the single-shot interferences between Stokes and anti-Stokes components from the two fibers. The experimental results clearly showed the strong phase anti-correlation between first-order side bands. We also developed a quantum theory to describe this Raman comb generation process, and it predicts and explains the phase correlations we observe.

The phase correlation that we found in optical Raman combs may allow us to synthesize single-cycle optical pulse trains, creating attosecond pulses. However, the vacuum fluctuation in stimulated Raman scattering will result in the fluctuation of carrier envelope phase of the pulse trains. We propose that we can stabilize the comb by simultaneously injecting an auxiliary optical beam, mutually coherent with the main Raman pump laser pulse, which is resonant with the third anti-Stokes field.

CURRICULUM VITAE

NAME OF AUTHOR: Chunbai Wu

GRADUATE AND UNDERGRADUATE SCHOOLS ATTENDED:

University of Oregon, Eugene, Oregon

Shanghai Jiaotong University, Shanghai, China

DEGREES AWARDED:

Doctor of Philosophy in Physics, 2010, University of Oregon

Master of Science in Physics, 2005, University of Oregon

Bachelor of Science in Applied Physics, 2002, Shanghai Jiaotong University

PROFESSIONAL EXPERIENCE:

Graduate Research Assistant
    University of Oregon 2004 - 2010.

Graduate Teaching Assistant
    University of Oregon 2002 - 2003.

AWARDS AND HONORS:

Graduate Research Fellow, University of Oregon, 2004-present

Graduate Teaching Fellow, University of Oregon, 2002-2004

Outstanding Graduate Award, SJTU, 2002

Shih Yu-Lang Memorial Scholarship for Academic Excellence, SJTU, 1999-2001

PUBLICATIONS:

C. Wu, M. G. Raymer, Y.Y. Wang and F. Benabid, "Quantum theory of phase correlations in optical frequency combs generated by stimulated Raman scattering", accepted by Physical Review A (2010)

Y.Y. Wang, C. Wu, F. Couny, M. G. Raymer and F. Benabid, "Quantum-fluctuation-initiated coherence in multioctave Raman optical frequency combs," Physical Review Letter **105**, 123603 (2010)

C. Wu, E. Mondloch, M. G. Raymer, Y.Y. Wang, F. Couny and F. Benabid, "Spontaneous phase correlations in Raman optical frequency comb generation", Frontier in Optics/Laser Science Conference 2010

C. Wu, E. Mondloch, M. G. Raymer, Y.Y. Wang, F. Couny and F. Benabid, "Spontaneous phase anti-correlations in Raman optical frequency comb generation", CLEO/QELS 2010 (QTuA5)

W. Ji, C. Wu and M. G. Raymer, "Slow light propagation in a linear-response three-level atomic vapor", Journal of Optical Society B **24**, 629 (2007)

W. Ji, C. Wu, S. J. van Enk and M. G. Raymer, "Mesoscopic entanglement of atomic ensembles through non-resonant stimulated Raman scattering", Physical Review A **75**, 052305 (2007)

W. Ji, C. Wu and M. G. Raymer, "Quantum statistics of stimulated Raman scattering in optically-pumped Rb vapor", CLEO/QELS 2006 (QMD7)

C. Wu and M. Raymer, "Efficient picosecond pulse shaping by Programmable Bragg gratings", IEEE Journal of Quantum Electronics **42**, 871 (2006)

ACKNOWLEDGEMENTS

During my many years study in University of Oregon, I owe a lot of sincere thanks to many people. I would like to first thank my advisor Professor Michael Raymer, who consistently supported my research and life. He has led me to greatly improve my skills in writing, presentations and conducting researches. I will always benefit from his advises and encouragements in my after-graduation life as a scientist and researcher. I would also like to acknowledge and thank Prof. Steven van Enk for his help and collaborations in our quantum entanglement project. I thank Prof. Dan Steck for helpful insights in "everything you want to know" about Rubidium atoms.

I also got numerous help from my labmates and coworkers. Dr. Wenhai Ji taught me basic optics lab skills. Dr. Andy Funk helped me with regenerative cavity setup through emails. Erin Mondloch, Cade Gladehill and Kyle Lynch-Klarup assisted me in setting up HCPCF experiments. Hayden McGuinness was always helpful in discussions and sharing his inventory of optics. Dr. Brian Smith, Dr. Justin Hannigan, Dr. Guoqiang Cui, Dr. Cody Leary, Dash Vitullo and Roger Smith always provided me with helpful insights about physics and research problems. All of them are my good friends and I wish them well in whatever they are doing or will do.

I would also like to thank Dr. Larry Scatena for his great help in my laser systems.

I have learned a lot of technical skills in lasers while working with him. For other people who supported me in electronics and machining, I would like to say "thank you": Cliff Dax, Kris Johnson, David Senkovich, John Businger and Jeffery Garman.

Living in Eugene for a foreign student would be hard without a great host family. I am fortune enough to have them supporting me and loving me for years. Mr. James Jennings and his wife, Ms. Patricia Jennings, have accepted me as part of their family from the first day I arrived in Eugene. Their daughters' families, the Thompsons and Petersons, also give me warm-hearted loves and supports. I remember every thanksgiving and Christmas dinner that I was invited at their homes. Those were most treasurable memories in my life.

Finally, I want to thank my wife Jenny. She has been supporting me in everything she could during this long journey of Ph.d. program. I truly enjoy every moment with her, and will always love her as I did in the first day we met in middle school.

DEDICATION

To my wife Jenny,

My parents,

And Mr. James H. Jennings and his family

– Your love has supported me, truly.

TABLE OF CONTENTS

LIST OF FIGURES

CHAPTER I

AN INTRODUCTION TO OPTICAL FREQUENCY COMB

Backgrounds

Optical frequency comb refers to light whose spectrum, if analyzed in the frequency domain by spectrometers or other instruments, consists of many discrete, equally spaced, narrow-width spectral lines [1]. Mathematically, the frequency of the n-th order spectra line in the comb can be expressed as:

$$f_n = n \times f_{rep} + f_0,$$

where f_{rep} is the frequency difference between two adjacent comb lines, and f_0 is the offset frequency.

Since time and frequency is one Fourier transform pair, the optical frequency comb is equivalent to a periodic optical pulse trains in the time domain. For example, ultrafast (usually shorter than one nano-second) mode-locked lasers that are commonly used in optical physics laboratory produce such pulse trains, as shown in Figure 1.1 [2].
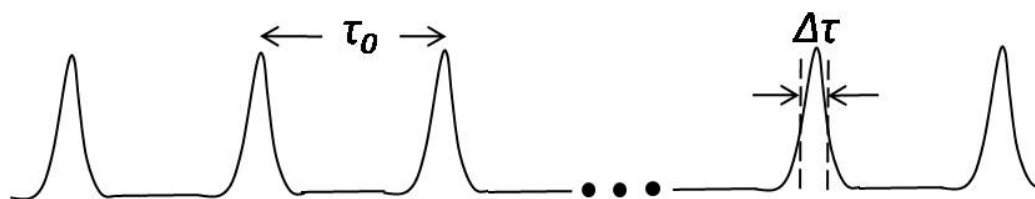
Figure 1.1. Periodic pulse trains produced from mode-lock laser.

In mode-lock lasers, a gain medium with extremely broad spectral range (typically larger than 100 nm in wavelength) is placed inside the laser cavity. Once the gain medium is pumped by a continuous wave (cw) source, there are hundreds of thousands of longitudinal modes spontaneously and simultaneously excited inside the cavity. The spectral separation between adjacent longitudinal modes is determined by the round trip time of the light travelling inside the cavity, and is typically on the order of 100 MHz to 1 GHz. In order to allow all these modes to be built up and eventually lasing in short-pulse form, a technique called mode-locking is used so that the phases of different longitudinal modes are coherent and locked [3, 4].

In Figure 1.2, I plot the comb-like spectrum of the output of a 30 femtosecond (10^{-15} s) Ti:Sapphire mode-locked laser with repetition rate at 80 MHz. The central wavelength of the laser output is at 800 nm, and the spectral width is about 16 THz. It therefore contains more than 200,000 comb lines with spacings equal to 80 MHz.

Span Ω: more than 200,000 comb lines or 16THz

Center wavelength:
800 nm or 375 THz
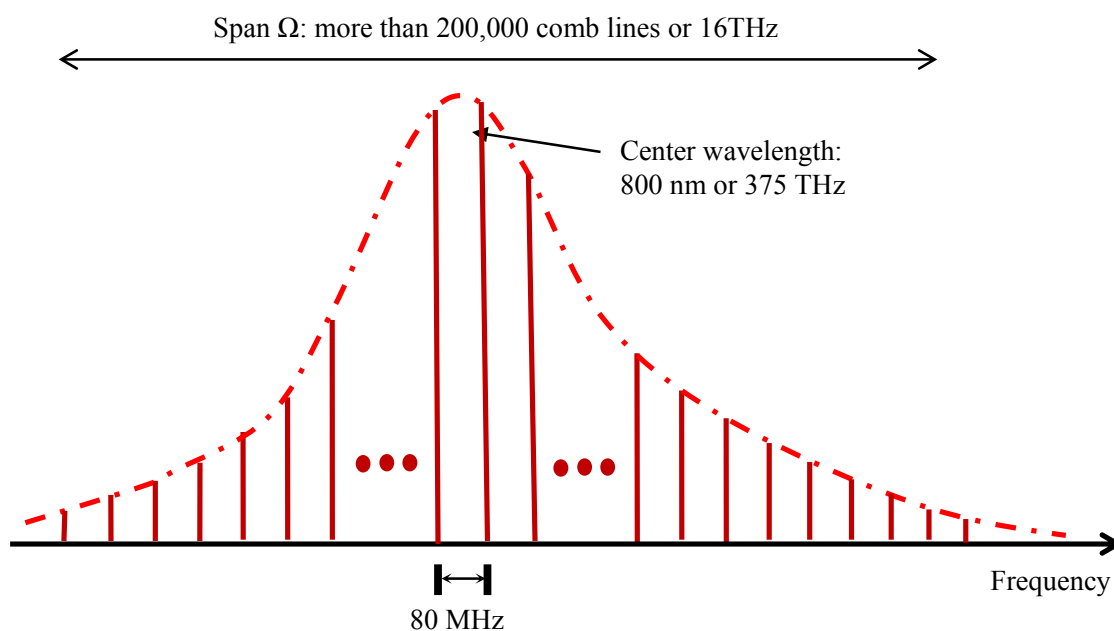
Frequency

80 MHz

Figure 1.2. Frequency comb produced by 30 femto-second
mode-lock laser with repetition rate at 80 MHz.

The application of such optical frequency combs is in optical metrology [5,6]. A
simplified understanding of this application can be made analogous to a regular distance-
measuring "ruler". Each comb line is acting as a marker on the "ruler", and the spacing
between two adjacent comb lines gives its unit. In experiment, the comb line spacing
$f_{rep} \approx 80$ MHz can be precisely determined by counting the frequency of the laser pulse
trains detected on a fast photodiode. However, it's not easy to determine and lock the
value of frequency offset f_0. One way to do this is the "self-referencing" scheme [7].

In "self-referencing" scheme, the output frequency comb of the Ti:Sapphire laser is
first sent into a solid-core photonic crystal fiber [8]. Thanks to the large nonlinearity of

this kind of fiber, the spectrum of the comb is significantly broadened by the effects such as "self-modulation" and sum and different frequency generations, so that the comb spectrum eventually spans more than one octave (factor of two) [9]. In this way the lower frequency part of the comb can then be frequency doubled in a nonlinear-optical crystal to spectrally overlap partially with the higher frequency part. The heterodyne beating frequency detected by a photodiode will then give the value of f_0, and is also serving as a feedback signal for active locking of the laser cavity. The output of the laser is then a stabilized frequency comb.

In order to measure an unknown frequency when using the frequency comb, one can use the comb lines as markers, the same as how we use a ruler to measure distance. The measurement accuracy, which usually is quantified by the ratio of the measurement uncertainty Δf and the absolute frequency f as a unitless number, is extremely small for the optical frequency comb. For example, a typical Ti:Sapphire femto-second mode-locked laser will produce a phase-coherent comb whose optical frequency is about 400 THz. The line spacing in the comb equals the repetition rate of the laser, which is typically set at 80 MHz. After employing sophisticated phase-locking technique, the measurement uncertainty Δf can go down to 1 kHz. The ratio between these two numbers is in the order of 10^{-13}, which is extremely accurate compared with other technologies.

This high accuracy in frequency measurement makes the optical frequency comb extremely useful in frequency metrology. For example, one can measure the absolute optical frequency of Cesium D1 line (335 THz or 895 nm) to the resolution of tens of kHz [10]. In another example, the optical frequency combs directly linked optical

frequencies to microwave frequencies beyond five orders of frequency difference, and thus enables the optical atomic clock at extreme high precision [11]. Physics society has recognized the importance of research work in optical frequency comb, and awarded the initial investigators with Nobel Prize [12] in year 2005.

Motivation

We are interested in another application of the optical frequency comb, which is to synthesize sub femto-second (or atto-second) pulses [13, 14]. Mathematically, the pulse train given by the optical frequency comb in Figure 1.1 is expressed as:

$$E(t) = \sum_n \tilde{E}(f_n) e^{i2\pi(f_n t + \phi_n)} \quad, f_n = n \times f_{rep} + f_0, \tag{1-1}$$

where ϕ_n is the phase of individual comb. For simplicity, we assume the phase term is constant for all comb lines.

It can be shown that the electric field in time domain $E(t)$ in Equation (1-1) is a periodic function, and its period is

$$\tau_0 = 1 / f_{rep},$$

and, when minimum-duration pulses are created, the width of each pulse (temporal duration) is directly related to the total frequency span of the comb Ω. A rule of thumb for the duration is

$$\Delta\tau \sim 1/\Omega.$$

Therefore, a large frequency span of the optical comb could result in extremely short pulses if all the comb lines are phase coherent. Atto-second pulses are very useful in the applications of real-time observation and time-domain control of atomic-scale electron dynamics [15]. One example is by stabilizing the carrier envelope phase of the generated atto-second pulses, it is possible to create light-induced atomic currents in ionized matter, and thus control the motion of the electronic wave packets on timescales shorter than 250 atto-seconds [16].

In order to generate atto-second pulses, one needs the spectral span of an optical frequency comb larger than a few hundred THz. This is out of reach by any active lasing medium used in mode-lock lasers. In our lab, we generate the optical frequency comb by using cascaded Raman scattering in hydrogen gas [17]. Many previous works in this research area employ two independent but phase-stabilized laser pulses to adiabatically drive the molecular coherence to produce a multiple-octave spanning optical comb [18, 19]. However, we use only a single pump pulse in our experiment. This is an interesting situation where all the Raman comb lines (except the pump) are spontaneously generated from the initially zero-photon occupied (vacuum) state. In another words, the generated Raman comb lines appear to be classical fields, in the sense that they have well defined

amplitudes and phases, but they arise from quantum initiation and amplification, which distinguishes this from the two-pump situation. This argument is also true for the molecular coherence (vibrational or rotational) created in the hydrogen molecules. From this point of view, the Raman comb generation process by a single pump is also an excellent tool to study quantum optics, such as entanglement and quantum fluctuations.

Previous work on Raman scattering theories and experiments has shown that the generated field from a single Raman pump, which is called the Stokes field, is temporally and spatially coherent [20, 21], if the scattering takes place in the transient regime and its Fresnel number is close to unity so the field is diffraction-limited. These two conditions can be easily satisfied in most Raman scattering experiments. It suggests that the Stokes field is a transform-limited pulse with a well-defined temporal phase. But in order to generate atto-second pulses from the optical Raman comb, one must have phase correlation between those Raman comb components, since in short-pulse synthesis the frequency components must satisfy certain deterministic phase relationships. Whether or not such correlation exists is a fundamental question that had not been previously answered. In this dissertation we will theoretically explore this critical phase correlation in the transient high-gain regime with no pump depletion. We will show that, for the first order of Stokes and anti-Stokes, they are very well phase anti-correlated throughout the duration of these two pulses, even at the situation where large dispersion is induced by a group velocity difference of Raman sidebands propagating through the media. For higher order Raman components, we predict their phases are also correlated within one pump pulse. The result reveals that a short pulse train could be synthesized. However, due to

inherent spontaneous initiation of Raman scattering, the generated Raman comb is found to fluctuate significantly from one pump pulse to another. This fluctuation not only occurs in the energy of those Stokes or anti-Stokes fields, but also in their temporal phases. I will show that this fluctuation may change the carrier envelope phase of synthesize atto-second pulse trains to be random from one shot to another. However, from our theoretical predictions and experimental evidences, we also find that there is a new way to lock the random phase to one deterministic value. This will be discussed later.

Overview of stimulated Raman scattering

In order to understand how the optical Raman comb is generated by a single pump pulse and to see its importance in quantum optics, it is necessary to review the history of Raman scattering and its applications. The first observations of Raman scattering in liquids were reported in 1928 [22]. This discovery of "a new radiation" not only demonstrates the inelastic scattering of light, but opens a new era to explore how light can interact with matter. This Raman scattering effect was extensively studied by using natural (sun) light before the invention of laser in 1960, mainly focusing on how it is different from other optical phenomenon, such as fluorescence and Rayleigh scattering, and how to determine the scattering cross-section from semi-classical theory [23]. Only with the strong coherent light that is produced from lasers, the stimulated effect on Raman scattering was first observed [24]. In this stimulated Raman scattering process,

the produced (or frequency-shifted) scattered light, which is usually called Stokes (frequency down-shifted) or anti-Stokes (frequency up-shifted), reaches a macroscopic level. Today in industry Raman scattering is well known for its application as "Raman Spectroscopy" [25], since different materials will scatter light with distinctive frequencies. This spectroscopic method has been widely used as a basic method for analyzing chemical compositions of gases, liquids and solids.

The significance of Raman scattering in modern research is its relation to quantum optics, since by studying the Raman scattering process, it provides answers to some basic quantum problems, such as how the initial spontaneously scattered photons evolved from vacuum under the influence of the pump field [26], and what the quantum coherence property is for the resulting macroscopic field if the stimulated effect is taking place. An extensive work in this topic was conducted by Dr. Raymer during 1980s [27]. His group first observed the macroscopic energy fluctuations in the generated Stokes field under transient high-gain conditions with no depletion of the pump field [21]. He also co-developed a quantum theory [20] for describing this phenomenon. It was shown that the energy fluctuation is related to the quantum initiation of the Stokes field, which was also experimentally shown to be temporally and spatially coherent in later experiments [28].

In recent progress of quantum information experiments, Raman scattering has also been used as a method to create quantum memory in an ensemble of Raman-active atoms, such as rubidium or cesium [29, 30]. In those experiments a strong pump laser acted as a writing tool to interact with the atoms off-resonantly, and the produced Stokes field was detected to know what "quantum information" has been written into the atomic medium.

In the mean-time, the Raman scattering process will also result in the transition of the atoms between two atomic electronic spin states that are generally not dipole-transition allowed. In a good approximation, the quantum state of collective electronic spin (CES) states of all atoms in one medium is entangled with the generated Stokes field, and thus carries the same "quantum information" as the one that has been written in. This CES state was demonstrated to be stored up to 1 μs in the ensemble and later read-out in a reverse process, where all the quantum information that was written into the CES state was transferred into generated anti-Stokes field.

Further application in quantum information is to generate an entangled state between two distant atomic ensembles [31, 32]. In practice, one atomic ensemble can be treated as a node in a quantum network. By creating entanglement between them, quantum information could be relayed through the whole network. Mathematically, the entangled state of two atomic ensembles means that it cannot be written as the product of CES states in individual ensembles. To create such entanglement, a writing process using a Raman scattering scheme is induced in each atomic ensemble. The Stokes fields generated independently from two atomic ensembles can be entangled by interfering in a simple optical device, such as a 50:50 beam-splitter. The entangled field states after this device can be detected, and from quantum theory, after detection the collapsed state of the two atomic ensembles is then entangled. The generated entanglement then can be verified by a read-out process. However, until today most such experiments were realized under the spontaneous regime, which resulted in very few Stokes photons being generated and detected by single photon detectors, and required an electric-field induced

transparency (EIT) scheme [33] to avoid re-absorption of the Stokes photons by the media. One recent breakthrough [34] has demonstrated quantum memories in Cs ensemble by using broadband (larger than 1 GHz) optical pulses, instead of megahertz modulated cw lasers.

Overview of Raman optical frequency comb generation

As shown in Figure 1.1, the mode-locked lasers generate ultrashort optical pulses by establishing a fixed phase relationship across their spectrum of frequency. However, the frequency span of the comb generated by these lasers is typically no larger than 20 THz. Most experiments using optical combs to do absolute frequency measurements, such as atomic clocks and attosecond control of electronic processes, require the comb spectra to a have multiple-octave span. As described in the previous section, one way to generate such a broad spectrum is using photonic crystal fiber that has large nonlinear effects like four-wave mixing or self-phase modulation.

Alternatively, discrete Raman combs from molecules are studied in many recent research efforts that aim to synthesize sub-femto or atto-second optical pulses. In this scheme, a cascaded Raman scattering process is induced under certain conditions. The generated first-order Stokes and anti-Stokes fields, which are co-propagating with the intense pump light, will be scattered by the molecules again to produce higher order sidebands. Therefore, the frequency comb generated will have a similar spectrum as

shown in Figure 1.2. The Raman shift in the medium determines the frequency difference between two adjacent comb lines, which, in a mode-locked cw laser, is controlled by its resonator length. This Raman shift is quite large, for example, in hydrogen molecules, the rotational Raman shift is 18 THz, and the vibrational Raman shift is about 125 THz.

The first experiment to explore the Raman comb generation is done in hydrogen gas when multiple rotational lines are observed and analyzed under high-power femto-second pulses [17]. Shortly after that experiment a two-pump scheme is proposed [35] where the Raman coherence is driven slightly off resonance and results in the Raman spectrum with Bessel-function amplitudes and phases. Experiments following this scheme successfully produced single-cycle optical pulses by adjusting the relative phase between each comb component [18]. Further efforts in controlling the carrier envelope phase of the generated single cycle pulse [19, 36], as well as to generate constant shape pulse trains [37], have been realized. Other experimental schemes, such as using ultra-short pulses to generate impulsive Raman coherence, also show promising phase locking effect between Stokes and anti-Stokes components.

In another hand, micro-structured hollow-core fiber (HCF) has been developed [38], and it shows broad transmitting optical band which is even larger than one octave. For a typical step-index fiber, the optical modes are confined inside the core area with higher refractive index than that of the cladding materials. No optical modes can be guided when the core is hollow for this kind of fiber. However, in micro-structured HCF, its cladding is constructed in a way that resembles the periodic structure of a two-dimensional crystal lattice. Indeed, an easy picture to see how the light is confined inside the fiber where a

large air hole is surrounded by such cladding structure is by the Bragg reflections off the periodic crystal lattice. Using the similar theory that is used in solid-state physics to describe the crystal structure, one can calculate the photonic band-gap which determines the guided wavelength of such fiber.

Since the core area of the HCF fiber is hollow, one can fill it with different gases under various pressures. If strong laser light is coupled into such fiber, cascaded Raman scattering may take place, creating a Raman optical frequency comb [39]. Using fiber in generating Raman combs has two major advantages compared with the conventional free-space Raman experiments: first, a Raman active medium like hydrogen gas can be pressure sealed inside the core area of the fiber and thus strongly interact with coupled pump light. Second, since the core diameter of most HCF fiber is about 10 microns, the pump light is tightly focused when transmitting inside the fiber. This ensures the pump intensity as well as the Raman interaction region are extremely larger compared with the conventional free-space Raman experiments using a long-focal-length lens to focus the pump.

For an example, in our lab, we generate more than 20 Raman rotational lines in hydrogen gas when coupling a Raman pump into the gas-filled HCF fiber. The power of the Raman pump is about 10 micro-joules per pulse, which is very low compared to the power required in a free-space setup, usually at 10 millijoules.

Outlines

In this dissertation, I will focus on the discussion of the phase relationship between comb lines in Raman optical frequency comb generation. I will first show how we predict this phase relationship by using both classical and quantum models. Then the experimental setup that allows us to generate Raman combs and verify this phase relationship will be covered. In the last part, I will discuss a proposal for how to lock more strongly the phases of comb lines based on our theory and observations.

In Chapter II, I start with the description of how a single molecule or atom interacts off-resonantly with light to produce frequency-shifted Stokes and anti-Stokes photons. I then discuss the stimulated Raman scattering process in a molecular ensemble, and a possible cascade process that produces many orders of Stokes and anti-Stokes lines. In order to connect established Raman scattering theory with cascaded Raman scattering effect which produces optical Raman frequency comb, we take all orders of Stokes and anti-Stokes fields into consideration. By following the method adopted in [40], we first adiabatically eliminate the molecular intermediate states from the interaction Hamiltonian, and then use optical Maxwell-Bloch theory to derive the equations of motion for all Stokes and anti-Stokes fields, as well as the buildup of the molecular coherence. We also develop an alternative approach where the propagations of Stokes and anti-Stokes fields are derived directly in the quantum Heisenberg picture, and find the same equations of motion. In the last part of this Chapter, I will discuss that in stimulated Raman scattering process where only first order Stokes is present, the Stokes field and molecular coherence

are created in an entangled state. This special property of Raman scattering has been used to generate entanglement between two distant atomic ensembles.

In Chapter III, the analytical solution of the equations of motion involving only first-order Stokes and anti-Stokes in a quantum model is shown. The numerical evaluations of these solutions based on quantum initiation conditions are then used to calculate the newly defined phase anti-correlation coefficient. We show that this coefficient is directly related to the intensity and phase fluctuations of first-order Stokes and anti-Stokes fields. Our calculation result then predicts that the phases of first-order Stokes and anti-Stokes are nearly perfect anti-correlated, which means the sum of their phases remains constant from shot to shot. Following this prediction, a semi-classical non-perturbative theory assuming that excited molecules act as a phase modulator is used to show that there exists a deterministic relation between phases of all comb lines in a single shot.

In Chapter IV, the experiments to generate a Raman optical frequency comb in hydrogen-filled hollow-core photonic crystal fiber (HCPCF) are presented. First, I briefly describe the manufacturing procedures and guiding mechanisms of HCPCFs that are made in University of Bath, UK. Then I show our own design of gas loading cell that is capable to fill the hollow-core fiber with controllable pressure gases. Most parts of this gas loading cell use commercially available parts, and require very little machining. It also shows the advantages of easy assembly and high pressure sealing. Next, I will describe our laser system, which consists of a mode-locked Ti:Sapphire laser producing nearly Fourier-transform-limited pulses with 200 pico-seconds temporal duration and a one-stage amplification system (regenerative amplifier). The amplified pulse is then used

as a Raman pump to couple into HCPCF filled with hydrogen gas. Depending on the polarization state of the Raman pump, I show the observed hydrogen rotational or vibrational optical combs.

In Chapter V, I will show the setup of a two-fiber experiment that will directly measure the phase correlation between comb lines. The experimental results and the data analysis will be covered as well. We emphasize the observed strong spontaneous phase anti-correlations between first-order sidebands, which are consistent with our theoretical predictions. A weaker phase correlation between first-order Stokes and 2nd order anti-Stokes is also shown. I will then describe a two-color experiment that verifies the phase correlations predicted by our semi-classical model. In this experiment the second harmonic (in blue color) of amplified pulse (in red color) generated in a BBO crystal and the amplified pulse itself are simultaneously coupled into HCPCF. This blue light is kept in low intensity so that it is only scattered off the molecular coherence created by the red light. The experimental results reveal that the molecular coherence is indeed acting as a phase modulator for light scattering from it. At the end of this chapter, I will discuss the possibility to extend the two-color experiment to lock the phase of Raman comb, which will be crucial to generate atto-second pulse trains with constant carrier envelope phases.

I will summarize my research work in the last chapter of this dissertation.

CHAPTER II

THEORY OF RAMAN OPTICAL FREUQUENCY

COMB GENERATION

Spontaneous Raman scattering background

As shown in Figure 2.1, an optical pulse propagating at z direction encounters a single molecule in its ground state. If the frequency of the optical pulse is far detuned from any transition line of the molecule, an inelastic scattering may occur where the frequency of the optical pulse is shifted and the molecule is transferred to its excited state. This is the well-known spontaneous Raman scattering process. The energy diagram of the described Raman transition is shown in Figure 2.2. In our theoretical model, we assume the optical pulse to be quasi-monochromatic, and its temporal duration is shorter than the Raman dephasing time, but its spectral linewidth is much narrower than the Raman frequency shift. Under these conditions, the Raman scattering process is in transient regime.
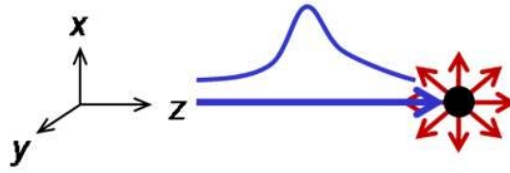
Figure 2.1. Single molecule scattering

We denote the molecule's ground state as $|1\rangle$ and the excited state as $|3\rangle$. Those intermediate states in Figure 2.2 are true molecular states, but in Raman scattering, the molecule has never occupied those states because the pump is detuned far from resonant. However, these intermediate states are necessary for Raman scattering to occur, since no dipole-allowed transition exists between the ground state $|1\rangle$ and excited state $|3\rangle$. In other words, the dipole moment defined as $\hat{d}_{13} = \langle 1|\vec{r}|3\rangle$ is zero in the molecular system, in the case of homonuclear molecules.

Although the ground state $|1\rangle$ and excited state $|3\rangle$ are not directly coupled, the molecule can still be transferred from one state to another in the Raman scattering process. It will be shown in the following that the effective d_{13}^{eff} in Raman scattering will be non-zero with the help of those virtual states $|m\rangle$.

The generated new optical field in Raman scattering where the original optical pulse is scattered by the molecule is called the Stokes field. It's easy to see from the energy conservation that the frequency of the Stokes field is $\omega_s = \omega_0 - \omega_{31}$.

After the molecule scattered to the excited state, it might get scattered back again by an inverse process. This is shown in Figure 2.3. A frequency up-shifted optical field

called the anti-Stokes field is produced during this process. The anti-Stokes field will have frequency $\omega_{as} = \omega_0 + \omega_{31}$.
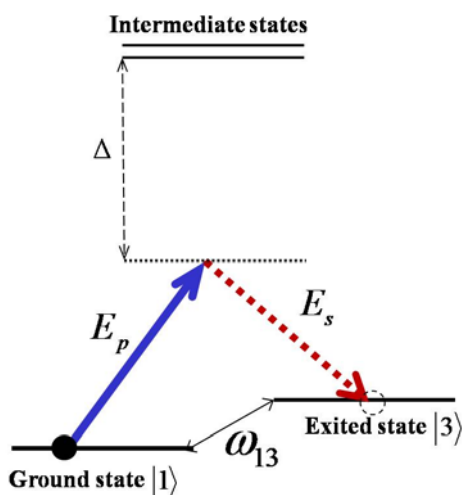
Figure 2.2. Energy diagram of Raman scattering
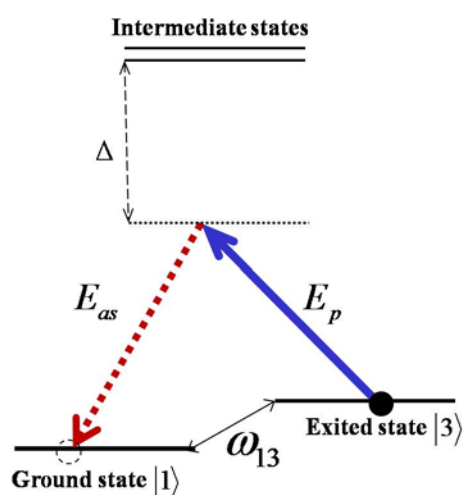
Figure 2.3. Energy diagram of inverse Raman scattering

The energy structures of real molecules are very complicated, since there are many possible degrees of freedoms in its Hamiltonian, such as electronic, nuclear vibration and rotation, inter-molecular and so on. However, in order to discuss Raman scattering, we could simplify the energy structure to a few levels whose transition will have the largest Raman scattering cross sections. For example, in hydrogen molecules, the most significant Raman scattering takes place involving the vibrational and rotational states between two hydrogen atoms (shown in Figure 2.4). All other states, such as electronic, will be treated as intermediate states. In this simplified model, the energy structure of

molecules is essentially a Λ system. Both the ground state $|1\rangle$ and excited state $|3\rangle$ are assumed to be degenerate, which means a single wave-function is sufficient to describe each state.
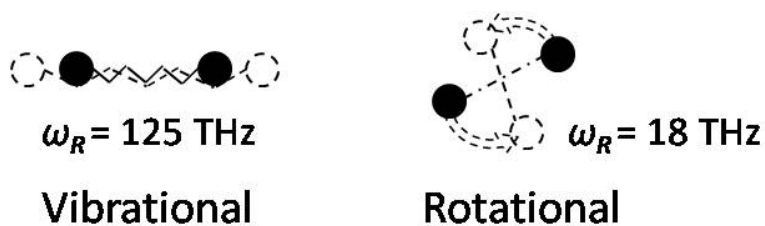
Figure 2.4. Vibrational and rotational state in bi-atomic hydrogen molecule

The energy separation between ground state $|1\rangle$ and excited state $|3\rangle$ is $\Delta E = \hbar\omega_{13}$. At room temperature, for $\Delta E \gg k_B T$ where k_B is the Boltzmann constant, the molecule will naturally be in its ground state. However, if that condition is not met, the molecule will have near-equal probability in its ground or excited state. In this situation, the optical Raman gain will be diminished. An optical pump scheme is required so that the molecule is prepared in its ground state.

Stimulated Raman scattering and Raman comb generation

Now we consider an ensemble of molecules that is confined within a pencil-shaped container. As shown in Figure 2.5, an optical pulse propagating along the length of the container interacts off-resonantly with these molecules. Each molecule can experience the spontaneous Raman scattering process to produce the Stokes field, as described in the previous section. In certain conditions, especially when the optical pulse, which is called the Raman pump, is intense enough, the spontaneous scattering can build up to generate a strong Stokes field that is co-propagating with the original optical pulse. This phenomenon is called stimulated Raman scattering.
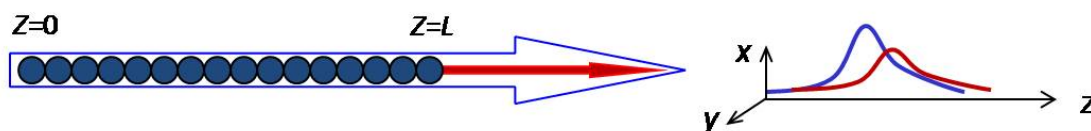
Figure 2.5. Raman scattering of an ensemble of molecules (Blue curve indicates Raman pump, and red curve indicates generated Stokes field)

One simple way to understand the stimulated process is as follows: the Stokes fields spontaneously generated from the first few molecules in the ensemble interacting with a strong Raman pump are distributed uniformly for each propagation direction. However, the Stokes field that happened to be propagating co-linearly with the pump laser may stimulate the scattering process occurring in the next available molecules. Here, "stimulate" means the first Stokes field, as shown in the leftmost event in Figure 2.6,

forces the next Raman scattering effect to produce a Stokes field with an identical property, i.e., the propagation direction, the wavelength and temporal phase. In other words, the Raman pump laser set a preferable direction where the Stokes fields from sequential spontaneous Raman scattering will be produced coherently. This is very similar to how lasers work. This stimulated Raman scattering process will continue until the Raman pump is depleted and the Stokes field could build up to a macroscopic level (larger than one million photons).
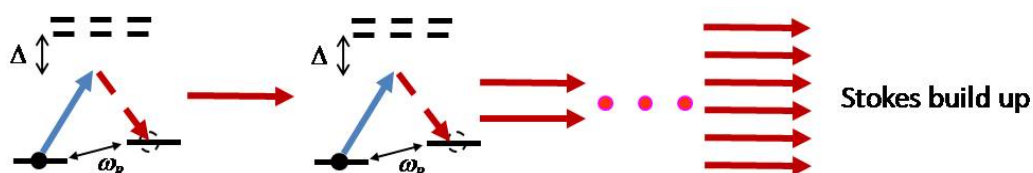
Figure 2.6. Stimulated Raman scattering generation

Molecules that are scattered to an excited state in the stimulated Raman scattering process can be scattered back by the same pump pulse to produce anti-Stokes photons (see Figure 2.3). Similar to the Stokes field buildup, the anti-Stokes field can also reach macroscopic level. The generation of both Stokes and anti-Stokes photons can be made analogous to a four-wave mixing process, where two pump photons are annihilated, and Stokes and anti-Stokes photons are generated. In this process, there exists a phase mismatch, i.e., $\Delta\beta = \beta_s + \beta_{as} - 2\beta_0$, where β_s, β_{as}, β_0 are the wave-vectors of Stokes, anti-Stokes and Raman pump fields, respectively. It has been shown that in a perfect phase-matching condition, the Stokes and anti-Stokes processes will be suppressed, while

for small but nonzero phase mismatch it will be enhanced. We will point this out in a later chapter.

After this Stokes field gets stronger, it might be scattered by the molecules again to produce higher-order sidebands. The same will happen to the anti-Stokes fields. This cascaded process is what we call "Raman comb generation." In Figure 2.7 we show this process. Because in our experiment we use very short (200 ps), high-intensity laser pulses to excite the Raman scattering, we will focus our theoretical discussion in a high-gain transient regime. In the following section, I will show how we obtain the equations of motion of the slowly varying parts of the radiation fields (including all Raman comb lines) and the collective molecular coherence.
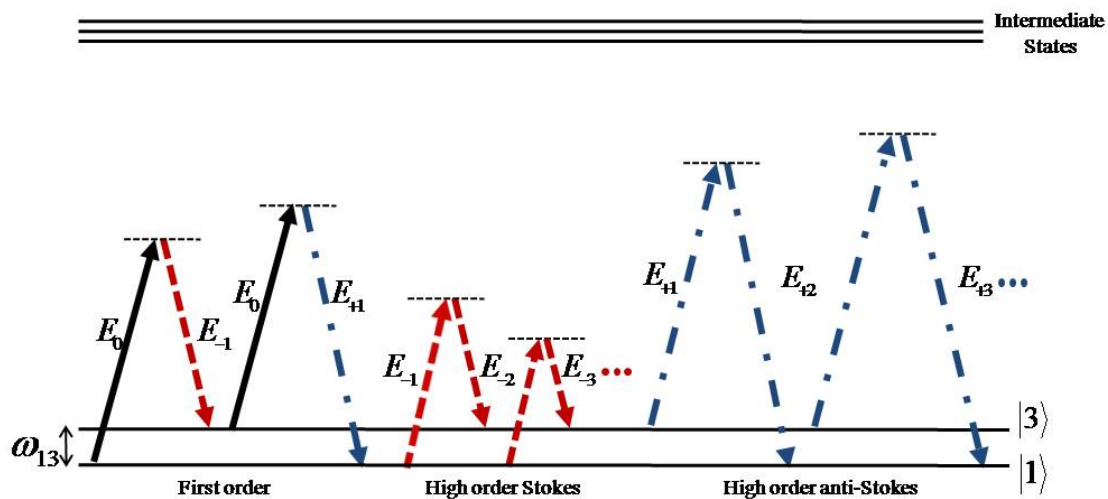
Figure 2.7. Cascaded Raman scattering process

Raman comb theory

We start our mathematical derivation with the quantum theory of Raman scattering, which will generalize to include any number of Raman lines in comb generation process [40]. Consider a single molecule located at position z and its interaction with all electric fields containing the pump and generated Raman sidebands. We write the electric fields as:

$$E = \sum_n E_n^{(+)}(z,t)e^{i(\beta_n z - \omega_n t)} + h.c. \qquad (2\text{-}1)$$

where we label integer number n as the order of sidebands, $n<0$ for Stokes fields, $n>0$ for anti-Stokes fields, and $n=0$ for the pump. We will keep this convention of naming the order of Stokes and anti-Stokes fields throughout the rest of this dissertation. $E_n^{(+)}(z,t)$ is the positive frequency part of the slowly varying envelope function. This envelope function is directly related to the photon creation and annihilation operators in quantum optics, and we will show its real form in the next section. The carrier frequency ω_n in the expression for the different order of the Stokes (anti-Stokes) line obeys the energy conservation, and it is related to the pump's frequency by:

$$\omega_n = \omega_0 + n \times \omega_{31}, \qquad (2\text{-}2)$$

In other words, the generated spectrum of cascaded Raman scattering process would be an equally spaced optical frequency comb. The parameter β_n is the wave-vector of the n-

th order sideband, and its value is mainly determined by the dispersion property of the medium.

The total Hamiltonian that will determine the molecule's equation of motion can be written as (neglecting free radiation fields):

$$H = H_0^{mol} + H_I , \qquad (2\text{-}3)$$

In the above equation, $H_0^{mol} = \hbar \sum_m \Omega_m |m\rangle\langle m|$ is the molecule's static Hamiltonian, and

$$H_I = -\hbar\{\sum_m d_{m1}\sigma_{m1}(t)E(z,t) + d_{3m}\sigma_{3m}(t)E(z,t) + h.c.\} \qquad (2\text{-}4)$$

is the dipole interaction Hamiltonian between the molecule and the electric fields of light. The operator $\sigma_{m,n} = |m\rangle\langle n|$ is the molecular transition operator between state $|n\rangle$ and $|m\rangle$. If the zero of energy is taken at the level of the ground state, the static Hamiltonian can be re-written as $H_0^{mol} = \hbar \sum_m \omega_{m1}\sigma_{m1}(t)\sigma_{m1}(t)$, where $\omega_{m1} = \Omega_m - \Omega_1$.

We then obtain the equations of motion for molecular operators that involve states $|1\rangle, |3\rangle$ and $|m\rangle$ in the Heisenberg picture (neglect any transition between intermediate states):

$$\frac{\partial}{\partial t}\sigma_{31} = i\omega_{31}\sigma_{31} + i\sum_m d_{1m}E\sigma_{3m} - i\sum_m d_{m3}E\sigma_{m1} , \qquad (2\text{-}5\text{-}1)$$

$$\frac{\partial}{\partial t}\sigma_{m1} = i\omega_{m1}\sigma_{m1} - id_{1m}E(\sigma_{11} - \sigma_{mm}) - id_{3m}E\sigma_{31}, \qquad (2\text{-}5\text{-}2)$$

$$\frac{\partial}{\partial t}\sigma_{3m} = i\omega_{3m}\sigma_{3m} - id_{3m}E(\sigma_{mm} - \sigma_{33}) - id_{m1}E\sigma_{31}. \qquad (2\text{-}5\text{-}3)$$

In our transient Raman scattering theory, we assume the laser is detuned far away from the intermediate states, that is, $\omega_m - \omega_0 \gg d\dfrac{|E|}{\hbar}$. In this situation, the molecule is assumed to never truly occupy those intermediate states $|m\rangle$ during the interaction. Therefore, we would like to eliminate these intermediate states from our equation of motion. In order to do so, we need to apply some essential approximations, and next, I am going to show this derivation in some detail. The first term of Equation 2-5-1 reads:

$$\frac{\partial}{\partial t}\sigma_{31}(t) \sim i\omega_{31}\sigma_{31}. \qquad (2\text{-}6)$$

This shows the operator $\sigma_{31}(t)$ is oscillating at its natural frequency ω_{31}. Any temporal oscillating term appearing in its equation of motion that has a frequency other than ω_{13} may be neglected (or have negligible contribution).

We can formally integrate Equation 2-5-2 and 2-5-3 and get:

$$\sigma_{m1}(t) = \sigma_{m1}(0)e^{i\omega_{m1}t} - i\int_0^t dt' e^{i\omega_{m1}(t-t')}\{d_{1m}E(t')[\sigma_{11}(t') - \sigma_{mm}(t')] + d_{3m}E(t')\sigma_{31}(t')e^{i\omega_{31}(t-t')}\},$$

$$(2\text{-}7\text{-}1)$$

$$\sigma_{3m}(t) = \sigma_{3m}(0)e^{i\omega_{3m}t} - i\int_0^t dt' e^{i\omega_{3m}(t-t')}\{d_{3m}E(t')[\sigma_{mm}(t') - \sigma_{33}(t')] + d_{m1}E(t')\sigma_{31}(t')e^{i\omega_{31}(t-t')}\},$$

$$(2\text{-}7\text{-}2)$$

These expressions for $\sigma_{m1}(t)$ and $\sigma_{3m}(t)$ can then be put into Equation 2-5-1 and only

the terms that have $e^{i\omega_{31}t}$ need to be retained. For example, the third term in Equation 2-7-

1 can be written as:

$$
\begin{aligned}
-i\sum_m d_{3m}E\sigma_{m1} = -i\sum_m d_{m3}E(t)\sigma_{m1}(0)e^{i\omega_{m1}t} \\
-\sum_m d_{m3}d_{1m}E(t)\int_0^t dt'e^{i\omega_{m1}(t-t')}E(t')[\sigma_{11}(t')-\sigma_{mm}(t')] \\
-\sum_m |d_{3m}|^2 E(t)\int_0^t dt'\, e^{i\omega_{m1}(t-t')}E(t')\sigma_{31}(t')e^{i\omega_{31}(t-t')}
\end{aligned}
$$

In the above equation, the first term proportional to $\sigma_{m1}(0)$ is oscillating at ω_{m1}, and

can be neglected. The third term, which is proportional to $\sigma_{31}(t)$ itself, is a term directly

resulting in AC Stark shift. It only slightly shifts the frequency ω_{31} and is also negligible.

The only term that might have oscillation at ω_{31} is the second term, and by using Equation

2-1, we can get:

$$
\begin{aligned}
-i\sum_m d_{m3}E\sigma_{m1} \approx -\sum_m d_{1m}d_{m3}\int_0^t dt'\, e^{i\omega_{m1}(t-t')} \times \\
\times \sum_{n_1}\sum_{n_2}\{E_{n_1}^{(+)}(z,t)e^{i\beta_{n1}z-i(\omega_0+n_1\omega_R)t}+h.c\}\{E_{n_2}^{(+)}(z,t')e^{i\beta_{n2}z-i(\omega_0+n_2\omega_R)t'}+h.c\}[\sigma_{11}(t)-\sigma_{mm}(t')]
\end{aligned}
$$

$$(2\text{-}8)$$

Here we use the Rotating-wave approximation (RWA) to neglect terms involving

$t+t'$. This will allow us to simplify the double summation in (2-8) as:

$$\sum_{n_1}\sum_{n_2}\{E_{n_1}^{(+)}(z,t)e^{i\beta_{n1}z-i(\omega_0+n_1\omega_{31})t}+h.c\}\{E_{n_2}^{(+)}(z,t')e^{i\beta_{n2}z-i(\omega_0+n_2\omega_{31})t'}+h.c\}[\sigma_{11}(t)-\sigma_{mm}(t')]$$

$$\approx\sum_{n_1}\sum_{n_2}E_{n_1}^{(-)}(z,t)E_{n_2}^{(+)}(z,t')e^{i\omega_0(t-t')}e^{i(n_1t-n_2t')\omega_{31}}e^{i(\beta_{n2}-\beta_{n1})z}+h.c\}[\sigma_{11}(t)-\sigma_{mm}(t')]$$

$$\approx\sum_{n}\{E_{n}^{(-)}(z,t)E_{n-1}^{(+)}(z,t')e^{i(\omega_0+(n-1)\omega_{31})(t-t')}+E_{n-1}^{(+)}(z,t)E_{n}^{(-)}(z,t')e^{-i(\omega_0+n\omega_{31})(t-t')}\}e^{-i\Delta\beta_n z}e^{i\omega_{31}t}\times$$

$$\times[\sigma_{11}(t)-\sigma_{mm}(t')]$$

$$(2\text{-}9)$$

where $\Delta\beta_n=\beta_n-\beta_{n-1}$.

Again, since operator $\sigma_{31}(t)$ is oscillating at frequency ω_{31}, in the second step of the above derivation we eliminate one summation to only retain the term $e^{i\omega_{31}t}$. By putting this result back into Equation 2-8, and making the adiabatic following approximation since the slowly varying envelopes $E_n(z,t)$, operators $\sigma_{33}(t)$ and $\sigma_{mm}(t)$ are all slowly changing compared with the frequency ω_{m1}, we have:

$$-i\sum_{m}d_{m3}E\sigma_{m1}\approx-\sum_{m}d_{1m}d_{m3}\int_0^t dt'\,e^{i\omega_{m1}(t-t')}\times$$

$$\times\sum_{n}\{E_{n}^{(-)}(z,t)E_{n-1}^{(+)}(z,t')e^{i(\omega_0+(n-1)\omega_{31})(t-t')}+E_{n-1}^{(+)}(z,t)E_{n}^{(-)}(z,t')e^{-i(\omega_0+n\omega_{31})(t-t')}\}e^{-i\Delta\beta_n z}e^{i\omega_{31}t}$$

$$\times[\sigma_{11}(t)-\sigma_{mm}(t')]$$

$$\approx-i\sum_{n}\sum_{m}\gamma_m^* E_n^{(-)}(z,t)E_{n-1}^{(+)}(z,t)e^{-i\Delta\beta_n z}e^{i\omega_{31}t}[\sigma_{11}(t)-\sigma_{mm}(t)]$$

$$(2\text{-}10)$$

where we define $\gamma_m=d_{3m}d_{m1}\dfrac{1}{\omega_{m1}+\omega_0+(n-1)\omega_{31}}+\dfrac{1}{\omega_{m1}-\omega_0-n\omega_{31}}$.

In a similar way, we can get the second term in equation 2-5-1 as:

$$i\sum_{m}d_{1m}E\sigma_{3m}=-i\sum_{n}\sum_{m}\gamma_m^* E_n^{(-)}(z,t)E_{n-1}^{(+)}(z,t)e^{-i\Delta\beta_n z}e^{i\omega_{31}t}[\sigma_{mm}(t)-\sigma_{33}(t)].\qquad(2\text{-}11)$$

Finally, by using equations 2-10 and 2-11, we simplify equation 2-5-1 as:

$$\frac{\partial}{\partial t}\sigma_{31}(t) = i\omega_{31}\sigma_{31}(t) - i\sum_n\sum_m \gamma_m E_n^{(-)}(z,t)E_{n-1}^{(+)}(z,t)e^{-i\Delta\beta_n z}e^{i\omega_{31}t}[\sigma_{11}(t) - \sigma_{33}(t)] \qquad (2-12)$$

Since we assume the molecule initially in its ground state, and the probability of the molecule staying in state $|3\rangle$ is very small, that means $\sigma_{11} - \sigma_{33} \approx 1$ remains valid throughout the interaction. Therefore, Equation (2-12) is further simplified as:

$$\frac{\partial}{\partial t}\sigma_{31}(t) = i\omega_{31}\sigma_{31}(t) - i\sum_n \alpha_{1,n}^* E_n^{(-)}(z,t)E_{n-1}^{(+)}(z,t)e^{-i\Delta\beta_n z}e^{i\omega_{31}t} \qquad (2-13)$$

where the Raman transition coefficient is given by:

$$\alpha_{1,n} = \sum_m d_{3m}d_{m1}\left(\frac{1}{\omega_{m1} + \omega_0 + (n-1)\omega_{31}} + \frac{1}{\omega_{m1} - \omega_0 - n\omega_{31}}\right). \qquad (2-14)$$

We define the slowly varying part of operator $\sigma_{31}(t)$ as another variable Q^K:

$$Q^\kappa(t) = \sigma_{31}(t)e^{i\omega_{31}t}. \qquad (2-15)$$

Here we use symbol κ to denote the different molecule located at position z. The physical meaning of $Q^K(t)$ is the slowly varying molecular-raising operator, which eliminates one molecule initially in ground state $|1\rangle$ and at the same time, creates one

molecule in excited state $|3\rangle$. Its equation of motion can easily be derived from Equation 2-13:

$$\frac{\partial}{\partial t}Q^{\kappa}(t) = -i\sum_{n}\alpha_{1,n}^{*}E_{n}^{(-)}(z,t)E_{n-1}^{(+)}(z,t)e^{-i\Delta\beta_{n}z} \tag{2-16}$$

The above equation describes the response of a single molecule at location z to the electric fields. Next, we consider an ensemble of molecules that are assumed to be evenly distributed in a pencil-like region, as shown in Figure 2.5, with the length L in z direction, area A in the cross-section and the molecule's number density N. In our theory, we assume the Fresnel number of the interaction, defined as $\frac{A}{\lambda L}$, is smaller than unity for all optical fields. For this reason, a one-dimensional model is sufficient for modeling the cascaded Raman process.

In order to treat the propagation of the radiation field, it is convenient to define the collective molecular raising operator at position z by:

$$Q(z,t) = \frac{1}{N}\sum_{\{\kappa\}_{z}}Q^{\kappa}(t), \tag{2-17}$$

where the summation runs for all molecules that are occupied at position z. People often refer to Q as the molecular collective coherence.

The commutation relation for $Q(z,t)$ and $Q^{\dagger}(z',t)$ can be found as:

$$\left[Q^{\dagger}(z,t), Q(z',t) \right] = \frac{1}{NA} \delta(z - z') \tag{2-18}$$

We can rewrite Equation 2-16 as:

$$\frac{\partial}{\partial t} Q(z,t) = -i \sum_n \alpha_{1,n}^* E_n^{(-)}(z,t) E_{n-1}^{(+)}(z,t) e^{-i\Delta\beta_n z} \ . \tag{2-19}$$

Next, we will calculate the macroscopic polarization operator, which is defined as:

$$P(z,t) = \sum_{\{\kappa\}} P^{\{\kappa\}}(t) \delta(z - z^{\kappa}), \tag{2-20}$$

where $P^{\{m\}}(t)$ is the polarization arising from single molecule located at position z^m:

$$P^{\{\kappa\}}(t) = \hbar \sum_m d_{m1} \sigma_{m1} + d_{3m} \sigma_{3m} + h.c.. \tag{2-21}$$

We can evaluate the above polarization by using Equation 2-5, which also uses similar adiabatic approximations:

$$\begin{aligned} P^{\{\kappa\}}(t) = &\hbar \sum_n \alpha_{1,n+1}^* E_{n+1}^{(-)}(z,t) Q^{(\kappa)\dagger}(t) e^{-i\Delta\beta_{n+1} z} e^{-i(\beta_n z - \omega_n t)} \\ &+ \hbar \sum_n \alpha_{1,n} E_{n-1}^{(-)}(z,t) Q^{(\kappa)}(t) e^{i\Delta\beta_n z} e^{-i(\beta_n z - \omega_n t)} + h.c. \end{aligned}, \tag{2-22}$$

Using equation 2-22, the macroscopic polarization $P(z,t)$ can be written as:

$$P(z,t) = N\hbar \sum_n \alpha^*_{1,n+1} E^{(-)}_{n+1}(z,t) Q^\dagger(z,t) e^{-i\Delta\beta_{n+1}z} e^{-i(\beta_n z - \omega_n t)} +$$
$$+N\hbar \sum_n \alpha_{1,n} E^{(-)}_{n-1}(z,t) Q(z,t) e^{i\Delta\beta_n z} e^{-i(\beta_n z - \omega_n t)} + h.c. \qquad (2\text{-}23)$$

This macroscopic polarization can be used to calculate the equation of motion that accounts for the spatial propagation of the electric fields in the Raman comb generation process. The well-known one-dimensional Maxwell-Bloch equation is:

$$\left(\frac{\partial}{\partial z} + \frac{\partial}{c\partial t} \right) E = \frac{2\pi}{c} \frac{\partial}{\partial t} P(z,t), \qquad (2\text{-}24)$$

Then using equation 2-23 for $P(z,t)$ and equation 2-1 for E, and sorting out the term with fast optical oscillation ω_n, the equation of motion for the n-th order comb line can be found from equation 2-24 as:

$$\left(\frac{\partial}{\partial z} + \frac{1}{c} \frac{\partial}{\partial t} \right) E^{(-)}_n(z,t) = -i\alpha_{2,n+1} E^{(-)}_{n+1}(z,t) Q^\dagger(z,t) e^{-i\Delta\beta_{n+1}z} - i\alpha^*_{2,n} E^{(-)}_{n-1}(z,t) Q(z,t) e^{i\Delta\beta_n z} \qquad (2\text{-}25)$$

where the coefficient $\alpha_{2,n} = 2\pi\hbar N \omega_n \alpha^*_{1,n}/c$.

Equations 2-19 and 2-25 will be the coupled equations describing the Raman comb generation.

An alternative approach

In the previous section, we started with the single molecule's interaction with light and then derived the equation of motion for the slowly varying collective molecular-raising operators and the electric fields. Although we write the electric fields in standard quantum optics operators, we derive their equations from the Maxwell-Bloch theorem, a corollary from quantum mechanics and Maxwell equations. In this section, we use a different approach where the basic quantum theory – the dynamics of a quantum operator in the Heisenberg picture – is used. This approach will be useful in the future development of the Raman theory because of its simplicity and clearness.

We first quantize the radiation field in free space, which can be found in a standard textbook. It starts with the transverse part of the potential vector in Coulomb gauge in terms of normal modes. In our situation where only one propagation dimension (along the z axis) is considered, then the normal modes will have wave vectors being quantized as $\beta = n\dfrac{2\pi}{L}, \quad n = 0, \pm 1, \pm 2, \ldots$. The quantized electric field can be written as:

$$E_x(z,t) = -i\sum_m \sqrt{\frac{2\pi\hbar\omega_m}{AL}} a_m e^{i\beta_m z - i\omega_m t} + h.c \qquad (2\text{-}26)$$

where x labels the polarization of the electric field, A and L are the area (assume uniformity along z) and length of the molecular medium. The operator a_m is the photon

annihilation operator that is similar to the one used in the quantum-mechanic harmonic oscillator and the commutation of a_m and a_n obeys:

$$\left[a_m, a_n^\dagger \right] = \delta_{m,n} . \qquad (2\text{-}27)$$

If $L \rightarrow \infty$, the discrete summation of all normal modes may be re-written in continuous integration, by changing

$$a_m \rightarrow \sqrt{\frac{2\pi}{L}} a(\beta) \ ; \quad \sum_m \rightarrow \int dm = \frac{L}{2\pi} \int d\beta . \qquad (2\text{-}28)$$

In this way, the commutation for $a(\beta)$ and $a^\dagger(\beta)$ is:

$$\left[a(\beta), a^\dagger(\beta') \right] = \delta(\beta - \beta') \qquad (2\text{-}29)$$

Then using 2-28, the quantized electric field is:

$$E_x(z,t) = -i \int d\beta \sqrt{\frac{\hbar \omega(\beta)}{A}} a(\beta) e^{i\beta z - i\omega(\beta)t} + c.c . \qquad (2\text{-}30)$$

We are more interested in the slowly varying envelope of a n-th order Raman sideband that has center frequency ω_n and wave-vector β_n. Therefore, we re-write the quantized electric field in following form:

$$E_x(z,t) = \sum_n E_n^{(-)}(z,t) e^{i(\omega_n t - \beta_n z)} + c.c \qquad (2\text{-}31)$$

and the slowly-varying envelope for *n*-th order sideband is given as:

$$E_n^{(-)}(z,t) = i\sqrt{\frac{\hbar\omega_n}{A}}\int d\delta\beta(1+\frac{v_n^g\delta\beta}{2\omega_n})\tilde{a}_n^\dagger(\delta\beta)e^{i\delta\beta z-iv_n^g\delta\beta t} \; , \qquad (2\text{-}32)$$

where v_n^g is the group velocity of the *n*-th order sideband. In deriving equation 2-32, we have used the dispersion relation as $\omega(\beta_n + \delta\beta) \approx \omega_n + v_n^g\delta\beta$, and have changed the integration variable in equation 2-31 to small wave-vector spreading $\delta\beta$ around β_n .

The total Hamiltonian of the radiation field in free space is given by:

$$H_0^{rad} = \frac{A}{8\pi}\int dz(|E_x(z,t)|^2 + |B_y(z,t)|^2) \qquad (2\text{-}33)$$

By putting into the full expression for the electric (equation 2-31) and magnetic fields, it can be shown that the above Hamiltonian can be simplified as:

$$H_0^{rad} \approx \sum_n \frac{\hbar}{2}\int d\delta\beta \, v_n^g \{\tilde{a}_n^\dagger(\delta\beta)\tilde{a}_n(\delta\beta) + \tilde{a}_n(\delta\beta)\tilde{a}_n^\dagger(\delta\beta)\} \; . \qquad (2\text{-}34)$$

From equation 2-32, the slowly varying envelope can be written approximately as:

$$\tilde{E}_n^{(-)}(z,t) = i\sqrt{\frac{\hbar\omega_0}{A}}\tilde{a}_n^\dagger(z,t) \; , \qquad (2\text{-}35)$$

if we define the new photon creation and annihilation operator as:

$$\tilde{a}_n^{\dagger}(z,t) = \int d\delta k \, \tilde{a}_n^{\dagger}(\delta k) e^{-i\delta k z + i v v_n^g \delta k t} \tag{2-36}$$

The Fourier inverse transform of above equation would give:

$$\tilde{a}_n^{\dagger}(\delta k) = \frac{1}{2\pi} \int dz dt \, \tilde{a}_n^{\dagger}(z,t) e^{i\delta k z - i v_n^g \delta k t} \tag{2-37}$$

Then, the free-space Hamiltonian in Equation 2-34 can be expressed in a different way:

$$
\begin{aligned}
H_0^{rad} &= \sum_n \frac{\hbar}{2} \int (d\delta\beta) v_g^n \delta\beta \left(\frac{1}{2\pi}\right)^2 \int dz_1 \, \tilde{a}_n^{\dagger}(z_1,t) e^{i\delta\beta z_1 - i v_g^n \delta\beta t} \int dz_2 \tilde{a}_n(z_2,t) e^{-i\delta\beta z_2 + i v_g^n \delta\beta t} \\
&= \sum_n \frac{\hbar}{8\pi^2} \int (d\delta\beta) v_g^n \left\{ \delta\beta \int dz_1 \, \tilde{a}_n^{\dagger}(z_1,t) e^{i\delta\beta z_1} \right\} \int dz_2 \tilde{a}_n(z_2,t) e^{-i\delta\beta z_2} \\
&\approx \sum_n \frac{\hbar}{8\pi^2} \int (d\delta\beta) v_g^n \int dz_1 \frac{\partial \tilde{a}_n^{\dagger}(z_1,t)}{\partial z_1} e^{i\delta\beta z_1} \int dz_2 \tilde{a}_n(z_2,t) e^{-i\delta\beta z_2} \\
&= \sum_n \frac{\hbar}{4\pi} \int dz v_g^n \frac{\partial \tilde{a}_n^{\dagger}(z,t)}{\partial z} \tilde{a}_n(z,t)
\end{aligned}
\tag{2-38}
$$

We can further write this Hamiltonian in terms of the slowly varying operator $E_n(z,t)$, by using the inverse of equation 2-35:

$$H_0^{rad} = \sum_n \frac{ic}{4\pi\omega_n} \int A dz \frac{\partial \tilde{E}_n^{(-)}(z,t)}{\partial z} \tilde{E}_n^{(+)}(z,t) + h.c. \tag{2-39}$$

if we assume the group velocities of all the electric fields in free space are at the speed of light in a vacuum, c. This form is consistent with, but generalizes, that in Haus [41].

The commutation between the positive and negative frequency part of the slowly varying envelope can be easily found from equation 2-45, and take the form as:

$$\left[\tilde{E}_n^{(+)}(z,t), \tilde{E}_m^{(-)}(z',t') \right] = \delta_{nm} \frac{2\pi\hbar\omega_0}{A} \delta(z-z'-c(t-t')) \qquad (2\text{-}40)$$

The interaction Hamiltonian between the radiation field and the single molecule at position z is given by equation 2-4, and if we include all molecules, then the interaction Hamiltonian can be formally written as:

$$H_I = -\hbar\{A\int dz \sum_{\{\kappa\}} \sum_m d_{m1}\sigma_{m1}^\kappa(t)E(z,t) + d_{3m}\sigma_{3m}^\kappa(t)E(z,t) + h.c.\} \qquad (2\text{-}41)$$

Again, we use the adiabatic-following approximation to eliminate those intermediate states $|m\rangle$ from the above interaction Hamiltonian. To do so, the expressions for $\sigma_{m1}(t)$ and $\sigma_{3m}(t)$ that are shown in Equation 2-5 are put into the Hamiltonian, and a similar approach to that in the previous section is applied to only retain those slowly varying terms, then the interaction Hamiltonian can be shown as:

$$H_I = -\sum_n \int (NA)dz\{\alpha_{1,n}Q(z,t)E_n^{(+)}(z,t)E_{n-1}^{(-)}(z,t)e^{i\Delta\beta_n z} +$$
$$+\alpha_{1,n+1}^* Q^\dagger(z,t)E_n^{(+)}(z,t)E_{n+1}^{(-)}(z,t)e^{-i\Delta\beta_{n+1}z}\} \qquad (2\text{-}42)$$

Combining Equation 2-39 and 2-42, the total Hamiltonian of our system is $H = H_0^{rad} + H_I$. The molecular static Hamiltonian H^{mol} is not included in H because it is eliminated when we do the slowly varying transformation from $\sigma_{13}(t)$ to $Q(z,t)$

(Equation 2-15). Indeed, the Hamiltonian H is in the interaction picture. The equation of motion for slowly-varying electric field operator of n-th order comb component can be easily obtained from standard quantum theory:

$$\partial_t E_n^{(-)}(z,t) = i\left[H_0^{rad} + H_I, E_n^{(-)}(z,t) \right] \qquad (2\text{-}43)$$

Using the commutation relations that are shown in Equation 2-25 and 2-50, the above equation can be simplified as:

$$(\partial_z + \frac{1}{c}\partial_t)E_n^{(-)}(z,t) = -i\alpha_{2,n+1}E_{n+1}^{(-)}\exp(-i\Delta\beta_{n+1}z)Q^\dagger - i\alpha_{2,n}^* E_{n-1}^{(-)}\exp(i\Delta\beta_n z)Q \qquad (2\text{-}44)$$

The new coefficient $\alpha_{2,n}$ is given by: $\alpha_{2,n} = 2\pi\hbar N\omega_n\alpha_{1,n}^* / c$.

The equation of motion for the collective molecular raising operator can be obtained in a similar way:

$$\begin{aligned}
\partial_t Q^\dagger(z,t) &= i\left[H_0^{rad} + H_I, Q^\dagger(z,t) \right] \\
&= -i\left[\sum_n \int (NA)dz'\{\alpha_{1,n}Q(z',t)E_n^{(+)}(z',t)E_{n-1}^{(-)}(z',t)e^{i\Delta\beta_n z'} + \right. \\
&\quad \left. +\alpha_{1,n+1}^* Q^\dagger(z',t)E_n^{(+)}(z',t)E_{n+1}^{(-)}(z',t)e^{-i\Delta\beta_{n+1}z'}\}, Q^\dagger(z,t) \right] \\
&= i\sum_n \alpha_{1,n}E_n^{(+)}E_{n-1}^{(-)}\exp(i\Delta\beta_n z)
\end{aligned} \qquad (2\text{-}45)$$

It is easy to see that the equations of motion that we derive in this section are the same as those we get in the previous section (Equation 2-19 and 2-25). By changing the variable from (z,t) to (z,τ), where $\tau = t - z/c$, the equations of motion become:

$$\partial_z E_n^{(-)}(z,\tau) = -i\alpha_{2,n+1}E_{n+1}^{(-)}\exp(-i\Delta\beta_{n+1}z)Q^{\dagger} - i\alpha_{2,n}^{*}E_{n-1}^{(-)}\exp(i\Delta\beta_n z)Q , \qquad (2\text{-}46)$$

$$\partial_\tau Q^{\dagger}(z,\tau) = i\sum_n \alpha_{1,n}E_n^{(+)}E_{n-1}^{(-)}\exp(i\Delta\beta_n z) . \qquad (2\text{-}47)$$

These two equations will be our starting point to make the theoretical predictions on interesting features in the Raman optical frequency comb generation process, which will be discussed in the next chapter.

Quantum entanglement in stimulated Raman scattering

During the optical Raman frequency comb generation, the collective molecular coherence $Q(z,t)$ and optical comb components E_n are initiated from a vacuum state, and then amplified to a macroscopic level. Equations 2-46 and 2-47 describe this process. However, an interesting question is whether the collective molecular coherence has special correlations with those electric fields. In this section, I will review this special correlation, which in a later context will be shown as quantum entanglement, under the condition that only first-order Stokes is generated.

The interaction Hamiltonian that involves only first-order Stokes and Raman pump can be written directly following Equation 2-42:

$$H_I = -\int (NA)dz\{\alpha_{1,0}Q(z,t)E_0^{*}(z,t)E_{-1}^{(-)}(z,t)e^{i\Delta\beta_0 z} + h.c\}$$

Since the Raman pump is assumed to be a strong laser field, we write its form E_0 classically instead of in a quantum operator. Using the above Hamiltonian or Equation (2-46) and (2-47), the equations of motion for first-order Stokes and molecular collective coherence are:

$$\frac{\partial}{\partial z} E_{-1}^{(-)}(z,\tau) = -i\alpha_{2,0}E_0(\tau)Q^\dagger(z,\tau)e^{-i\Delta\beta_0 z},$$

$$\frac{\partial}{\partial \tau} Q^\dagger(z,\tau) = i\alpha_{1,0}E_0(\tau)E_{-1}^{(-)}(z,\tau)e^{i\Delta\beta_0 z}. \qquad (2\text{-}48)$$

After doing a complex conjugation of the first equation above, absorbing dispersion factor $\Delta\beta_0 z$ into $E_0(\tau)$, and defining parameters: $\hat{a}_{-1}(z,t) = \sqrt{\dfrac{Ac}{2\pi\hbar\omega_{-1}}}E_{-1}^{(+)}(z,t)$ as a Stokes photon annihilation operator, $g_0 = \sqrt{\dfrac{2\pi N\hbar\omega_{-1}}{c}}$ as a normalized gain coefficient, and $\hat{b}^\dagger(z,t) = \sqrt{NA}Q(z,t)$ as the molecular creation operator, the coupled equation is written in a more symmetric form:

$$\frac{\partial}{\partial z}\hat{a}(z,\tau) = g_0 E_0(z,\tau)\hat{b}^\dagger(z,\tau),$$

$$\frac{\partial}{\partial t}\hat{b}(z,\tau) = g_0 E_0(z,\tau)\hat{a}^\dagger(z,\tau). \qquad (2\text{-}49)$$

We call the operator $\hat{a}(z,t)$ the photon annihilation operator and $\hat{b}^\dagger(z,t)$ the molecular creation operator because their same positions or time commutation relations are normalized delta functions:

$$\left[\hat{a}(z,\tau),\hat{a}^\dagger(z,\tau')\right]=\delta(\tau-\tau')\,,\quad \left[\hat{b}(z,\tau),\hat{b}^\dagger(z',\tau)\right]=\delta(z-z')\,. \tag{2-50}$$

The solution of the coupled equation can be found by using Green's propagators. We will show the details of derivation in next chapter. Here, I follow the method used in [42], where a modified Bloch-Messiah reduction theorem is applied. The solution of the coupled equation 2-49 is indeed a summation of many two-mode squeezing processes, and each process is a Bogoliubov transformation:

$$\hat{a}_n^{out}=\hat{a}_n^{in}\cosh\xi_n+\hat{b}_n^{(in)\dagger}\sinh\xi_n$$
$$\hat{b}_n^{out}=\hat{b}_n^{in}\cosh\xi_n+\hat{a}_n^{(in)\dagger}\sinh\xi_n \tag{2-51}$$

In the above equation, we have decomposed the input operators $a(0,\tau)$ and output operators $a(L,\tau)$ into different temporal modes $\hat{a}_n^{in}$ and $\hat{a}_n^{out}$, respectively. We also decomposed the operators $\hat{b}(z,-\infty)$ and $\hat{b}(z,+\infty)$ into different spatial modes $\hat{b}_n^{in}$ and $\hat{b}_n^{out}$. The detailed mathematical expression for these decompositions can be found in the reference [42]. For each mode, the squeezing parameter ξ_n determines the photon occupation number by:

$$\langle\hat{n}_n\rangle=\sinh^2\xi_n\,. \tag{2-52}$$

From a numerical evaluation of equation 2-52, there exists a *dominant* pair of temporal modes of the Stokes field and a spatial mode of collective molecular coherence if dispersion is absent. In Figure 2.8 we show the calculated photon number distribution

of most occupied temporal modes [42] in the generated Stokes field under different dispersion conditions. The calculation assumes the Gaussian-shaped pump pulse and the collisional dephasing was neglected. It shows that if there is no group-velocity difference between Stokes and pump fields ($\Delta\beta_0 = 0$), the most occupied Stokes temporal mode has a thousand times more photons than the second most occupied mode.

This existence of a dominant mode justifies that the generated Stokes field and the collective molecular coherence can be simply treated in a two-mode squeezing state. Generally, this state is also an entangled state, in analogy to an optical parametric down-conversion process. The common explanation of this entanglement is, if one Stokes photon is detected in output, then there must be a molecule also being transferred to its excited state.

If there are many sidebands other than a single Stokes line in the comb generation, then the above argument of entanglement is no longer rigorously valid. But since the sidebands and molecular collective coherence are generated cooperatively, we conjecture that they will be generated in a multi-partite entangled state.
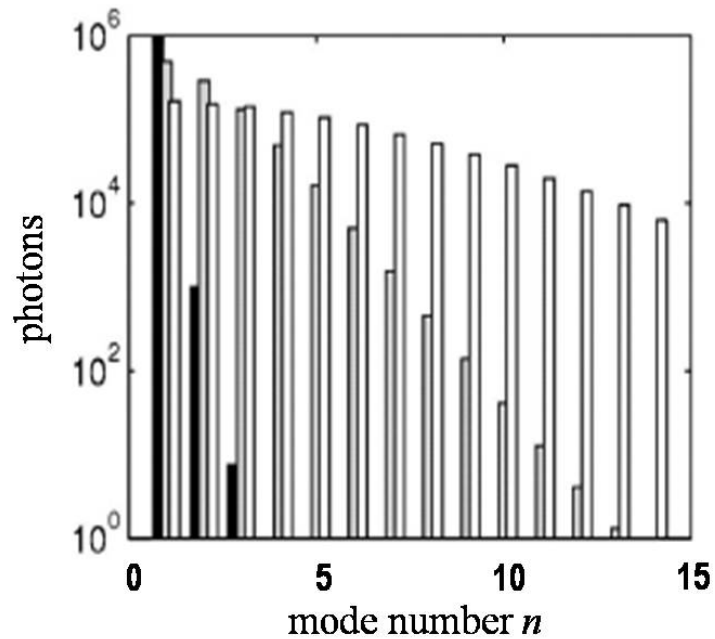
Figure 2.8. Photon occupation number (equation 2.52) for different output modes under different dispersion conditions: $\Delta\beta_0 = 0$ (black bar), -10 ps/mm (gray bar) and -30 ps/mm (hollow bar). Results are from reference [42].

Quantum entanglement between two atomic ensembles

In this section, I would like to briefly review one project that I had worked on before I shifted my research focus to Raman frequency comb generation. This project utilized the entanglement idea in a stimulated Raman scattering process, and was aiming to create an entangled state between two distant objects, which are alkali atom ensembles. We used atoms instead of molecules because the electronic Raman scattering in atoms has a much

longer lifetime, typically in the order of micro-seconds. This long quantum lifetime of collective electronic spin (CES) coherence has played an important role in recent quantum network experiments.

The entanglement scheme is plotted in Figure 2.9. The Stokes field generated by the stimulated Raman scattering process in each atomic ensemble (A or B) was mixed at a 50/50 beamsplitter. The two outputs of the beamsplitter were then detected individually by certain methods. After the measurement, the state of two atomic ensembles may be collapsed into an entangled state, depending on the detection scheme.
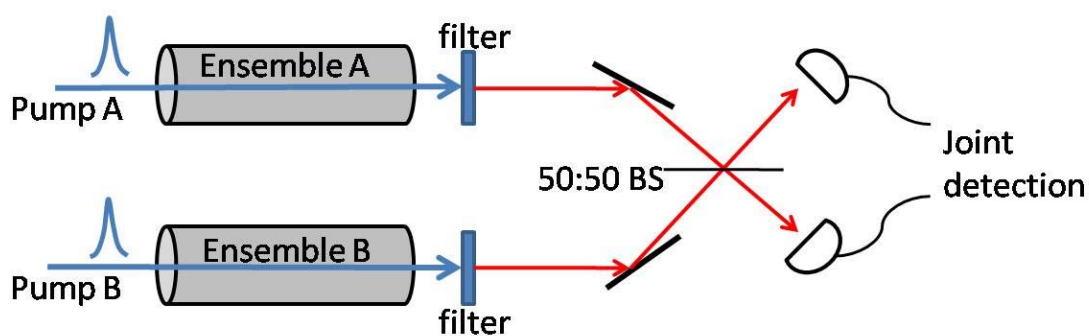
Figure 2.9. Scheme to generate entanglement between two atomic ensembles

In a spontaneous regime, where only very few Stokes photons were generated from each ensemble, one can use avalanched photon detectors (APD) to simultaneously measure whether there were photons or not in the output channels of the beam-splitter. In any stance where only the upper channel detects one click, but the down channel detects no photons, the state of the two atomic ensembles can be shown to be:

$$|\psi\rangle = |1\rangle_A |0\rangle_B + |0\rangle_A |1\rangle_B \qquad (2\text{-}53)$$

This state is one of the maximum entangled Bell states [43].

If the Raman scattering in each ensemble was in a mesoscopic regime, which means the Stokes photon number is in the range of 10 to 100, but still does not reach the stimulated regime, the photon number-resolving detector can be used to measure how many photons are in each output channel of the beamsplitter. If n and m photons were detected, the resultant state of the two atomic ensembles is:

$$|\psi\rangle = \frac{1}{\cosh \xi_1 \times \cosh \xi_2} \sum_{i,j} (\tanh \xi_1)^i (\tanh \xi_2)^j \, B_{i,j}^{n,m} |i\rangle_A |j\rangle_B \qquad (2\text{-}54)$$

where $B_{i,j}^{n,m}$ is the beamsplitter transform matrix with a probability that a 50/50 beam-splitter has i and j photons in its outputs if n and m photons are two inputs.

This state is not as easily verified as an entangled state, especially in an experiment. One practical way to do it is to use a so-called "entanglement witness," which is derived from the Shchukin-Vogel scheme [44]. It measures various moments of creation and annihilation operators of the beam-splitter's two output channels jointly. In principle, this type of measurement can be done by using a balanced homodyne correlation. A detailed description of the proposed experiment can be found in [45].

If the Raman scattering in each atomic ensemble is in a stimulated regime, where the Stokes field is generated at a macroscopic level, we can use balanced homodyne detection to measure the quadrature operators in each output channel of the beamsplitter [46]. Quadratures of Bosonic-like operators are defined as:

$$q = \frac{1}{\sqrt{2}}(a^\dagger + a)$$

$$p = \frac{1}{\sqrt{2}i}(a - a^\dagger)$$

In order to generate entanglement, one measures the two output channels on an orthogonal quantum basis. For example, if one measured the q quadrature in one output of the beamsplitter, one would simultaneously measure the p quadrature in the other output channel. If the measurement results from the above two joint measurements are Q and P, respectively, then the state of the two atomic ensembles can be shown to be collapsed to:

$$|\psi\rangle = \exp(-\frac{s}{2}q_+^2 - \frac{1}{2s}q_-^2 - i\frac{2\mu\nu P}{s}q_- + 2\mu\nu Q q_+)|q_-, q_+\rangle, \qquad (2\text{-}55)$$

where $\mu = \cosh\xi$, $\nu = \sinh\xi$, $s = \mu^2 + \nu^2$ and we assume two Raman scattering processes have same gain coefficient $\xi = \xi_1 = \xi_2$. $q_\pm = (q^A \pm q^B)/\sqrt{2}$ is the sum and difference between the two q quadratures of the two atomic ensembles.

The state $|\psi\rangle$ in Equation 2-68 can also be shown to be an entangled state. A detailed analysis can be found in [47].

Another advantage of using Raman scattering to generate entanglement between two distant atomic ensembles is that, by using a time-delayed control laser light, the quantum state can be readout in an inverse process. This process is depicted in Figure 2-4, where an anti-Stokes field is generated with all atoms in an excited state scattered back to

ground state. This allows the atomic ensemble to serve an important role as a memory and information exchange node in a quantum network.

CHAPTER III

SPONTANEOUS PHASE CORRELATIONS IN RAMAN

OPTICAL FREQUENCY COMB GENERATION

Phase correlation between first order sidebands

Equations (2-46) and (2-47) in Chapter II that include all Raman sidebands is extremely non-linear. There are no analytical solutions for those coupled non-linear operator equations. However, as a simplifying case, we first consider the situation where only first-order Stokes E_{-1} and anti-Stokes E_{+1} fields are created, and the pump intensity profile is unchanged throughout the interaction. This simplified linear model allows us to find a complete quantum description and gain insight into the comb generation process. The coupled equations are:

$$\partial_z E_{-1}^{(-)}(z,\tau) = -i\alpha_{2,s} E_0(\tau) Q^{\dagger}(z,\tau)$$

$$\partial_z E_{+1}^{(+)}(z,\tau) = i\alpha_{2,a} E_0^*(\tau) Q^{\dagger}(z,\tau) \exp(-i\Delta\beta z)$$

$$\partial_\tau Q^{\dagger}(z,\tau) = i\alpha_{1,s} E_{-1}^{(-)}(z,\tau) E_0^*(\tau) + i\alpha_{1,a} E_{+1}^{(+)}(z,\tau) E_0(\tau) \exp(i\Delta\beta z) \qquad (3\text{-}1)$$

where $\Delta\beta = \beta_1 + \beta_{-1} - 2\beta_0$ is the phase mismatch of wave-vectors. Here we treat the Raman pump as a classical field, and it stays unchanged through the entire interaction. These coupled equations in 3-1 were first solved in a full quantum context by Kilin [48], who verified that a slight phase mismatch is needed to maximize the generation of Stokes or anti-Stokes sideband, as seen in experiments [49]. More general solutions than those in [48] are found here using the methods in [40]. Assuming that the pulses are long enough that group-velocity effects are not important, the field operators at the end of the fiber ($z = L$) and at local time $\tau = t - z / \mathrm{v}_g$ (where v_g is the group velocity of the pump) are found to be:

$$
\begin{bmatrix} E_{-1}^{(-)}(L,\tau) \\ E_{+1}^{(+)}(L,\tau) \end{bmatrix} = E_0(\tau)\int_0^\tau d\tau' E_0(\tau') \begin{bmatrix} \alpha_{2,s}G_{11}(L;\tau,\tau') & \alpha_{2,s}G_{12}(L;\tau,\tau') \\ -\alpha_{2,a}G_{21}(L;\tau,\tau') & -\alpha_{2,a}G_{22}(L;\tau,\tau') \end{bmatrix} \begin{bmatrix} \alpha_{1,s}E_{-1}^{(-)}(0,\tau') \\ \alpha_{1,a}E_{+1}^{(+)}(0,\tau') \end{bmatrix}
$$
$$
+ E_0(\tau)\int_0^L dz' \begin{bmatrix} -i\alpha_{2,s}G_{13}(z';\tau,0) \\ i\alpha_{2,a}G_{23}(z';\tau,0) \end{bmatrix} Q^\dagger(L-z',0) + \begin{bmatrix} E_{-1}^{(-)}(0,\tau) \\ E_{+1}^{(+)}(0,\tau)e^{i\Delta\beta L} \end{bmatrix}
$$

$$(3\text{-}2\text{-}1)$$

$$
Q^\dagger(L,\tau) = i\int_0^\tau d\tau' \{ \alpha_{1,s}E_0^*(\tau')G_{13}(L;\tau,\tau')E_{-1}^{(-)}(0,\tau') + \alpha_{1,a}E_0(\tau')G_{13}(L;\tau,\tau')E_{+1}^{(+)}(0,\tau') \}
$$
$$
+ \int_0^L dz' G_0(z';\tau,0)Q^\dagger(L-z',0)
$$

$$(3\text{-}2\text{-}2)$$

The Green propagators are given by:

$$
G_{11}(z;\tau,\tau') = G_{12}(z;\tau,\tau') - i\Delta\beta\int_0^z dz' G_{12}(z';\tau,\tau');
$$

$$
G_{22}(z;\tau,\tau') = G_{12}(z;\tau,\tau') + i\Delta\beta\exp(i\Delta\beta z) * G_{12}(z;\tau,\tau');
$$

$$
G_{12}(z;\tau,\tau') = G_{21}(z;\tau,\tau') = I_0(2\sqrt{\xi_s(\tau,\tau')z}) * [J_0(2\sqrt{\xi_a(\tau,\tau')z})\exp(i\Delta\beta z)];
$$

$$
G_{13}(z;\tau,\tau') = I_0(2\sqrt{\xi_s(\tau,\tau')z}) * [\delta(z) - J_1(2\sqrt{\xi_a(\tau,\tau')z})\sqrt{\xi_a(\tau,\tau')/z}\exp(i\Delta\beta z)];
$$

$$
G_{23}(z;\tau,\tau') = [I_1(2\sqrt{\xi_s(\tau,\tau')z})\sqrt{\xi_s(\tau,\tau')/z} + \delta(z)] * [J_0(2\sqrt{\xi_a(\tau,\tau')z})\exp(i\Delta\beta z)];
$$

$$G_0(z;\tau,\tau') = [I_1(2\sqrt{\xi_s(\tau,\tau')z})\sqrt{\xi_s(\tau,\tau')/z} + \delta(z)]$$
$$* [\delta(z) - J_1(2\sqrt{\xi_a(\tau,\tau')z})\sqrt{\xi_a(\tau,\tau')/z}\exp(i\Delta\beta z)]$$

where "*" denotes convolution on the variable z, and J_n, I_n are n-th order Bessel and modified Bessel functions, respectively. The time-dependent gain coefficients are:

$$\xi_{s,a}(\tau,\tau') = \alpha_{1,(s,a)}\alpha_{2,(s,a)}\int_{\tau'}^{\tau}dt|E_0(t)|^2. \tag{3-3}$$

With the sideband fields initially in the vacuum state and all molecules in their lowest-energy states $|1\rangle$, the initial operators have the following correlation functions :

$$\langle Q^\dagger(z,0)Q(z',0)\rangle = (1/AN)\delta(z-z')$$

$$\langle Q(z,0)Q^\dagger(z',0)\rangle = 0$$

$$\langle E_n^{(+)}(0,\tau')E_n^{(-)}(0,\tau)\rangle = (2\pi\hbar\omega_n/Ac)\cdot\delta(\tau-\tau')$$

$$\langle E_n^{(-)}(0,\tau')E_n^{(+)}(0,\tau)\rangle = 0, n = \pm1 \tag{3-4}$$

Equation (3-2-1) represents two types of processes: The terms coupling $E_{-1}^{(-)}$ ($E_{+1}^{(+)}$) with Q represent Stokes (anti-Stokes) scattering from ground-state (excited-state) molecules. The off-diagonal terms in the green matrix coupling $E_{-1}^{(-)}$ with $E_{+1}^{(+)}$ represent Stokes/anti-Stokes four-wave mixing, in which two pump photons are annihilated and a Stokes/anti-Stokes photon pair are created. Both of these processes drive the same collective molecular excitation Q. The phases of the initiating vacuum (zero-point) fields are temporally and spatially fluctuating, as shown in the delta correlation functions of

equation (3-4), which represents white noise in time and space. We could attribute this fluctuation to a thermal-like field distribution of the temporal-spatial modes (TSM) of the spontaneously emitted Stokes field, or equivalently to the thermal-like distribution of longitudinal spatial modes of the collective molecular excitation [47, 50]. The laser field further scatters from the collective molecular excitation creating additional anti-Stokes light. Subsequently, the initial white noise is heavily filtered under the high-gain transient conditions, since the gain process is a resonant one, and the Green propagators grow exponentially as the pulse propagates through the medium. The filtering or smoothing process eventually produces a Stokes and anti-Stokes field that are determined solely by a single TSM each; in other words, each has the form of a smooth, transform-limited wave packet with an overall phase and a peak amplitude that are random from one pump pulse to another. In this sense, these two fields resemble classical fields, that is, complex temporal envelopes with well defined carrier frequencies, although the intensities and phases of both fields dramatically fluctuate from one shot to another [21, 47, 51]. It is further known that if the scattering process goes into saturation, then the magnitude of the intensity fluctuations greatly decreases [52], although this is not accounted for in the linear theory considered here.

Next we examine the mutual coherence between generated first-order Stokes and anti-Stokes fields, in the high-gain transient regime. We calculate the correlation coefficient defined as

$$C = \frac{\left| \left\langle E_{-1}^{(-)}(L,\tau) E_{+1}^{(-)}(L,\tau) \right\rangle \right|^2}{\left\langle E_{-1}^{(-)}(L,\tau) E_{-1}^{(+)}(L,\tau) \right\rangle \left\langle E_{+1}^{(-)}(L,\tau) E_{+1}^{(+)}(L,\tau) \right\rangle} \qquad (3.5)$$

Because both fields in the numerator are negative-frequency ones, this gives the degree of phase anti-correlation between generated Stokes and anti-Stokes fields. Writing $I_{\pm 1} = \left\langle E_{\pm 1}^{(-)} E_{\pm 1}^{(+)} \right\rangle$, the phase correlation coefficient is proportional to the degree of mutual phase coherence, defined as $C_\varphi = \left| \left\langle e^{-i(\varphi_{-1}+\varphi_{+1})} \right\rangle \right|$, as is seen from:

$$C = \frac{\left| \left\langle \left| E_{-1}^{(-)} \right| \left| E_{+1}^{(-)} \right| \right\rangle \right|^2}{I_{-1} \, I_{+1}} \left| \left\langle e^{-i(\varphi_{-1}+\varphi_{+1})} \right\rangle \right|^2, \qquad (3\text{-}6)$$

if we assume that the fluctuations in intensities $\left| E_{\pm 1}^{(-)} \right|^2$ of first-order Stokes and anti-Stokes are independent of that of their phases. For example, if the temporal phase of the Stokes pulse is statistically independent of the anti-Stokes pulse, the C value (and C_φ) would be zero. Also, if the two fields' phases tend to be equal, then C would be zero. In contrast, if the sum of the phases of these two pulses stays constant from shot to shot (while they both fluctuate), which indicates phase anti-correlation, then C_φ would equal one, and C would be determined by intensity fluctuations alone.

By putting expressions from (3-2) into equation (3-6) and using the initial conditions (3-4), we calculate the C values under various conditions. The full expression is given in the Appendix A, as well as in our publication [53]. In Figure 3.1 we plot C values and Stokes and anti-Stokes intensities as functions of local time τ under the phase mismatch condition $\Delta\beta \times L = 10$, where the anti-Stokes intensity is maximized (see Figure 3.2). In all our calculations here we use 12 ns (FWHM) transform-limited Gaussian pump pulses,

and the Stokes and anti-Stokes integrated gain coefficients ($\alpha_{1,s}\alpha_{2,s}\int_{-\infty}^{\infty}dt\left|E_0(t)\right|^2 L$) are set

at the values of 25 and 30, respectively.

Figure 3.1. Pump and first-order Stokes and anti-Stokes mean intensities and their anti-correlation *C* as functions of local time.

We see in Figure 3.1 that the value of *C* nearly equals 1 throughout the duration of the generated Stokes pulses. Also note that the peak of the Stokes field is delayed by 4 ns relative to the peak of pump field, which is consistent with previously known results [27]. In Figure 3.2 we show the calculated *C* value at the peak of the Stokes-pulse intensity under various dispersion conditions, and find that its value stays close to 1. There we also

show the peak Stokes and anti-Stokes-pulse intensities versus phase mismatch, showing
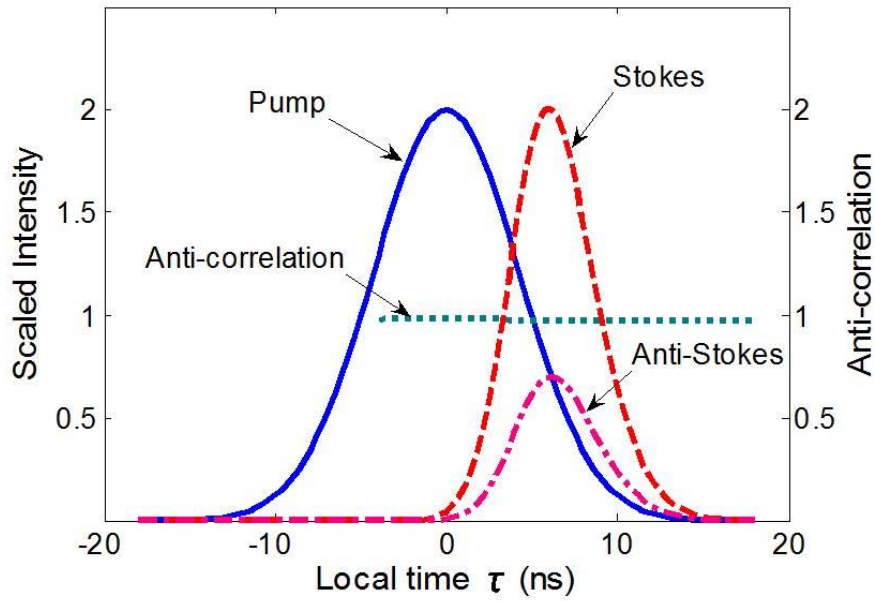
the well-known minimum that occurs for perfect phase matching [48, 49,54].
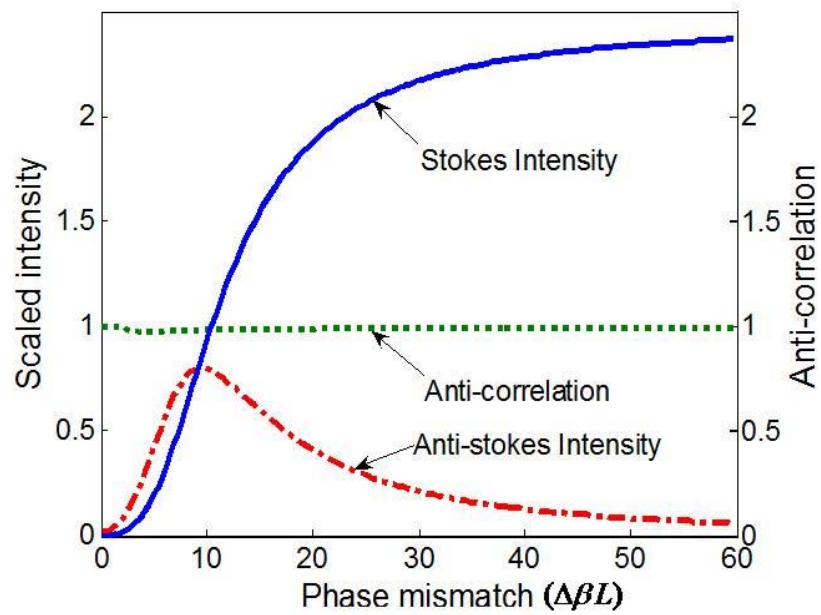
Figure 3.2. First-order Stokes and anti-Stokes mean intensities, and
their anti-correlation C as functions of phase mismatch.

The result $C \approx 1$ implies that the first-order Stokes and anti-Stokes are correlated in

the following way:

$$E_{+1}^{(+)} \approx \alpha\, E_{-1}^{(-)}, \qquad (3\text{-}7)$$

where α is a complex constant (with magnitude smaller than unity). This relation shows

that, not only the intensities of the two sidebands fluctuate in the same manner from pulse

to pulse, but their phases are near perfectly anti-correlated. This confirms one of our conjectures in [55]. It indicates a tendency in this system to automatically evolve toward perfect phase anti-correlation, although our experimental observations show that the anti-correlation is not perfect. A more rigorous model including all comb lines and pump depletion is needed for explaining this discrepancy.

The generated sideband fields are also correlated with the collective molecular excitation created in the medium, as seen in the solution (3-2-2). The quantity $\left\langle Q(L,\tau)E_{-1}^{(-)}(L,\tau)\right\rangle$, which is a measure of this field-medium correlation, is plotted in Figure 3.3 as a function of the local time τ. It shows a maximum in time, following the Stokes fields (see Figure 3.2). This correlation between field and molecular coherence has been studied in experiment for the case that Stokes only was generated [50]. In the absence of dephasing processes, this non-zero correlation can be considered as a manifestation of quantum state entanglement between the medium and the fields.
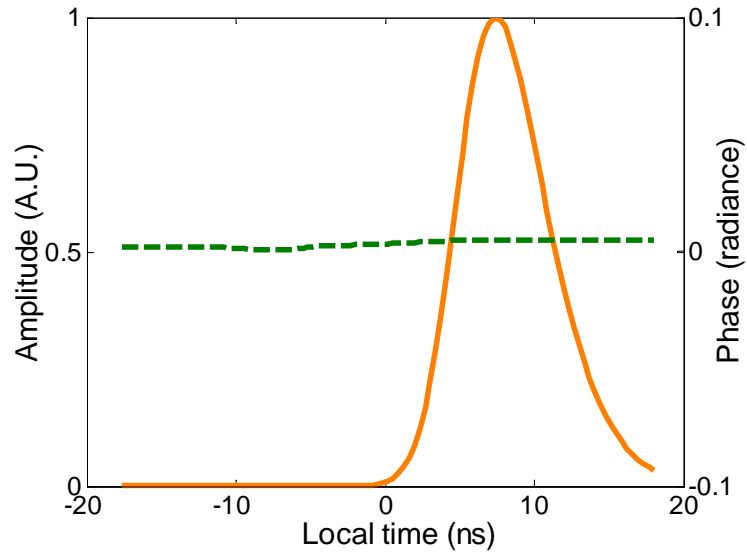
Figure 3.3. Amplitude and phase of quantity $\left\langle Q(L,\tau)E_{-1}^{(-)}(L,\tau)\right\rangle$. Phase value is with respect to the pump's phase.

Mechanism for phase locking

Here we provide a simple, intuitive model that helps explain the physical mechanism of the automatic phase anti-correlation between first-order Stokes and anti-Stokes fields predicted above. It also predicts the phase relations among all comb lines, a result that is further supported by the independent calculation in the following section. Equation 2-47 can be simplified by assuming perfect phase matching, since the phase mismatch does not strongly affect the phase anti-correlation, as shown in Figure 3.2. We treat the fields as classical random processes, and define real amplitudes and phases by

$$E_n^{(-)} = \left| E_n^{(-)} \right| e^{-i\theta_n}; \quad Q = \left| Q \right| e^{-i\phi'} . \tag{3-8}$$

This gives the evolution of the molecular polarization as:

$$i|Q|\partial_\tau\phi + \partial_\tau|Q| = \sum_{n=-N}^{N} \left|\alpha_{1,n}\right| \left|E_n^{(+)}\right| \left|E_{n-1}^{(-)}\right| e^{i(\theta_n - \theta_{n-1} - \phi' - \delta)} , \tag{3-9}$$

where we expressed the complex coefficient $i\,\alpha_{1,n}$ in terms of an amplitude and phase:

$i\,\alpha_{1,n} = \left|\alpha_{1,n}\right| exp(-i\,\delta)$. This gives two real equations:

$$\partial_\tau|Q| = \sum_{n=-N}^{N} \left|\alpha_{1,n}\right| \left|E_n^{(+)}\right| \left|E_{n-1}^{(-)}\right| \cos\left(\theta_n - \theta_{n-1} - \phi' - \delta\right)$$

$$\partial_\tau\phi' = \frac{1}{|Q|}\sum_{n=-N}^{N} \left|\alpha_{1,n}\right| \left|E_n^{(+)}\right| \left|E_{n-1}^{(-)}\right| \sin\left(\theta_n - \theta_{n-1} - \phi' - \delta\right) \tag{3-10}$$

The first equation in (3-10) implies that the molecular polarization grows at a maximal positive rate if $\theta_n - \theta_{n-1} - \phi' - \delta = 0$. In this situation, the second equation implies that the random phase ϕ' of the molecular polarization becomes time-independent, as the sin function goes to zero. This result is consistent with the established phenomenon of high-gain temporal filtering [50]. The idea is that the spontaneously generated comb lines can arise with any phase values, and the values that actually occur will be those leading to the highest overall gain, as indicated by the highest growth rate of $|Q|$. This highest gain also leads to time-independent phases with particular relations

among them. This is similar to self-mode locking in a laser. For compactness, this relation can be written as:

$$\theta_n - \theta_{n-1} = \phi ,$$
(3-11)

where $\phi = \phi' + \delta$ absorbs the constant δ into the random phase ϕ'. The random variable ϕ has uniform probability between 0 and 2π [51]. For the case of a strong pump in the n = 0 mode with phase θ_0, this relation implies for the anti-Stokes and Stokes phases, $\theta_1 = \theta_0 + \phi$ and $\theta_{-1} = \theta_0 - \phi$. These further imply perfect anti-correlation: $\theta_1 + \theta_{-1} = 2\theta_0$.

Now we can self-consistently solve for the phases of all comb lines from equation (3-11), referenced to the pump phase θ_0, giving

$$\theta_n = \theta_0 + n \phi .$$
(3-12)

This simple relation, while meant only to indicate the ideal limit of perfect phase locking (when phase mismatches are zero), is a useful guide in understanding the global behavior of the system.

Semi-classical Raman modulator model

Because Equation 2-46 describing all the Raman sidebands is difficult to solve, and the calculation in Section VI is only qualitative, we develop another supporting

simplified approach, which we call the semi-classical Raman modulator model. This non-perturbative model assumes that the vibrational coherence (polarization) in the molecules is spontaneously created by the first Stokes and anti-Stokes mode pair, and the higher-order sidebands are generated by the action of this coherence back on the pump. Unlike the analysis in the previous section, here we use detailed mathematic derivations which allow us to gain further insight into the phase relations of all Raman sidebands.

The Raman pump field can be written as the sum of two classical-field components:

$$E = E^{(+)}e^{-i\omega_0 t} + E^{(-)}e^{i\omega_0 t}, \tag{3-13}$$

where (dropping various constants) the equation of motion for the positive-frequency part is [56]:

$$\left(\partial_z + 1/\mathrm{v}_g \partial_t\right)E^{(+)} = iP^{(+)} = i\alpha(X)E^{(+)} \tag{3-14}$$

In the above equation we write the semi-classical electronic polarizability $\alpha(X)$ as a function of inter-nuclear coordinate X. Next, Taylor expand $\alpha(X)$ around the equilibrium coordinate origin X_0 and neglect the orders higher than the first term:

$$\alpha(X) \cong \alpha(X_0) + \left(\frac{\partial \alpha}{\partial X}\right)(X - X_0). \tag{3-15}$$

We discard the $\alpha(X_0)$ term, as it affects only the phase velocity of the electric field. We also ignore for now any phase velocity mismatching in this model. By changing to local time variable $z' = t - z / v_g$, equation (17) can be written as:

$$\partial_z E^{(+)} = i\alpha ' X \, E^{(+)},$$

(3-16)

where $\alpha ' = \left(\dfrac{\partial \alpha}{\partial X} \right)$.

The electric field at the end of the Raman medium ($z = L$) can be obtained by integrating the above equation:

$$E^{(+)}(L,t) = E^{(+)}(0,t) \exp\left(i\alpha ' \int_0^L dz' X(z',t) \right)$$

(3-17)

The X variable is related to the molecular polarization P created in the medium by [56]

$$\begin{aligned} X(z,t) &= P^{\dagger}(z,t)e^{-i\omega_{13}t} + h.c. \\ &= 2|p(z,t)|\cos\left(\omega_{13}t + \varphi(z,t)\right) \end{aligned},$$

(3-18)

where ω_{13} is the molecular resonance frequency, and $\varphi(z,t)$ is the random phase variable arising from the Raman process. By putting equation (3-18) into equation (3-17), we get

$$E^{(+)}(L,t)$$

$$= E^{(+)}(0,t)\exp\left(i\alpha'\int_0^L dz\, 2\big|p(z,t)\big|\cos\big(\omega_R t + \varphi(z,t)\big)\right) \tag{3-19}$$

$$= E^{(+)}(0,t)\exp\big(i\big|a(t)\big|\cos\big(\omega_R t + \phi'(t)\big)\big)$$

where $\big|a(t)\big|e^{i\phi'(t)} \equiv 2\alpha'\int_0^L dz\big|p(z,t)\big|e^{i\varphi(z,t)}$. We use a mathematical expansion for the

phase part of the above equation, i.e., $\exp(i\,x\cos(\beta)) = \sum_{n=-\infty}^{\infty} i^n J_n(x)\exp(i\,n\,\beta)$, and we

use $J_{-n}(x) = (-1)^n J_n(x)$ to re-write $J_n(x) = (-1)^n J_{|n|}(x)$. Then

$$E^{(+)}(L,t)$$

$$= E^{(+)}(0,t)\sum_{n=-\infty}^{\infty} (-i)^n J_{|n|}\big(\big|a(t)\big|\big)\exp\big(in(\omega_R t + \phi'(t))\big) \tag{3-20}$$

$$= E^{(+)}(0,t)\sum_{n=-\infty}^{\infty} J_{|n|}\big(\big|a(t)\big|\big)\exp\big(in(\omega_R t + \phi'(t) - \pi/2)\big)$$

If we write $\phi(t) = \phi'(t) - \pi/2$, then

$$E^{(+)}(L,t)$$

$$= E^{(+)}(0,t)\sum_{n=-\infty}^{\infty} J_{|n|}\big(\big|a(t)\big|\big)\exp\big(in\,\phi(t)\big)\exp\big(in\,\omega_R t\big) \tag{3-21}$$

We can identify the complex amplitudes of the Stokes and anti-Stokes lines as:

$$E_n^{(+)}(L,t) = E^{(+)}(0,t)J_{|n|}\big(\big|a(t)\big|\big)\exp\big(in\,\phi(t)\big)$$

We see that the first-order Stokes ($n = 1$) and anti-Stokes ($n = -1$) fields are predicted to have opposite phases, which is the same conclusion we derived earlier from the more rigorous quantum theory for the case of only two side bands. Equation 3-21 is similar to the one derived in reference [35], except that here only a single pump is used and the effects of quantum fluctuations (ignored in [35]) are paramount. More interestingly, equation 3-21 predicts that the higher orders of Stokes and anti-Stokes fields will have their temporal phases related to the phase of the strong pump (θ_0) by:

$$\theta_n = \theta_0 + n\,\phi(t)\,. \tag{3-22}$$

Under high-gain transient conditions, the phase $\phi(t)$ will be essentially constant during a single pulse, as discussed above. Therefore, this prediction is the same as obtained in equation (3-12) using a distinct and more qualitative argument. It can be understood, since higher-order sidebands arise from multiple scattering from the Raman medium. Each time the field gets scattered, the Raman medium will impose a ϕ phase shift onto it.

Prospects for ultrashort pulse generation

Combining the ideal relation (3-22) with the frequency relations (2-2), we find that the generated comb spontaneously satisfies the required relations for Fourier synthesis to create a periodic waveform. In order to see that, express the synthesized waveform as:

$$E^{(+)}(t) = \sum_n \left|E_n^{(+)}(t)\right| e^{i[(\omega_p + n\omega_{13})t + n\phi + \theta_0]} = e^{i\omega_p t + i\theta_0} \sum_n \left|E_n^{(+)}(t)\right| e^{in(\omega_{13}t + \phi)} , \qquad (3\text{-}23)$$

where we assumed $\phi(t) = \phi$ is constant during a given pulse (although random shot to shot). The intensity will be determined by the summation term, which is invariant with period $T = 2\pi / \omega_{13}$ under the assumption tshat E_n is a slowly changing envelope compared to that period.

However, the carrier-envelope phase (CEP) of the synthesized waveform is changing, as we can see from equation (3-23), in which the term $e^{i\omega_p t}$ is generally not invariant over period T. This situation is simulated in Figure 3-4 (*a*), using six Raman modes. If the pump is tuned and stabilized to a multiple of the molecular resonance frequency, i.e., $\omega_p = m\,\omega_{13}$ (*m* is an integer), then one set (train) of periodic pulses with constant CEP will be created within one pump pulse. On the other hand, because the quantum phase ϕ changes from shot to shot, the pulse trains within successive laser shots will not have the same waveform and will not be comprised of isolated short pulses. This change of CEP phase is illustrated in Figure 3-4 (*b*) and (*c*). Further locking mechanisms, such as coherent injection of molecular coherence, have been used to overcome this limitation, and stable ultrashort pulse trains were created, with the cost of added experimental complexity [37].
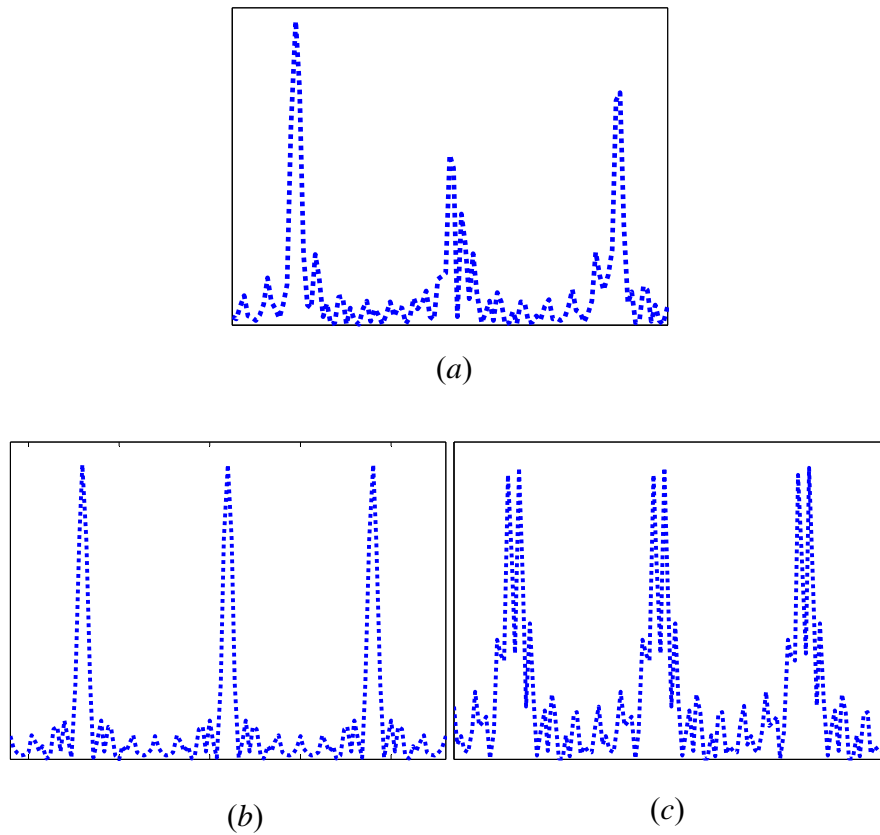
Figure 3.4. Simulated short pulses under different conditions. *a*) $\omega_p \neq m\,\omega_{13}$. *b*) $\omega_p = m\,\omega_{13}, \phi = 0$. *c*) $\omega_p = m\,\omega_{13}, \phi = \pi/6$. From (*b*) and (*c*) it clearly shows the change of carrier-envelope phase in the synthesized pulses.

We are presently exploring whether simultaneous pumping of the medium by a fundamental pump and its phase-locked second harmonic, as in [37], but without external injection of coherence, can also lead to stable ultrashort pulse trains by a generalization of the phase locking discussed in the present Chapter. If the frequency of the fundamental pump is tuned to be precisely an integer multiple of the molecular resonance frequency, the frequency-doubled pump will be resonant with one of the anti-Stokes fields of the

original pump. For example, if we choose hydrogen molecules as our Raman medium, the vibrational resonance frequency is around 125 THz [39]. We can tune the pump to about 375 THz (or 802 nm), which is in the range of commonly used Ti-sapphire lasers. The frequency-doubled pump (401 nm) will be resonant with the third anti-Stokes field of the original pump, and will have a deterministic temporal phase $\Delta\varphi$ relative to the pump. Both the pump and its frequency-doubled beam will simultaneously interact with hydrogen molecules to generate the comb. The question is whether this will deterministically lock the temporal phase difference among adjacent comb lines, which is ϕ in equation (3-22), to the value $\Delta\varphi/3$, the only value that allows a self-consistent phase anti-correlation between all comb lines. The produced periodic single-cycle pulse trains will then be identical upon subsequent pump pulses.

CHAPTER IV

OPTICAL RAMAN COMB GENERATION

Hollow-core Photonic Crystal Fiber

The hollow-core photonic crystal fibers (HCPCF) that we used in our experiments were fabricated by and generously provided by Dr. Fetah Benabid and his research group at the University of Bath in the UK. HCPCF consists of a large air hole in the "core" area, and a periodic 2-D crystal structure-like lattice as the fiber's cladding. By using HCPCF, we can fill it with Raman active gases, such as hydrogen or CH_4, at various pressures. Also, HCPCF has shown broadband transmission from ultra-violet to infrared. This multiple octave span in wavelength will be greatly useful in generating the optical Raman frequency comb that is wide enough for the atto-second pulse to synthesize.

Although I do not make the HCPCF myself, I would like to briefly describe the process involved in making it [57, 58], which has the following three-stage drawing: In the first step, a hexagonal unit cell on a macroscopic scale is formed by drilling a hole down the length of a silica rod. In a typical photonic crystal fabrication process, the diameters of the hole and the rod are 16 mm and 30 mm, respectively [57]. Six flats are

then milled on the outside of the rod, forming a regular hexagon. In the second step, the preform of a hexagonal unit cell is drawn on a fiber drawing tower at a certain temperature and pressure to produce hexagonal cane of a diameter at the order of 1mm, which is cut to short lengths and stacked to give the required crystal structure. This hexagonal cane of a small diameter is usually called a "thin capillary." In the third step, the stack of capillaries forming a certain crystal structure is again drawn on the tower, fusing the stacked canes together and reducing the pitch (center-to-center spacing) to a certain small value. Finally, a piece of this fused stack is drawn down again to yield the final fiber.

The crystal structure of the HCPCF that we got and used in our experiment from the University of Bath is called a Kagome structure, and it has a large hole (about 20 microns) in the center. The fabrication technique to introducing such a core defect is applied in the second step, where shorter capillaries are stacked on both sides of the capillary, leaving a gap in the middle. During the cane-pulling process (the third step), no cladding or core pressurization is applied. The drawing temperature is kept low in order to form the Kagome structure. During the fiber-drawing process (the final step), the integrity of the structure is preserved by independently pressurizing the core, the cladding, and the region separating the jacket tube from the cane. Moreover, to maintain the structure's air-filling fraction, the Kagome fiber is drawn at a low temperature, high-preform feed rate, and high drawing tension. Figure 4.1 shows the scanning electron microscope of the transverse structure of the Kagome fiber, after the fiber has been cleanly stripped and cleaved.
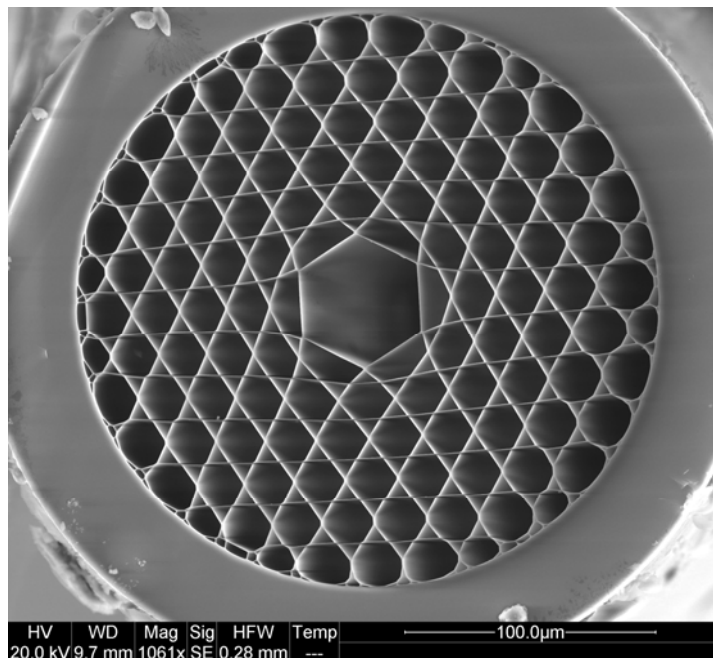
Figure 4.1. SEM picture of Kagome fiber after it has been cleaved

The guiding property of HCPCF is usually explained by the theory of the two-dimensional photonic band-gap (PBG) [58]. From geometry optics, the wave vector component along the fiber, known as the propagation constant β, determines whether light propagates or is evanescent in any part of the guide. Conventional total internal reflection (TIR), where the index n_1 of the core is greater than index n_2 of the cladding, ensures the existence of a range of β where light is propagating in the core while being evanescent in the cladding. In contrast, light can be confined between two multilayer dielectric stacks in a core of arbitrary refractive index, if the stacks have a periodic Bragg grating (PBG) for a range of β at a given optical frequency. There are two regimes of

PBG guidance. In the first regime, light propagates in the layers with high index n_1 of the dielectric stack but is evanescent in the layers with low index n_2. The high-index layers act as individual TIR waveguides, supporting bound modes at specific values of $\beta = \beta_m$. Resonant tunneling between adjacent high index layers permits the leakage of light through them, provided β lies within the pass bands that open up around each β_m. The widths of the pass bands depend on the strength of coupling between the layers. Between the pass bands lie band gaps; if a high-index core layer with a different (maybe smaller) width supports a mode with β inside a band gap, it is not resonant with the other layers and light leakage by tunneling is frustrated. The mode is thus strictly guided by the frustrated tunneling form of PBG. In the second regime of PBG guidance, light can propagate in all layers ($\beta < k\, n_2$). Band gaps occur at the Bragg condition as a result of multiple scattering and interference, leading to the Bragg form of PBG guidance.

The Kagome fiber, although it belongs to HCPCF, relies on a new photonic guidance whereby photons are confined not by PBG but rather via a mechanism akin to Von Neumann-Wigner bound states [59, 60] within continuum, where the fiber-guided modes cohabitate with those of the cladding without notably interacting. This "inhabited interaction" between the hollow core-guided modes and the cladding continuum is explained by the high degree of the transverse-field mismatch between the core and cladding modes [39].

The guiding property of a Kagome fiber is mainly determined by its pitch (Λ), core size, strut width and air-filling fraction. The fiber that we used in the experiment and will discuss throughout this chapter has a single core air hole with a diameter of 20 microns

and has a large pitch at 12 microns. The transmission curve of the fiber measured with a white light laser source is shown in Figure 4.2. It clearly shows the typical broadband transmission from the visible to infrared region.
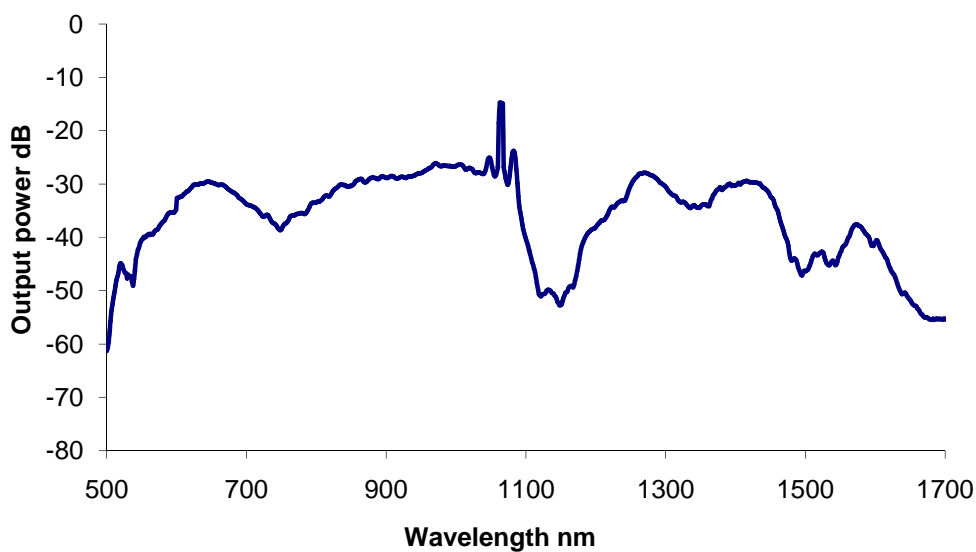

Figure 4.2. Broad transmission of Kagome fiber

Gas-loading cell

We designed a gas-loading cell by using commercially available materials or parts with little requirement of machining. I would like to specially thank Cade Gladhill for purchasing all the required parts, assembling them and performing the leaking test of the cell.

Figure 4.3 shows the detailed drawing of the cell. The main part of the cell is a 3/8"
female pipe thread tee. The input end is connected with another pipe thread tee where a
hydrogen gas tank and a pressure gauge are attached. One output of the female pipe
thread tee is connected with a pipe-thread (3/8") to a VCO (1/2") adapter. A 3 mm thick
optical window (BK7) is put inside a VCO-type nut, and this output end is sealed by
capping the nut, which essentially pushes the window firmly against the o-ring that is
built inside the VCO adapter. In the other output end, where fiber will be loaded, a 1/8"
Swagelok straight fitting to a 3/8" pipe thread is directly attached. In order to seal this
end, a graphite ferrule with a .5 mm OD capillary is used. When loading the fiber into the
cell, one first inserts the un-cleaved fiber through the Swagelok nut, and then through the
ferrule carefully. Next insert the fiber into the Swagelok fitting that is already attached to
the pipe thread tee, and push the fiber through the pipe until it hits a plastic fiber guide
placed inside the VCO adapter. This fiber guide is the only self-machining part in the
design of this gas-loading cell. It has a center hole that is large enough to allow fibers to
go through. The purpose of this fiber guide is to support the fiber against its gravity.
Several small holes are drilled around the center hole in the fiber guide so that gas can
still be filled with the whole pipe thread tee. Special care should be taken so that the fiber
is inserted through the center hole of the fiber guide, instead of the small holes around it.
After the fiber end appears on the other end (window is not put on at this time), carefully
thread the Swagelok nut with the ferrule placed inside. This end should stay loose, so that
the fiber still can be pulled from the other end and then cleaved. After cleaving, pull the
fiber end back through the cell until its tip is inside the VCO fitting but outside the fiber

guide. Cap the VCO nut with the window placed inside, and finally, use a tool to tighten the Swagelok nut (a quarter turn after hand-tightening is enough). Figure 4.4 shows the cell before being assembled.
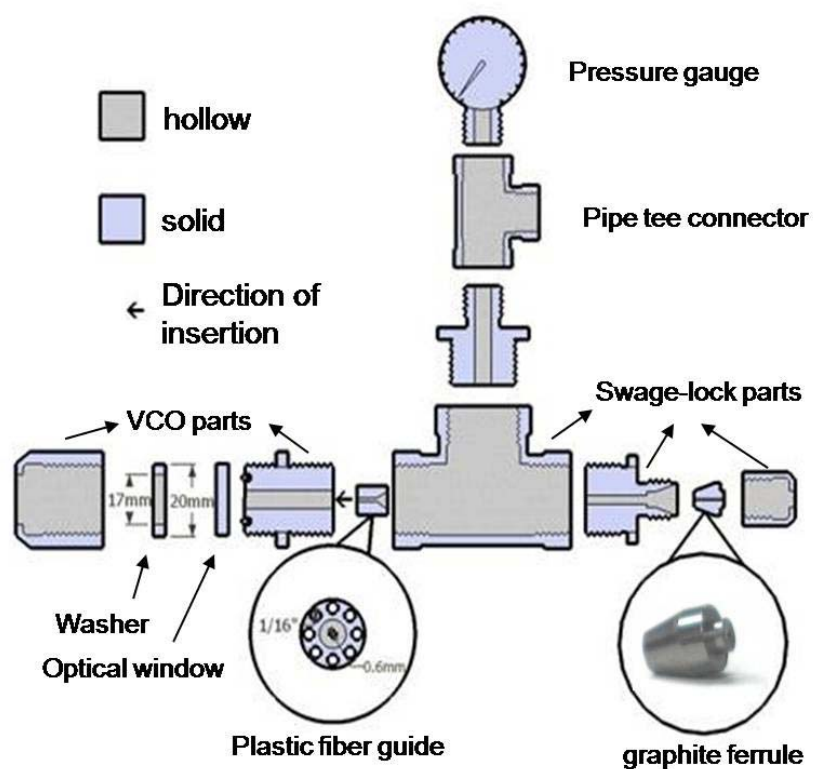

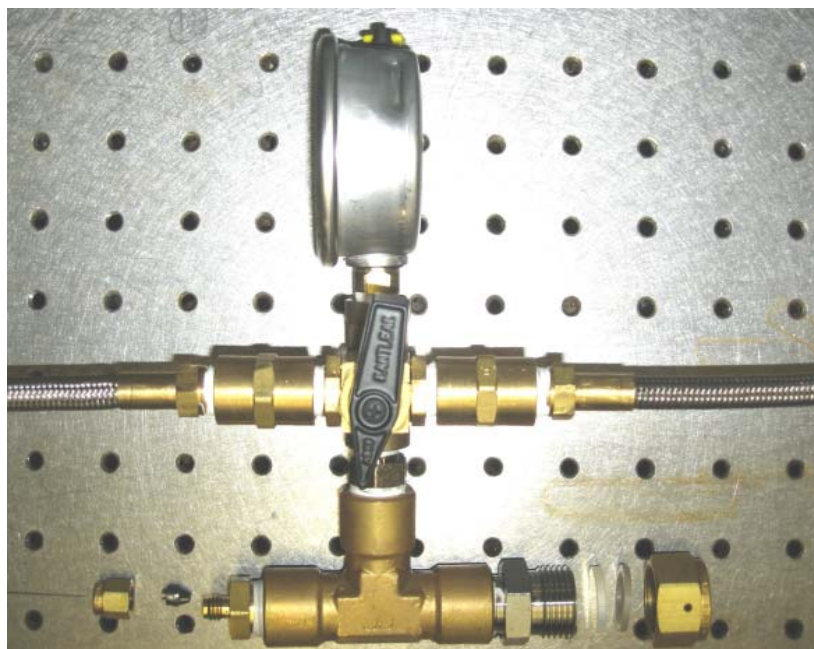Figure 4.3. Detailed drawing of the gas loading cell

Figure 4.4. Experimental picture of gas loading cell

Optical Raman frequency comb generation

in HCPCF filled with hydrogen gas

    The experiment setup to generate and observe the optical Raman frequency comb from hydrogen gas is shown in Figure 4.5.
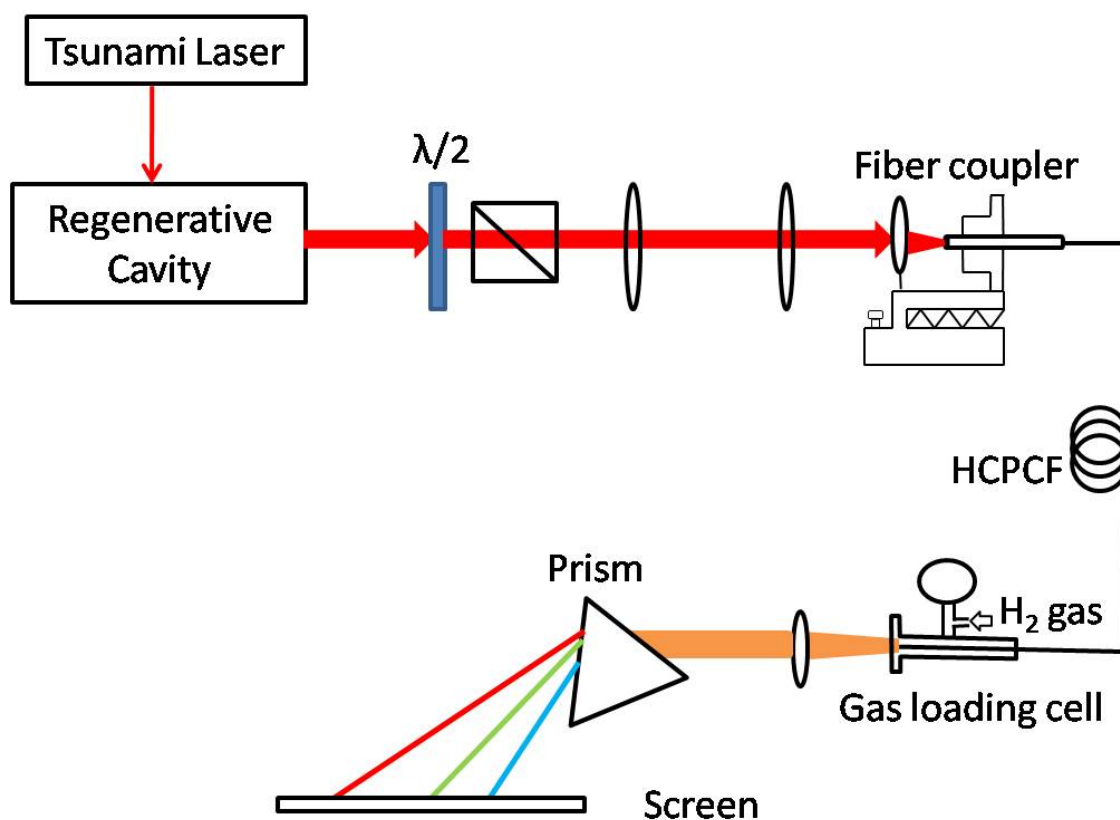
Figure 4.5. Experiment setup for observation of Raman optical frequency comb

The light source we use is from a mode-locked Ti:Sappire laser (Spectra-Physics, Tsunami) pumped by CW diode-pumped laser (Spectra-Physics, Millennium Pro) at 532 nm. The laser produces near 200 pico-second (ps) pulses at 80 MHz repetition rate. The output pulse of the laser is monitored by two pieces of equipment: one is an ultra-high-resolution wave-meter (Burleigh 1600) and another one is a high-speed photo-detector (25GHz, New Focus 1437). The wave-meter displays the center wavelength of the pulse to the accuracy of 10^{-4} nm (calibrated by Rubidium 87 D1 transition). The fast photo-diode measures the temporal shape of the pulse, and ensures that the Ti:Sapphire laser is

properly mode locked. A typical trace of the pulse is shown in Figure 4.6. We confirm the pulse is near transform limited by measuring its spectra width using a Fabre-Perot interferometer (Burleigh F-140). The product of temporal width and spectra width is 0.45, close to the Gaussian limit of 0.44.
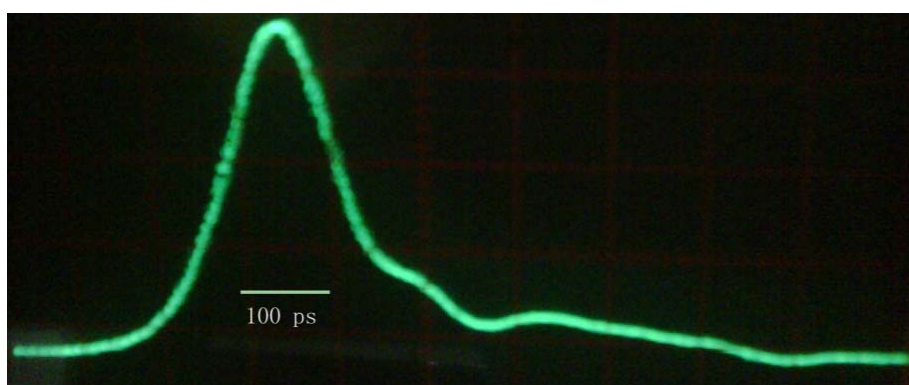

Figure 4.6. Temporal shape of ultra-short pulse. FWHM of the pulse is about 200 ps

The laser pulse from Tsunami is then sent into a regenerative (Regen) cavity, which will amplify the peak intensity of the pulses by a factor of a million. This Regen cavity itself is a Q-switched Ti:Sapphire laser system, pumped by a 5 kHz pulsed Nd:YLF laser (Positive Light, Merlin). The working principle of this Regen cavity is that, every time its pump laser at 5 kHz fires and excites its gain medium, only one pulse from Tsunami's 80 MHz pulse train is picked into the high-Q mode of the cavity. All other pulses from Tsunami will be dumped out of the Regen cavity immediately. The picked pulse will travel inside the Regen cavity many times, and each time it is amplified when passing through the medium. When the pulse cannot be further amplified – that is, gain saturation

occurs – the cavity is switched to low-Q mode and thus the amplified pulse is ejected out of the Regen cavity. A combination of an electro-optic modulator (EOM) and a thin-film sheet polarizer inside the cavity is used as a Q-switcher to pick and eject the pulse. The timing of EOM is precisely controlled by a four-channel digital delay generator (Stanford Research DG535). The output of the Regen cavity is an intensified pulse with 160 micro-joules per pulse at a 5 KHz repetition rate. Details of this Regen cavity configuration can be found in [61].

The pulses from the Regen cavity first go through a half-waveplate and a polarizer so that they are linearly polarized in a horizontal direction, and then collimated by a pair of lenses (300 mm and 100 mm focal length, respectively). We use a 35-mm, anti-reflection doublet aspheric lens (Edmond Optics) coated for near IR (700 nm -1100 nm) to couple the light into the HCPCF. Usually the fiber length is about 1.5 meters. The output of the fiber is then collimated by another doublet lens at 60 mm. An equilateral dispersive prism is used to disperse the collimated output, whose spectrum is then projected onto a distant screen for easy viewing.

In the experiment, we seal one fiber end with the home-designed hydrogen gas-loading cell, and leave the other fiber end open. The hydrogen gas is then pressurized into the loading cell, typically between 5 and 15 bars, and then diffused into the HCPCF. Since the output end is open, we can imagine there are hydrogen molecules blowing out from that end. However, since the fiber transverse area (<100 microns) is very small compared to fiber length (typically at 1.5 meters), the flow rate of hydrogen gas is very low. In the experiment, we never notice the hydrogen gas leaking from the open end.

The Raman frequency shift ω_{13} of hydrogen gas has slight dependence on gas pressure, and has been found in a previous experiment as [62]:

$$\Delta\omega \text{ (GHz)} = 9.6 \times 10^{-2} \times \text{pressure (bar)} .$$

When hydrogen gas is set at 15 bars, ω_{13} is estimated to shift by 1.4 GHz from the above equation. This shift is still smaller than our laser's linewidth (2.2 GHz). We normally just neglect the impact of this small shift in our later experiment.

The Raman optical frequency comb that we observed in our lab is shown in Figure 4.7. To generate such a spectrum, we put an extra quarter-wave plate before the pulses are coupled into the HCPCF, so that the Raman pump pulses are circular polarized. The spectrum shown then is the hydrogen rotational line, which has line separation at 18 THz. In order to show the spectrum, we use a standard digital camera to record the picture of the spectrum scattered off the screen. The figure shows many high-order anti-Stokes lines in the deep blue region, but fewer Stokes lines. This is because the Stokes lines are in an infrared region, and the camera has poor or no response in this spectral region. We estimate the pulse intensity required to generate such a spectrum is about a 5-10 μJ / pulse, when the gas cell is kept at the pressure of 200 PSI. This required pump intensity is much lower than the 1 mJ / pulse that is usually required in free-space setups.
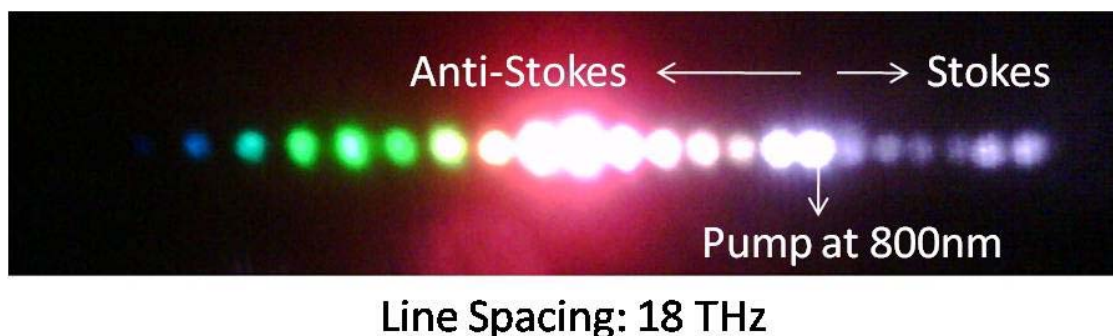
Figure 4.7. Hydrogen rotational comb

In our later experiment, we take out the extra quarter-wave plate and couple the linearly polarized pump pulses into HCPCF, which will excite the molecular vibrational state in hydrogen gas. The frequency shift in this case is very large, about 125 THz. In Figure 4.8, it shows the comb that we observe on the screen. In order to illustrate the first-order Stokes at a wavelength of 1200 nm, we have used our IR viewer device, which is responsive from 1100 nm to 1700 nm. The second-order Stokes, however, is at 2200 nm, and we cannot show it in the figure. For anti-Stokes fields, we observe up to 3 orders. Their wavelengths are 602 nm, 488 nm and 401 nm, respectively. We label those Raman comb lines with integer numbers, as we discussed in Chapter II. Stokes orders are negative integers, and anti-Stokes orders are positive integers.

Another feature we can see from this Raman comb generation in gas-filled HCPCF is that the output from the fiber after collimation shows a near Gaussian-like spatial mode for almost every comb line, except those high-order anti-Stokes lines near the blue region. This shows that the HCPCF helps to produce single spatial mode Stokes and anti-Stokes in the comb. Since the effective cross-section of the HCPCF is only 20 microns, our

assumption in Chapter II that the Fresnel number of the Raman interaction is smaller than
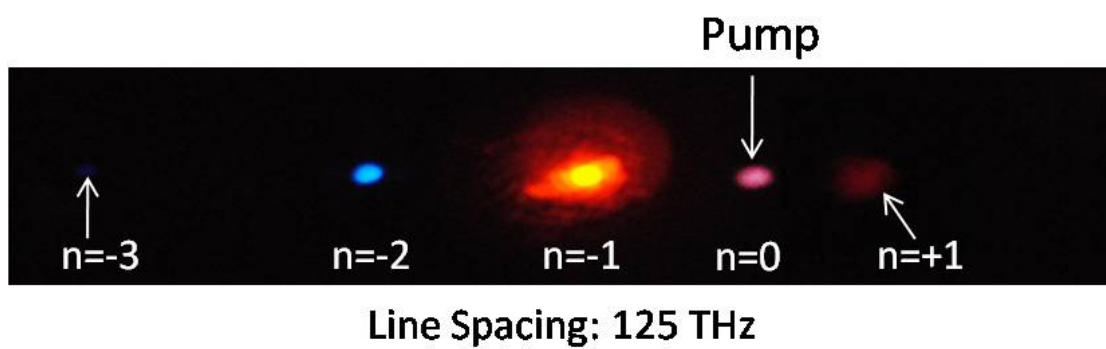
unity is valid.

Figure 4.8. Hydrogen vibrational comb

CHAPTER V

EXPERIMENTS AND RESULTS OF PHASE

CORRELATION MEASUREMENT

Energy statistics of generated first-order Stokes field

The Raman optical frequency comb shown in the previous section is generated by 200 ps optical pulses. The interaction between the optical pulse and the hydrogen molecules are in the so-called transient regime, where the molecular dephasing time T_2 is much longer than the pulse duration. Typically this T_2 for hydrogen molecules are in the order of 1 nanosecond. In reference [63], it is shown that transient regime can be satisfied even when the pulse duration is longer than dephasing time T_2 under ultra-high gain condition. If the steady-state Raman gain is denoted as G_{ss}, then for a pulse duration shorter than $G_{ss}T_2$, the interaction is said to be under transient regime.

In the experiment we measure the energy statistics of first-order Stokes (vibrational line, wavelength at 1200 nm) to verify that our comb generation is under transient regime, and also no photon at Stokes wavelength is seeding the process. In other words, the first-

order Stokes field is generated by quantum initiation and amplification through the co-propagation with the pump.

The experiment setup is similar to the previous chapter where hydrogen vibrational comb lines were observed, which is shown in Figure 5.1. We placed an IR Complementary metal–oxide–semiconductor (CMOS) linescan camera after the prism to detect the signal, including both the first-order Stokes field and the pump field.
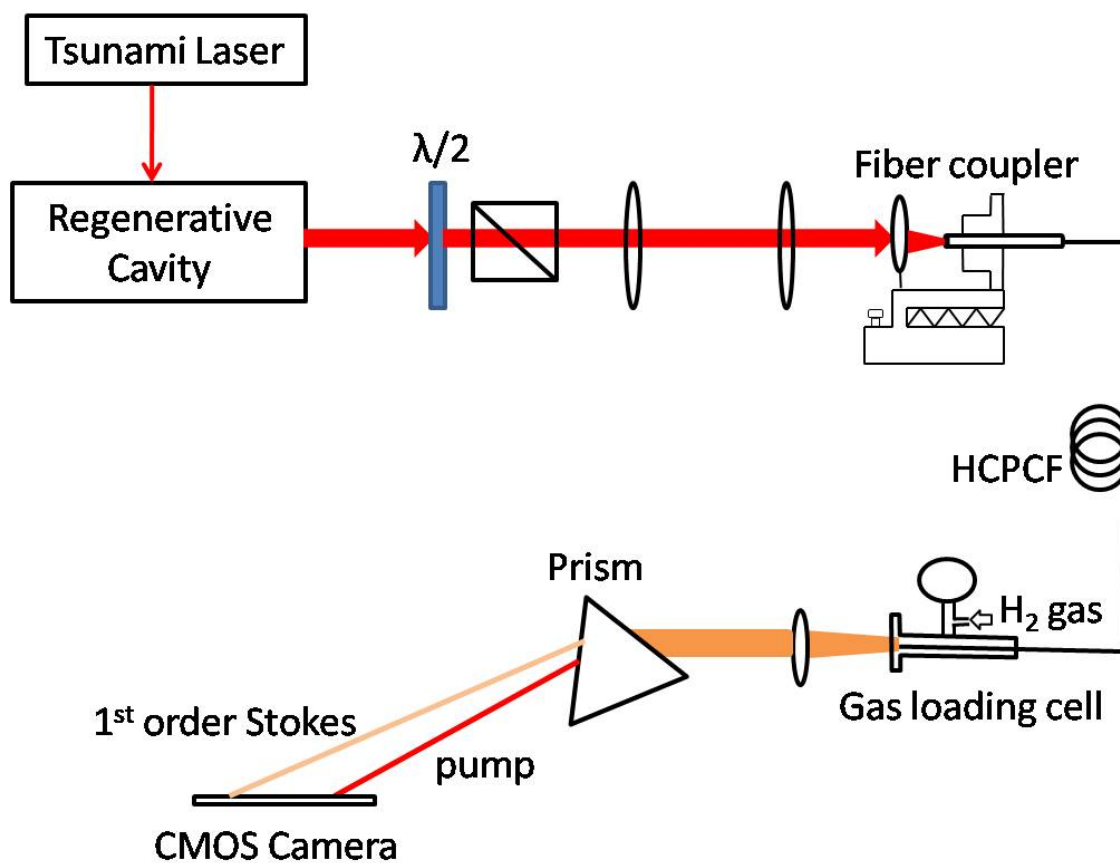

Figure 5.1. Experiment setup for measuring Stokes pulse energy statistics

This CMOS linescan camera was purchased from Photon Control, Inc. It consists of a Hamamatsu InGaAs CMOS array detector and an electronic driver board that will allow the detection under external triggering mode. The detector itself has 512 pixels, and each pixel is 25 μm × 125 μm. Its spectral response is from 800 nm to 1650 nm. The detector also has a very fast integration time, which can go down as small as 1 μs. We set the detector at the external triggering mode, where the trigger signal is directly from the pump laser. In this setup, once the detector received a low-to-high TTL signal, it will start to integrate (count the photons hit on each pixel) for certain amount of time (integration time), and then automatically shut down for some time (several milliseconds) to read out the data on each pixel. This read-out process is usually called 'binning.' After it finishes transferring data to the built-in memory, the detector will send a "data ready" signal to the computer via the USB-connection cable. The computer will then read the data from the detector's memory and display it on the monitor. After reading the data, the computer will signal the detector and the detector will clear its memory and zero any electrons that are accumulated on each pixel during the blackout period, and wait for the next available trigger signal to start its next operational cycle.

In this way, we can detect the dispersed single-shot first-order Stokes and pump field if we set the detector's integration time shorter than the time between consecutive pulses, which is at about 200 μs. In the experiment, we set this integration time at 180 μs. The frame rate of the camera is about 100 Hz, mainly limited by its data-binning and transfer speed. The CMOS detector array is slightly different from the charge coupled device (CCD) version, in that each pixel on the CMOS detector has its own amplifier, while all

pixels on CCD detector share one amplifier. Therefore, CMOS has a limitation on its response linearity of all pixels. In our CMOS detector array, the specification of linearity is better than 95%.
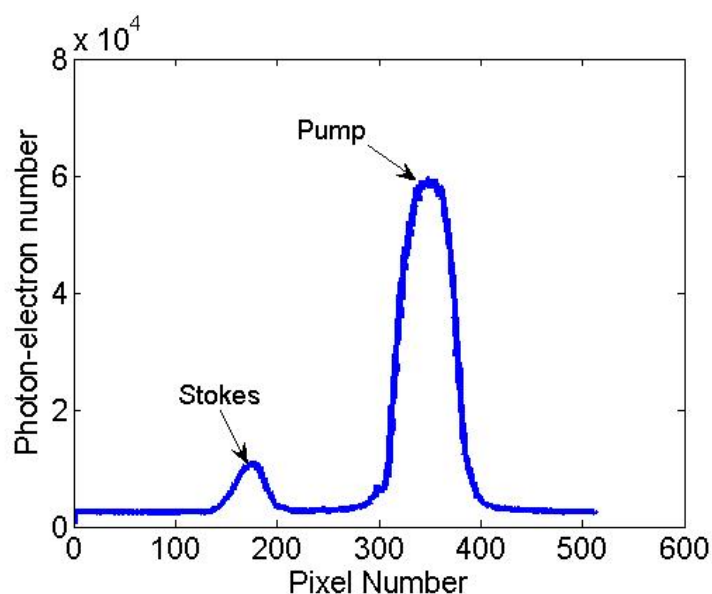

Figure 5.2. Single-shot first-order Stokes and pump signals

In Figure 5.2 we show the typical single-shot Stokes and pump signal recorded on the CMOS linescan camera. We adjusted the beam height so that the array detector (horizontal line) is centered across the beam. We also use neutral density filters to attenuate the beam to prevent any saturation on the camera's pixels. The beam sizes of the first-order Stokes and pump are a little different shown from the data image. This is because the numerical aperture of the HCPCF is not all the same for different colors of light.

In the experiment, we keep the pump's intensity low so that only the first-order Stokes is present. No other comb lines can be observed by the eyes. In this way, we can compare our measurement with previously known results for the stimulated Raman scattering [21]. The histogram showing the probability distribution of the Stokes pulse energies is plotted in Figure 5.3. In this figure, we analyze 300 total recorded camera shots, and the peak value of the Stokes pulse in each shot is extracted to represent the Stokes pulse energy. We can see that the histogram shows negative exponential distribution for the Stokes pulse energy, i.e., the most probable Stokes energy is near zero. This statistical feature of Stokes energy shows great fluctuations from one shot to another, and is directly related to the vacuum initiation of the Stokes field. In quantum optics, the exponential decay distribution is related to the Bose-Einstein distribution, where the probability can be written as [64]:

$$P(E) = \frac{1}{(1+\langle E \rangle)(1+1/\langle E \rangle)^E} .$$

In the above equation, $\langle E \rangle$ is the mean of Stokes pulse energy. The distribution peaks at zero. However, when there is saturation, the above formula will no longer be valid. That's the main reason we kept our pump intensity low in our experiment.

However, it has also been shown that, even when $\langle E \rangle \to 0$, the Stokes energy distribution might deviate from a negative exponential to Gaussian. This is when the generated Stokes pulse has several spatial and temporal modes (i.e. wave-packet modes). Although each mode obeys a negative exponential distribution, the overall behavior of

Stokes energy statistics will then converge to a Gaussian distribution. An easy way to see this effect is by using the analogy of the central limit theorem in classical probablity theory. A detailed review on this topic can be found in [27]. Since our experiment shows that the Stokes energy distribution is close to a negative exponential, the generated Stokes field is in a single temporal and spatial mode. In other words, the Stokes field is close to Fourier-transform limited pulse with a well-defined temporal phase. In the next section, we will see that this temporal phase is also random from shot to shot due to the quantum initiation process of the Stokes field.
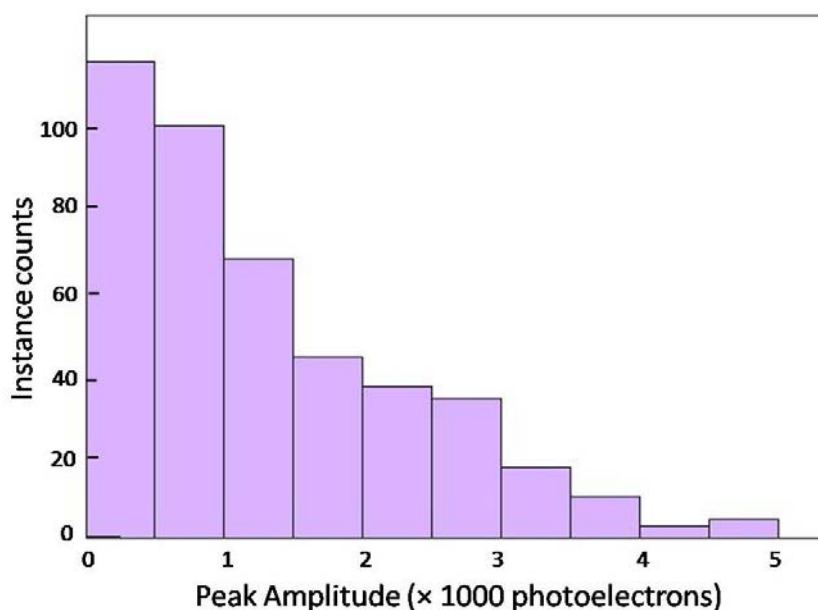

Figure 5.3. Intensity statistics of first-order vibrational Stokes

In Figure 5.4 we also show the energy statistics of the pump laser. This plot is to confirm that the large energy fluctuation of the Stokes field is not caused by the pump's

intensity instability. In fact, the pump is very stable during the experiment, and its estimated fluctuation is about 2%.

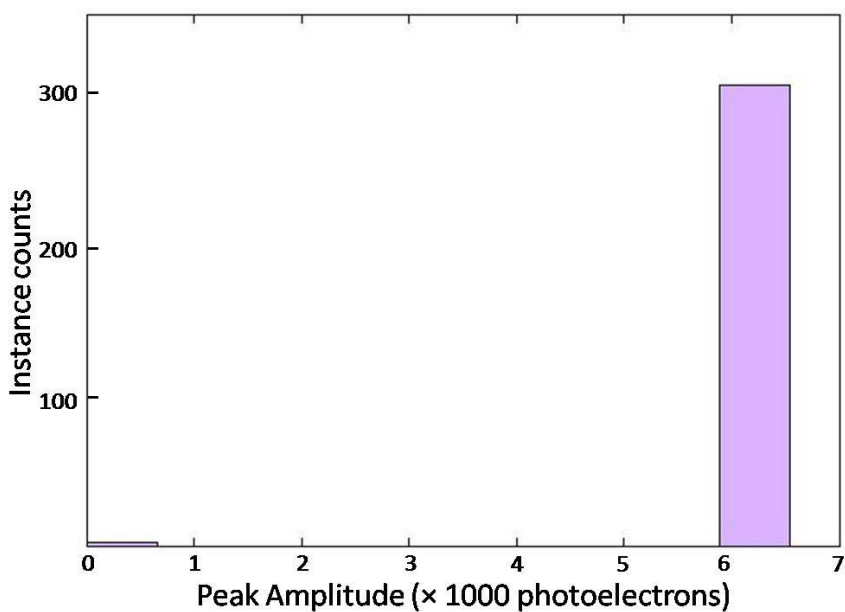Figure 5.4. Intensity statistics of Raman pump

Self-coherence of the comb lines

Under low pump power level, we find the generated Stokes pulse is temporal coherent by measuring its pulse energy statistics. When the pump power is strong enough for Raman optical frequency comb generation, we have to test the temporal and spatial coherence of the Stokes field another way. Here we introduce a two-fiber experiment

where we interfere the same comb components generated independently from two fibers. This technique was first used for Raman studies in "bulk" gas cells by Kuo et al [51]. The high-visibility and random interference fringe phase indicate that the generated comb lines are temporally coherent but have a random phase.

The experiment setup is shown in Figure 5.5. The pump pulse is again the output from the Regen cavity with 200 ps temporal duration. It is split by a non-polarizing beam-splitter (BS-A) into two parts, and each part is then coupled into a hydrogen-gas filled, 1.5 meter-long HCPCF. The output of each HCPCF is then collimated by a pair of lenses, which will ensure both outputs have similar beam diameters. These two beams are combined by a small angle on a non-polarizing beam splitter (BS-B), and a narrow band filter is placed in each output of the beam splitter to filter out single Stokes or anti-Stokes line. A CCD or CMOS camera is placed afterwards to capture the interference fringes.

It is obvious that from BS-A to BS-B the alignment is a well-known Mach-Zander interferometer. Each arm of this interferometer contains an HCPCF. In order to see interference fringe on the camera, the distance of these two arms should be balanced, so that the light pulses would overlap in the time domain.

Before the hydrogen gas is pumped into the HCPCF fiber, we test the balance of the two arms by overlapping two pump beams transmitted from each fiber onto a non-linear semiconductor photodetector. The intensity-squared dependence of the voltage signal generated by the detector has a cross term depending on the two pump beams intensity and their temporal overlap. This cross term is non-zero only when the temporal difference between two pumps is smaller than the pump's duration, and will be peaked when this

difference is perfectly zero. This cross-term signal is much more easily detected than interference fringes, since it does not depend on the phases of two pumps. We place a manually adjustable delay stage in one arm of the interferometer to fine-tune the distance difference.
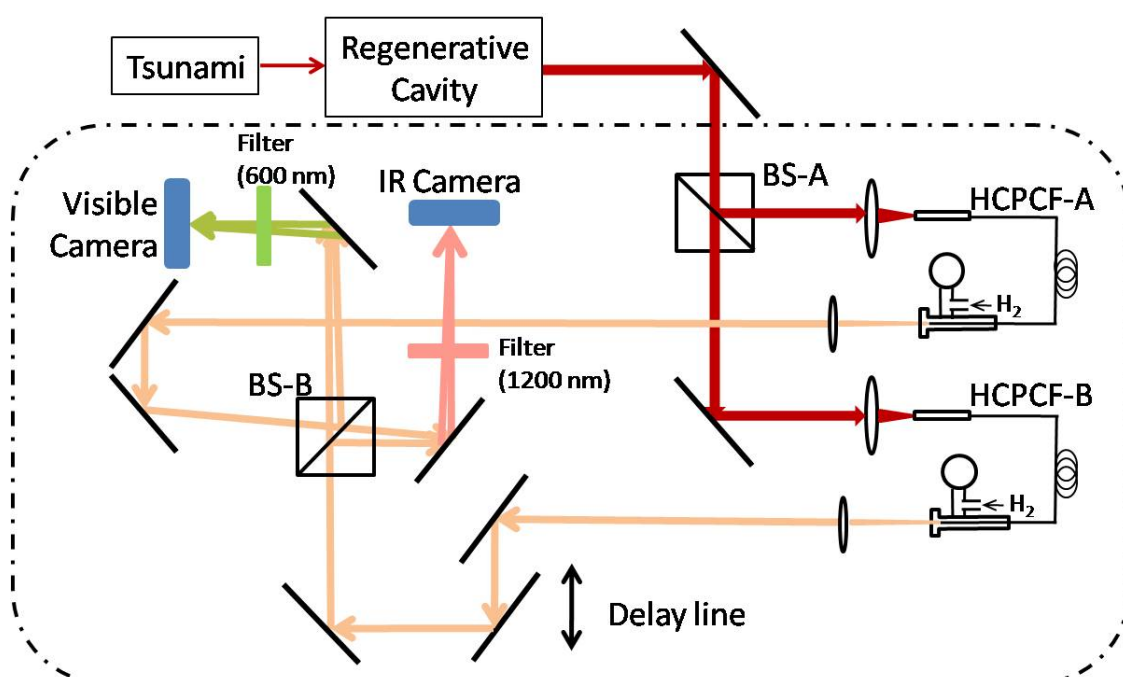

Figure 5.5. Experiment setup for observation of interference fringes from two Raman optical frequency combs. The dash-dotted bracket indicates the two fiber interference setup.

After we balanced the two arms of the interferometer by using an optical delay line, we observed the interference fringes on the linescan detector. Mathematically, the fringe can be expressed as:

$$I(x) = \int dt \left\{ \left| E^{(1)}(x,t) \right|^2 + \left| E^{(2)}(x,t) \right|^2 + 2E^{(1)}(x,t)E^{(2)}(x,t) \times \cos[(\Delta k x]) \right\}, \qquad (5\text{-}1)$$

where the superscript denotes the fiber and Δk is the wave vector difference of the two fields projected on the x direction in which the array detector extends. This difference determines the fringe spatial frequency and can be controlled by adjusting the angle between two beams when they are combined on the array detector. Usually we set this spatial frequency approximately equivalent to the size of 20 pixels of array detector.
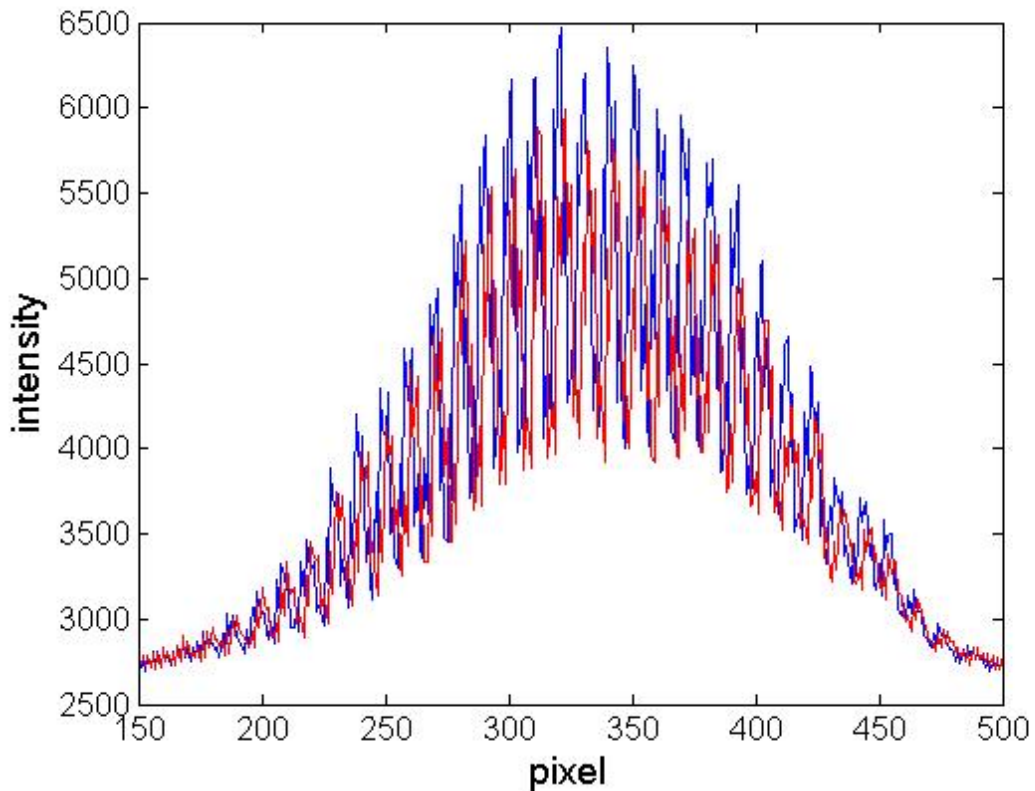

Figure 5.6. Two consecutive single-shot interference fringe (blue and red curve) of first order Stokes recorded on IR line scan camera

In the experiment, we took extra care to keep the intensity of the two pumps that are coupled into two HCPCF approximately equal, since the two fibers are not exactly same. For example, their lengths, degrees of bending (which affects the loss of the fibers), and their cleaving conditions are all slightly different. We balance these effects so that the two generated first-order Stokes fields should approximately have same properties.

In figure 5.6 we show the two "consecutive" single-shot interference fringes of first-order Stokes that we observed on the IR linescan camera. Here "consecutive" means two successive camera shots (at about 100 Hz), instead of the laser shots (at 5 kHz). Since the intensity of each Stokes field, like we show in previous section, is greatly fluctuating from one shot to another, the visibility of the fringes is also fluctuating. The figure shows a typical good fringe with an estimated visibility of 0.7. This high visibility reveals that the first-order Stokes field is highly self-coherent, or in other words, the Stokes field is temporal transform limited pulses, which is consistent with our conclusion in the previous section. Another feature that we observed is that the fringes are randomly moving from one shot to another. This movement is not due to the instability of the interferometer, but is a direct result of the quantum-generated random phase of the first-order Stokes field. From Equation 4-1, if we re-write the electric field of generated Stokes as:

$$E^{(j)}(x,t) = \left| E_n^{(j)} \right| e^{i\phi_n^j} e^{i\omega_n t - i k_n^j z} + c.c \, , \qquad (5\text{-}2)$$

where j (= A or B) indicates the fiber number, and n is -1 for the Stokes line, then the spatial oscillation of the interference fringe is directly related to the difference of temporal phases of two Stokes fields by:

$$I_{osc} \sim \cos(\Delta kx + \Delta\phi_{-1}).\qquad\qquad(5\text{-}3)$$

The movement of the interference fringes from one shot to another can come from two factors, that is, the wave vector difference Δk and the phase difference $\Delta\phi_{-1}$. The parameter Δk is directly related to the stability of the two-fiber interferometer, and we verify that this Δk is not changing from one shot to another because the interference fringes from the two Raman pumps are very stable. In this sense, we determine that the movement of the interference fringes indicates the temporal phase of the generated Stokes field is random from shot to shot. If we set a reference (or zero) phase point in our obtained interference fringe, we can get the phase value $\Delta\phi_{-1}$ for each shot. The detail of how to retrieve this phase will be discussed in the next section.

We also observed interference fringes with high visibility for anti-Stokes vibrational lines, including the first, second and third order. These anti-Stokes fields are in visible wavelength region, and we use a visible CCD camera (Thorlab LC-1USB) to observe the fringes.

Mutual coherence between first-order sidebands

In our research long-range goals, we are aiming to synthesize atto-second pulse trains by using the generated Raman optical frequency comb. In Chapters II and III, we used theoretical calculations to predict that ideally the phases of all comb lines are spontaneously correlated in a deterministic way within one single pump shot. In order to emphasize this, we repeat the predicted result as expressed in the following equation:

$$\phi_n = \phi_0 + n\,\phi_{rand}\,, \tag{5-4}$$

where ϕ_0 is the pump's phase, ϕ_{rand} is the random phase arising from the spontaneous initiation, and n is the order of Raman lines. For first-order sidebands, a more rigorous relation derived from quantum theory, which we call anti-correlation, is:

$$\phi_{-1} + \phi_{+1} = \text{ constant}\,. \tag{5-5}$$

We would like to test the validity of this phase anti-correlation prediction in our experiment. The experiment setup is same as in previous section. The one output from the second beam-splitter (BS-B in Figure 5.5) is filtered by an optical band-pass filter centered at 1200 nm, and then detected by an IR line-scan camera. The other output of that beam-splitter is filtered by the same kind of filter, centered at 600 nm, and detected by a visible line-scan camera. We simultaneously recorded these two fringes on the computer.

In Figure 5.7 we show the enlarged details of the typical two "consecutive" fringes detected by an IR camera and a visible camera. In this figure, the blue curves in both graphs are one shot, and the red curves are the next camera shot. It's easy to see that the red curve for the Stokes field moved to the blue curve's right. At the same time, the red curve for the anti-Stokes field moved to the blue curve's left but by the nearly same amount.

In order to show the relation in Equation 5-5, we recorded hundreds of simultaneous interference fringes on two cameras. For each fringe, we performed a sinusoidal fit to extract the amplitude and phase of the fringe in a carefully selected pixel window. An example is shown in Figure 5.8. This window usually contains two spatial oscillations around the peak area of the fringes, and the left-most pixel in the window defines the zero-point phase. The value of the extracted phase of each fringe from the fit is relative to this common zero-point. In the example, the phase of the Stokes fringe is -1.52, if the zero phase point is set at pixel #300.
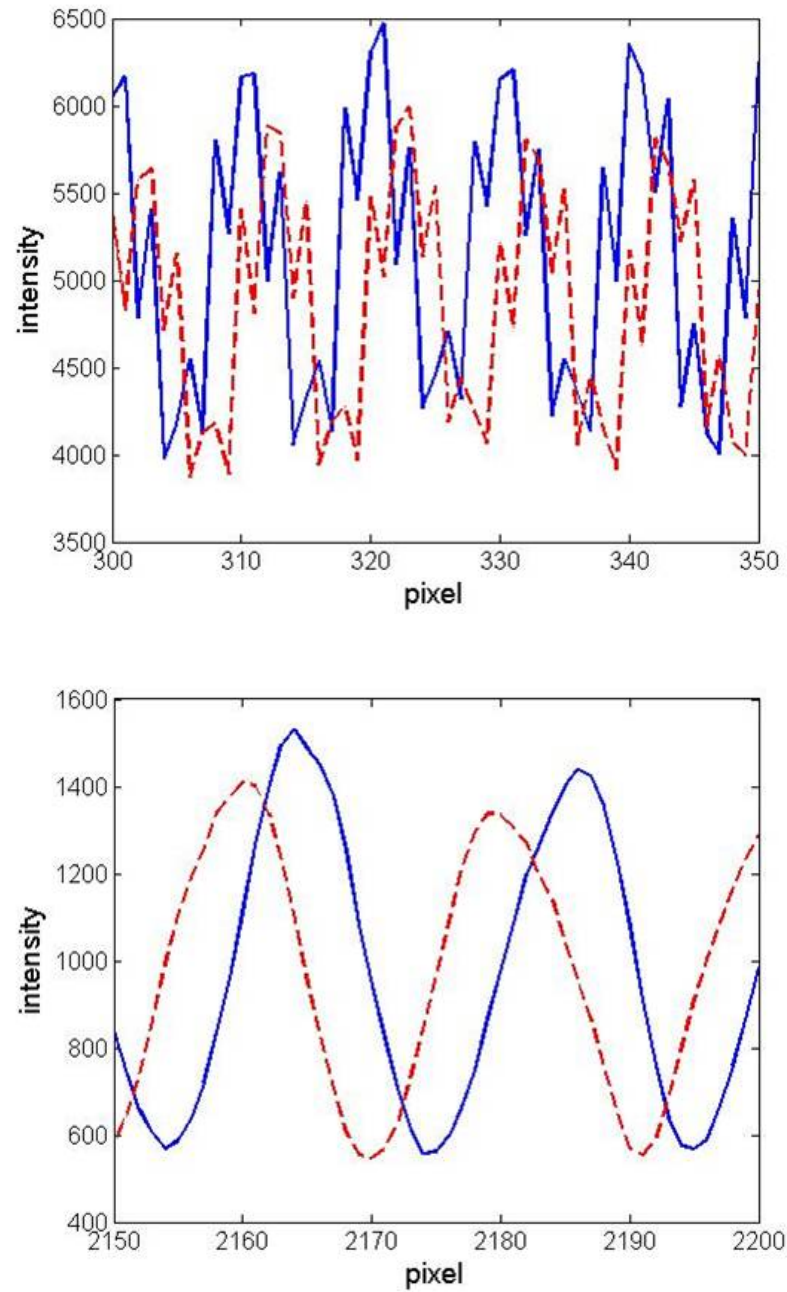
Figure 5.7. Two consecutive Stokes (above) and anti-Stokes (below) interference fringes recorded on the IR and visible linescan camera, respectively. These two cameras are configured to simultaneously measure single laser shot interference fringes. The Stokes fringes here are the enlarged part of Figure 5.6
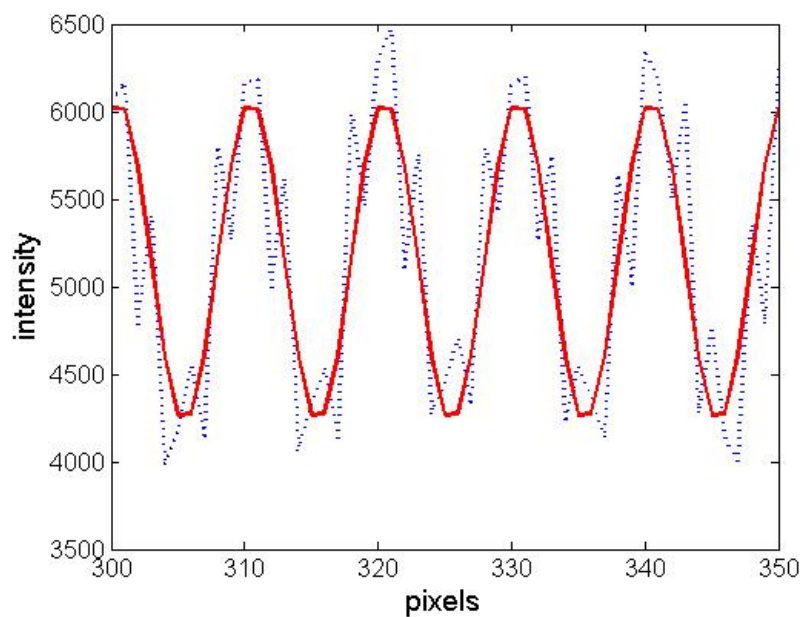
Figure 5.8. Example of extracting phase from Stokes interference
fringe (blue dotted) by performing sinusoidal fit (red solid)

It is then easy to quantify the fringe movement by the phase difference between two successive camera-recorded fringes. Remember the camera is operating at a much lower frame rate than the laser pulse repetition rate, and in this sense, the consecutive fringes are not the same as consecutive laser shots. Typically, the time delay between two consecutive fringes is about 30 ms. Mathematically, the phase extracted from one combined fringe containing both first-order Stokes and anti-Stokes that are simultaneously taken by two cameras can be written as:

$$\phi_{-1}^{(1)} = \phi_{-1}^{(A)} - \phi_{-1}^{(B)} = \delta\phi_{0}^{(1)} + \delta\phi_{-1}^{(1)}$$

$$\phi_{+1}^{(1)} = \phi_{+1}^{(A)} - \phi_{+1}^{(B)} = \delta\phi_{0}^{(1)} + \delta\phi_{+1}^{(1)} \tag{5-6}$$

where the superscript A and B on the right side of the equation counts the fiber number, and the number superscript of the left hand side is the fringe number. The symbol δ denotes the phase difference between the two fibers. For two consecutive camera-recorded fringes, the phase differences, or the movement of the Stokes and anti-Stokes fringes, are:

$$\Delta\phi_{-1} = \phi_{-1}^{(2)} - \phi_{-1}^{(1)}, \ \Delta\phi_{+1} = \phi_{+1}^{(2)} - \phi_{+1}^{(1)}. \tag{5-7}$$

According to our theoretical predictions, the phases of first-order Stokes and anti-Stokes are anti-correlated in one pump pulse, that is, $\delta\phi_{-1}^{(n)} + \delta\phi_{+1}^{(n)} = \text{constant}$. In this sense, the summation of the two-phase differences between consecutive camera-recorded fringes from two fibers should be zero:

$$\Delta\phi_{-1} + \Delta\phi_{+1} = \phi_{-1}^{(2)} - \phi_{-1}^{(1)} + (\phi_{+1}^{(2)} - \phi_{+1}^{(1)}) = \delta\phi_{-1}^{(2)} + \delta\phi_{+1}^{(2)} - (\delta\phi_{-1}^{(1)} + \delta\phi_{+1}^{(1)}) = 0 \tag{5-8}$$

In the experiment, the probability distribution of $\Delta\phi_{-1} + \Delta\phi_{+1}$ is obtained by analyzing over 300 experimentally recorded data (simultaneously recorded Stokes and anti-Stokes fringes), and is plotted in Figure 5.9. Its narrow peak around zero clearly shows the predicted phase anti-correlation between first-order Stokes and anti-Stokes. Using this

probability distribution, we calculate the quantity $\left\langle e^{i(\Delta\phi_{-1}+\Delta\phi_{+1})} \right\rangle$, which quantifies the

degree of phase anti-correlation:

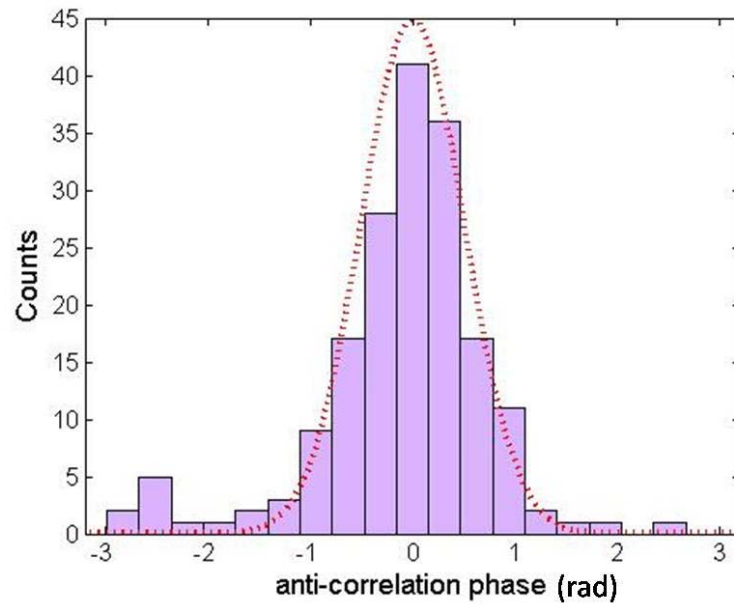$$\left\langle e^{i(\Delta\phi_{-1}+\Delta\phi_{+1})} \right\rangle \approx 0.8 \qquad (5\text{-}9)$$

Figure 5.9. Histogram plot showing the probability distribution of
the anti-correlation phase ($\Delta\phi_{-1} + \Delta\phi_{+1}$).

Our theoretical prediction for this quantity based on quantum Raman theory (see Chapter III, Section 1) is nearly one. This discrepancy between experiment results and theoretical prediction indicates the Raman comb process is more complicated than the first-order rigorous theory accounts for. In this sense, more sidebands need to be considered in the future development of the theory.

As we mentioned previously, this phase anti-correlation between Stokes and anti-Stokes fields is spontaneously generated. For the individual comb line, its phase is totally random. In Figure 5.10 I plot the histograms of the Stokes and anti-Stokes phases from the experimental data that is used to plot Figure 5.9. It's clear that both phases are random from one shot to another.
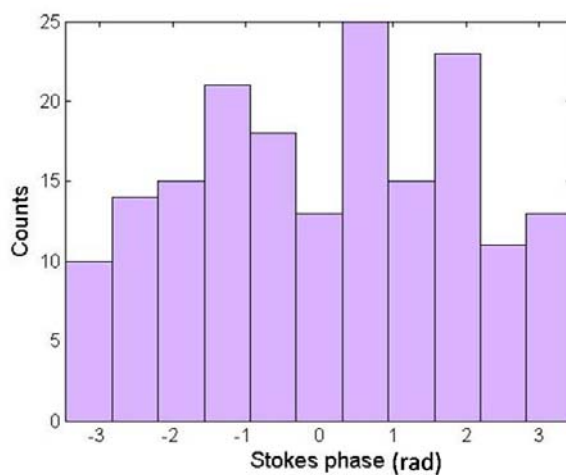
(*a*)
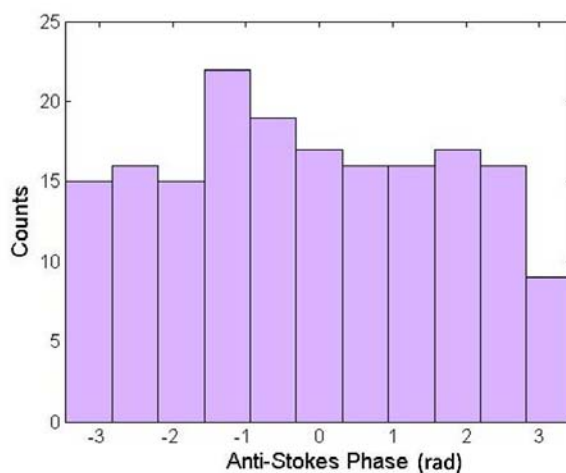
(*b*)

Figure 5.10. Random phases of Stokes (*a*) and anti-Stokes fields (*b*)

Synchronize two cameras

In the previous section, we showed how we verified the phase anti-correlation between first-order Stokes and anti-Stokes fields. The essential idea is to observe the interference fringes of these two fields that are generated from two independent hydrogen-filled HCPCFs *simultaneously* on two cameras. Here, this simultaneous measurement ensures that the two cameras capture the Raman fields generated by the *same* single-pump pulse. Otherwise, the measurement of the probability distribution of $\Delta\phi_{-1} + \Delta\phi_{+1}$ would not show any narrow peak, unless there is any phase correlation between Stokes or anti-Stokes fields that are generated by two pump pulses that are at least a few milliseconds apart. However, the molecular coherence usually fast dissipates in nanosecond scale, and therefore, the second pump pulse will not see any footprint that the first pump left in the molecules, and the fields it generated should have random phases compared to the phases of fields generated by the first pump.

In this section, I will show that in the experiment we ensured the two cameras were operating simultaneously (or synchronized), and the experiment result of measuring the probability distribution of $\Delta\phi_{-1} + \Delta\phi_{+1}$ if the two pumps are *not* synchronized.

In principle, although the two cameras we use are manufactured by different companies, both cameras are operating similarly. Their operation principle can be summarized as following: First, they will receive an 'open connection' command from

the computer. Under this command, the camera will first clear the memory of old data in its physical memory part, and then wait for a 'start measurement' command. Once it receives one, the camera will then wait for a trigger signal, which usually is a TTL from low to high pulse. After it's triggered, the camera will start 'integration' for a period of time set in its operating mode parameters, which means all the photons registered during this specified time period will be converted into electron currents.

However, since the IR and visible cameras are made from different companies, they are slightly different in their response times. This response time is defined as the time delay between receiving the computer command for 'start' and actually starting to integrate. If the response times of both cameras are shorter than the pulse repetition rate, which is 200 ms, then both cameras will be active for the same pump pulse. Unfortunately, our cameras are not fast enough in this time scale. Also, the response time difference is longer than 200 ms, which means the two cameras will naturally operate asynchronously.

To synchronize two cameras, the trick is to use an external trigger signal in a slow repetition rate. Normally, this external trigger is generated from the photo-detector that detects the light signal picked off from the pump pulse train, which is at 5 KHz. However, we can bring it down by the frequency divider, and this will slow the 'effective' pulse repetition rate that the two cameras are operating at. Once the response time difference between two cameras is shorter than this effective rate, the two cameras will be activated for same pump pulse; in other words, they'll be synchronized. The negative side effect is the slow detection rate (or frame rate). Usually we operate the two cameras synchronized

at about 30 frames per second, lower than the typical 100 frames per second that we used in the previous experiment that uses only one individual camera to measure the Stokes energy statistics.

We test the synchronization of two cameras in the following way: A chopper wheel is placed in the alignment before the pump light is split by first beam-splitter (BS-A in Figure 5.5). This chopper wheel is operating at 1.7 KHz to modulate the pump's intensity. The two cameras are both configured in slow trigger mode and 'simultaneously' detect the pump signal transmitted from the HCPCF fiber. In Figure 5.11 we show the signal recorded from two cameras versus the frame (or detection) number. The vertical axis is the peak amplitude of the pump signal recorded on each camera in one 'simultaneous' detection numbered by the horizontal axis. We can see that these peak amplitudes from the two cameras are oscillating together due to the amplitude modulation from the chopper wheel, which directly shows the two cameras are correctly synchronized in our experiment.
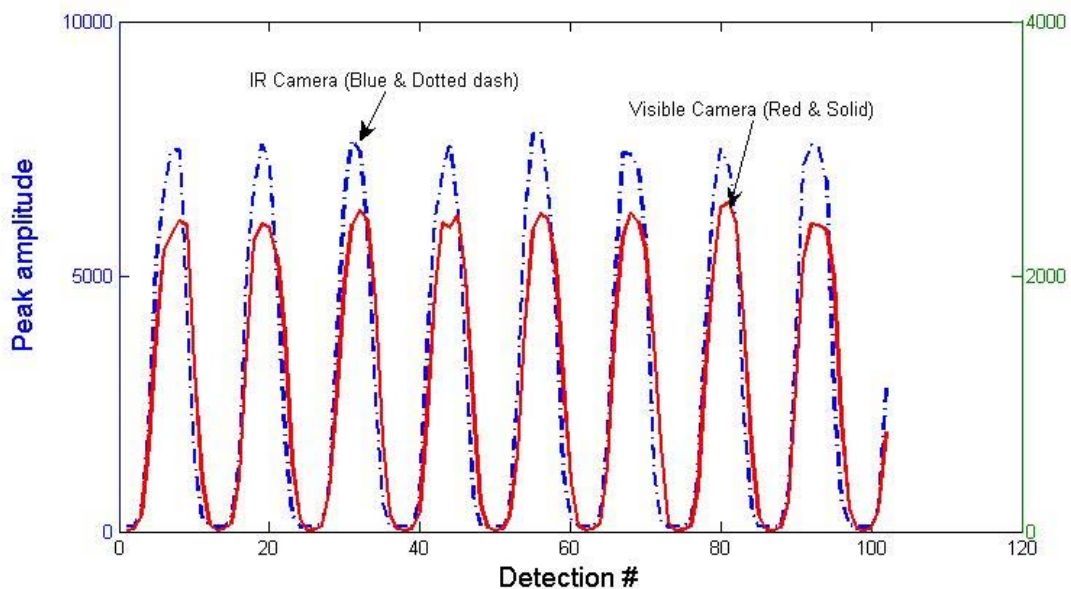
Figure 5.11. Simultaneous measurement of pump signals on two
cameras. The pump's amplitude is modulated by a chopper wheel

I also performed the measurement of the probability distribution of $\Delta\phi_{-1} + \Delta\phi_{+1}$ with
the same procedures described in the previous section, but with 'asynchronous' cameras.
The result is plotted in Figure 5.12. We see a random phase distribution, which exactly
shows no phase correlation between the Stokes field generated by the first pump pulse
and the anti-Stokes field generated by another pump pulse following the first one by a
few milliseconds. Or, in other words, no molecular seeding is present in our experiment
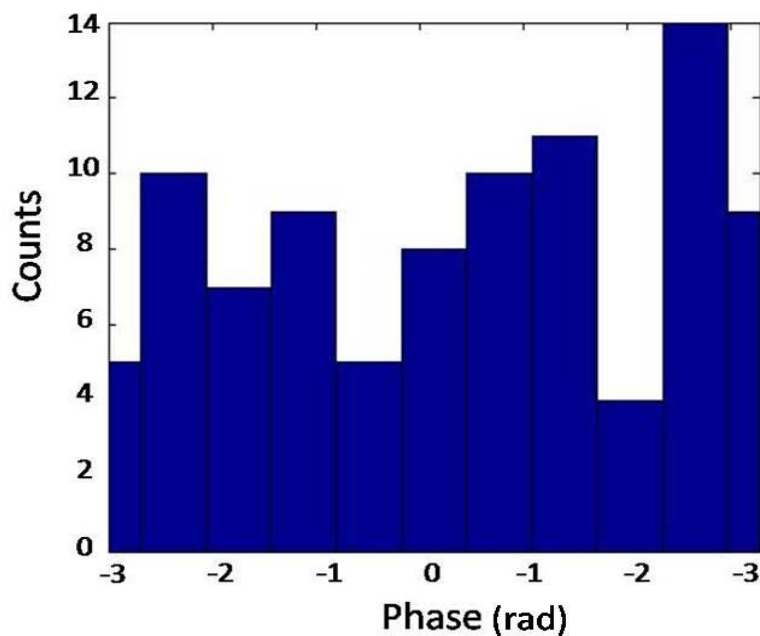with a 5 kHz pump repetition rate.

Figure 5.12. Histogram plot of the phase $\Delta\phi_{-1} + \Delta\phi_{+1}$ (radiance) with asynchronous pumps. No phase anti-correlation is observed under this condition.

Phase correlation between first-order Stokes and second-order anti-Stokes fields

In this section we would like to verify the phase correlation between first-order Stokes and second-order anti-Stokes, as predicted by our theory based on the modulator model (see Chapter III, section 2). We use a method similar to the one I described in measuring first-order pairs. Here the visible camera is measuring the interference fringes

of the second-order anti-Stokes field (wavelength at 488 nm) from two fibers. The two cameras are operated synchronously.

According to Equation 5-4, the phase correlation between first-order Stokes and second-order anti-Stokes predicts:

$$2 \times \phi_{-1} + \phi_{+2} = \text{constant} . \tag{4-10}$$

In order to verify the above correlation, we measure the probability distribution of the quantity $2 \times \Delta\phi_{-1} + \Delta\phi_{2}$, where symbol Δ again means the phase difference between two consecutive camera shots. The experimental result is shown in Figure 5.13.

The peak around zero shows that there exists the predicted phase correlation between first-order Stokes and second-order anti-Stokes. However, this correlation is not as strong as the one observed for first-order sideband pair, since the peak is wider, or, quantitatively,

$$\left\langle e^{i(2 \times \Delta\phi_{-1} + \Delta\phi_{+2})} \right\rangle \approx 0.5 ,$$

which is smaller than the average value of 0.8 that we obtain for first-order sideband pair.
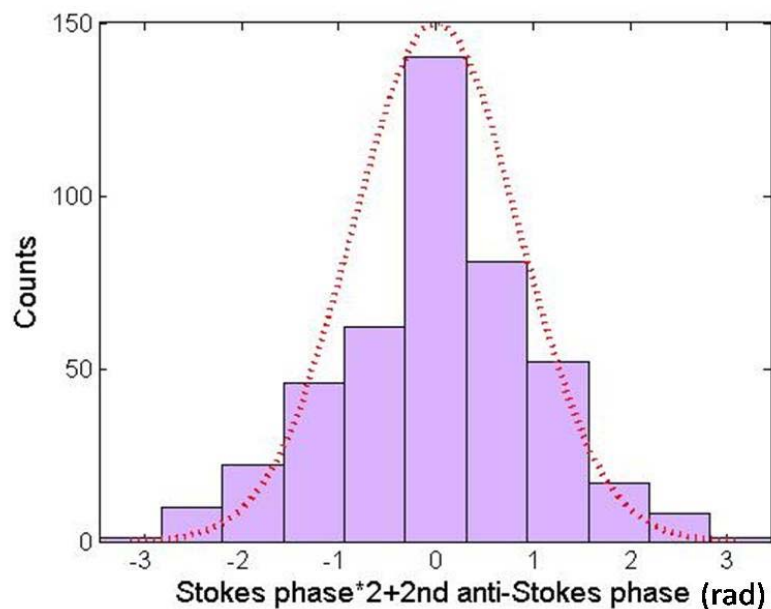
Figure 5.13. Histogram showing the probability distribution of quantity $2 \times \Delta\phi_{-1} + \Delta\phi_2$.

The reasons why the correlation is degraded for higher-order modes is not well understood. We speculate that dispersion between second-order Stokes and first-order Stokes may be an important factor.

Two-color experiment

The key idea in our derivation of the phase correlation involving high-order sidebands in Chapter III is the so-called phase modulation. This idea assumes that the

molecular coherence created by a pump pulse interacting with hydrogen molecules when generating the first-order sidebands is acting like a phase modulator back on the fields. Every time the light is scattered off this molecular coherence, the generated new light will obtain one phase shift. In this sense, the phase of n-th order sideband is given by Equation 5-4, that is, $\phi_n = \phi_0 + n\,\phi_{rand}$.

In this section, we would like to test this phase modulation idea by using two laser pulses with different colors. One is the pump pulse with 200 ps at 800 nm that we used in the previous section, and the other one is the frequency-doubled pump pulse, which is at 400 nm. In short, I denote the pump pulse at 800 nm as the red pump, and the 400 nm pulse as the blue pump. In our experiment, we use the high-power red pump to generate its first-order vibrational Raman sidebands as well as the hydrogen molecular coherence. At the same time, the blue pump is overlapped with the Red pump spatially and temporally, but is kept at a low intensity. In this way, the blue pump is very close in frequency to the third-order anti-Stokes of the red pump. If the blue pump is scattered by the molecular coherence created by red pump, then its generated Stokes will have the same phase as the red pump's Stokes, according to the Raman phase modulator model. The energy diagram of this two-color experiment is shown in Figure 5.14.
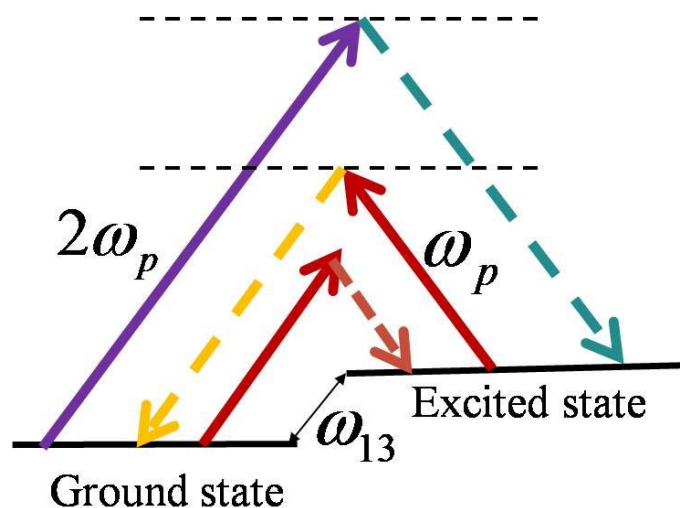
Figure 5.14. Energy diagram of the two-color experiment

The blue pump is generated by a second harmonic generation of the red pump on a BBO crystal. We choose to use a BBO crystal because it is a uniaxial crystal with a high damage threshold. We carefully designed this BBO crystal optimized for 200 ps pulses. The cutting of the BBO crystal is set at an angle θ_c (the angle between the crystal's optical axis and the normal to the crystal surface) so that we can use the type I second harmonic generation, where two red photons at 800 nm with polarization at the crystal's ordinary refractive index axis are annihilated and one blue photon at 400 nm with polarization at the crystal's extraordinary refractive index axis is produced. The critical angle for the phase mismatching condition at this situation is about 24 degrees. This angle can be achieved by putting the crystal on a rotational stage.

The experiment setup for generation of the blue pump and then coupling both red and blue pump into HCPCF is shown in Figure 5.15. The output from the Regen cavity is split into two parts by using a half-wave plate following a polarized beamsplitter. One output of the beamsplitter is used to generate the blue pump. The other output will be used as the red pump. In order to generate the blue pump, we use a 75 mm lens to tightly focus the red light onto the BBO crystal. The generated blue pump has a wide rectangular spatial shape in the far field, due to the walk-off effect (energy flow is different than the propagation direction) of the BBO crystal. We use a combination of 75 mm convex lens and a 150 mm cylindrical lens to collimate the blue pump. The distance between these two lenses is about 225 mm. The residue of the red light after the crystal is just diverging and dissipating away. We use a dichroic mirror (Thorlabs DHLP 570) to combine the blue and red pump. In order to adjust their temporal delays, we place a translational stage in the red pump's alignment. The conversion efficiency of red to blue on the BBO crystal is estimated to be about 30%. The maximum average power of the blue pump is estimated to be 40 mW, limited by the maximum red power allowed to put on the BBO crystal without damaging it.
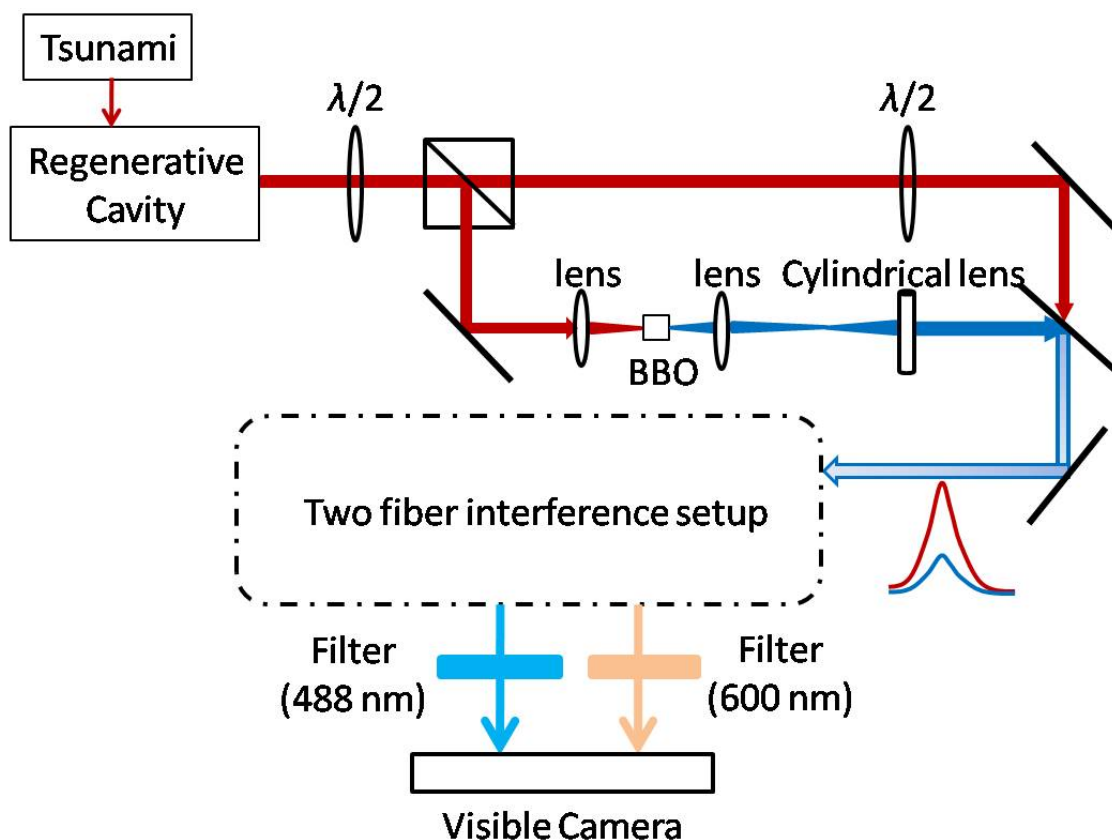
Figure 5.15. Experimental setup for two-color experiment

The combined blue and red pumps are then coupled into a two-fiber setup, similar to the one shown in Figure 5.11. Both red and blue pumps are coupled into each fiber. The difficulty, however, is how to diminish the chromatic aberration in the focusing lenses, since the two pumps are widely separate in wavelength. Thanks to the large numerical aperture of the HCPCF (NA>0.03), we don't need to use a tightly focused coupling lens, such as a microscopic objective lens. In Gaussian optics theory, if the laser beams are focused by a lens with a long focal length, then they will have longer Raleigh ranges at their focal spots. If the chromatic aberration focal shift of the blue and red pumps induced

by the coupling lens is smaller than their Raleigh range, then it's possible to couple both beams into HCPCF with high efficiency. In the experiment, we use a 50 mm achromatic doublet lens with broadband visible to near-infrared coating. Note that this lens is different than the one (focal length is 35mm) optimized for a single-pump situation. In this way we slightly compromise the coupling efficiency of the red pump to significantly increase the blue coupling efficiency. We estimate that the coupling efficiency of the red and blue pump is about 15% and 20%, respectively.

In Figure 5.16, we also show the Raman spectrum generated with both pumps coupled into one HCPCF. The blue pump is controlled at low intensity, so that it does not generate any sidebands by itself. However, with the red pump interacting strongly with hydrogen molecules, the blue pump is scattered by the molecules that are coherently excited by the red pump and its first-order Stokes is present in the spectrum. It should be noted that, in Figure 5.16, the red pump looks dimmer than the blue pump although the red pump is 20 times more intense than the blue pump. This is because the blue color is more sensitive to the digital camera. In Figure 5.17, we show the picture of "colorful" fibers when the two-color experiment is taking place.
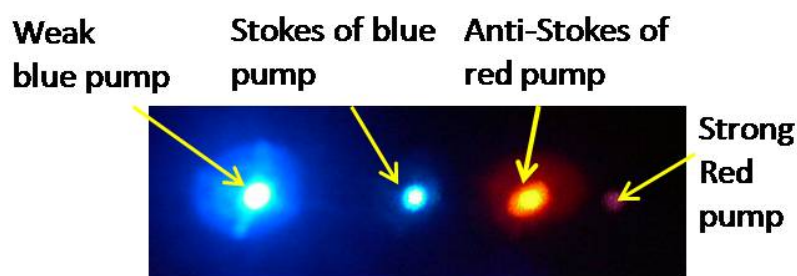

Figure 5.16. Raman spectrum generated in two-color experiment
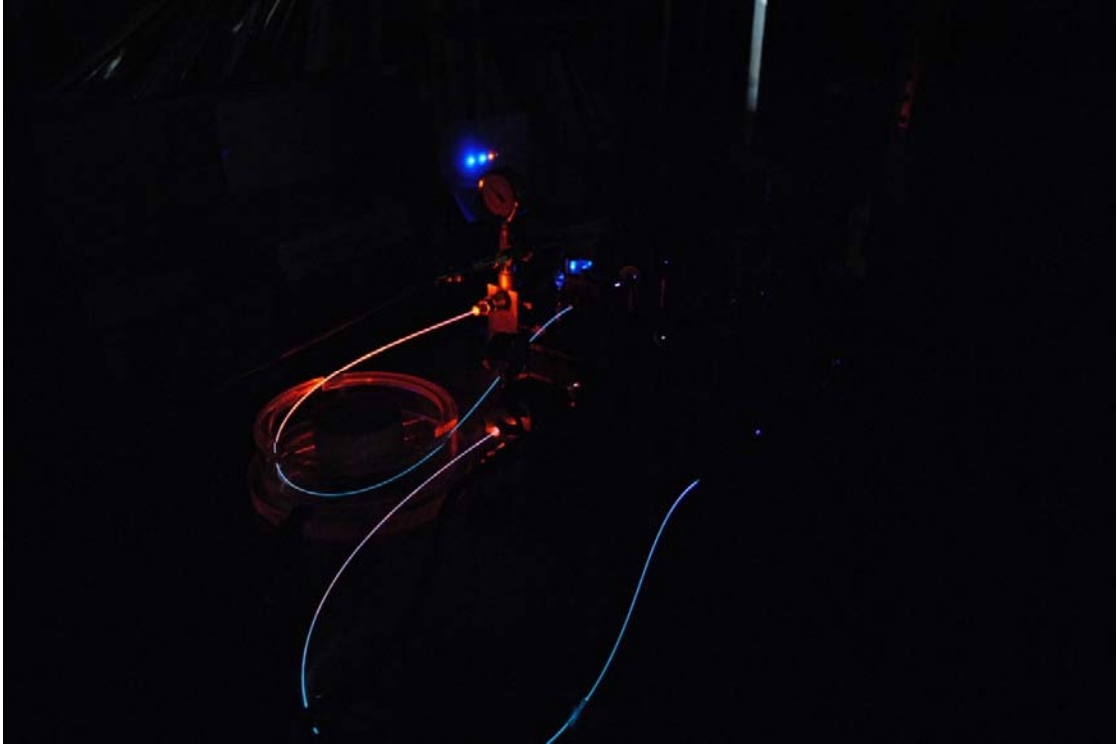
Figure 5.17. Picture of fiber when two-color experiment is taking place

We also perform the simultaneous phase measurement of first-order Stokes of the blue pump (at 485 nm) and first-order anti-Stokes of the red pump (at 602 nm). From their single-shot interference fringes recorded on one visible linescan camera (Thorlabs), which automatically ensures the simultaneous measurement, we can obtain the probability distribution of the quantity $\Delta\phi_{stokes}^{blue} + \Delta\phi_{anti-stokes}^{red}$. The typical individual interference fringes (single shots) are shown in Figure 5.18.
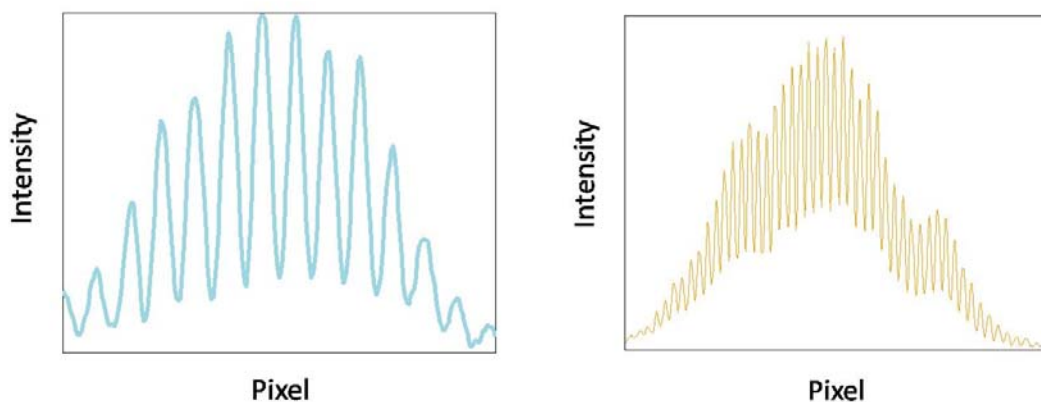
Figure 5.18. Single shot Interference fringes of blue pump's Stokes and red pump's anti-Stokes

If the modulator model is valid, then the phases of these two fields, first-order Stokes of the blue pump and first-order anti-Stokes of the red pump, will be also anti-correlated. In Figure 5.19, we plot the measured probability distribution over 300 shots. Its narrow peak around zero again verifies our speculation of the phase anti-correlation. This experiment result also shows that the molecular coherence generated by the red pump has a well-defined temporal mode with random shot-to-shot phases. This coherence is related to the quantum memory and entanglement that is described in Chapter II. It can be used to modulate coherently any light at the frequency equal to the molecular vibrational frequency, which in our case is 125 THz.
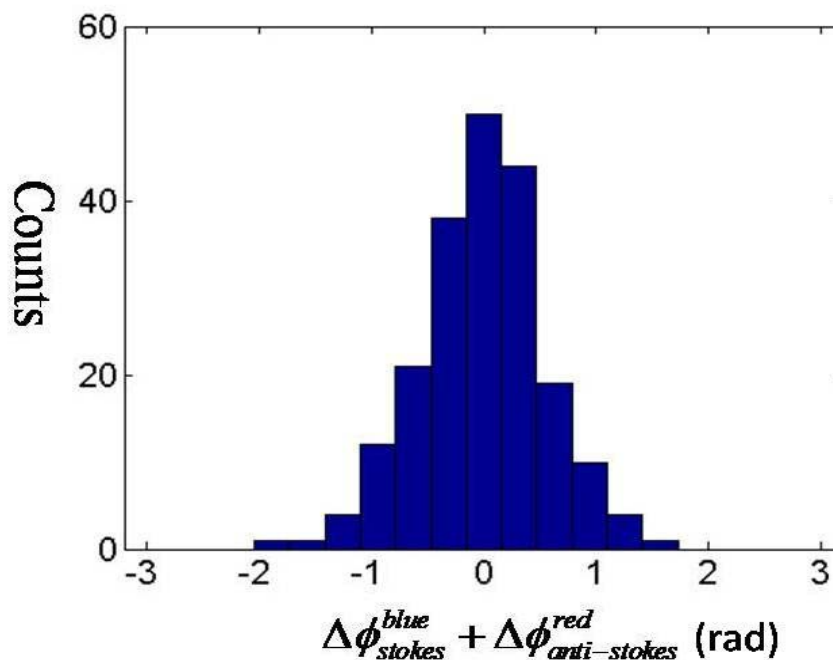
Figure 5.19. Experiment result of the probability distribution (histogram) of the quantity $\Delta\phi_{stokes}^{blue} + \Delta\phi_{anti-stokes}^{red}$.

Phase locking the Raman comb

Our experiment results using single pump to generate the optical Raman frequency comb clearly verify two predictions of our theoretical work: the random phases from shot to shot and the phase correlation among comb lines in one shot. In order to overcome this phase randomness, people add an auxiliary laser beam with the pump beam to coherently drive the molecular vibration, and thus the generated comb has a locked phase [65]. Often, this auxiliary laser beam is spectrally overlapped with the first-order Stokes line. One

way to understand the mechanism of this phase locking is to treat the auxiliary beam as a coherent seed beam. The photons in the seed beam stimulate the Raman scattering process, and any Stokes photons that are scattered from pump photons will be coherent with the seed beam. In the same time, the molecular coherence is also created in a well-defined phase, and according to Equation (5-4), this phase equals: $\phi_{mol} = \phi_0 - \phi_{-1} = \Delta\phi$, where $\Delta\phi$ is the phase difference between the pump beam and the auxiliary beam. If this phase is fixed from pulse to pulse, then the phases of the Raman comb are locked (see Figure 5.20 (a)).

The disadvantage of using an auxiliary beam is obvious, since one has to use another laser beam which is exactly ω_{13} away from the pump laser in frequency and is phase locked to the other laser.

We are currently trying to extend our two-color experiment, where the frequency-doubled pump beam (the blue beam) is acting as an auxiliary beam to phase lock the comb. The frequency of the red pump is tunable for the Ti:Sapphire laser between 350 THz and 400 THz. If the red pump is tuned to around 375 THz, then it will be resonant with the third harmonic of Raman vibrational transition (125 THz) in hydrogen molecules. In other words, the blue pump at 750 THz will be resonant with the third-order anti-Stokes of the red pump. Ideally, the phases of all comb lines generated by red pump only are correlated by $\phi_n = \phi_{red} + n\phi_{rand}$. But the existence of blue pump will force the third-order anti-Stokes to have the phase $\phi_{+3} = \phi_{blue}$. Therefore, when these two pumps simultaneously interact with the hydrogen molecule, the phase of the Raman comb will be locked to $\phi_{rand} \to \Delta\phi / 3 = (\phi_{blue} - \phi_{red}) / 3$. This result is also self-consistent if one treats

the blue pump as the main pump to create molecular vibrations and Raman combs, while the red pump is resonant with the third order Stokes line. The process is illustrated in Figure 5.20 (b).
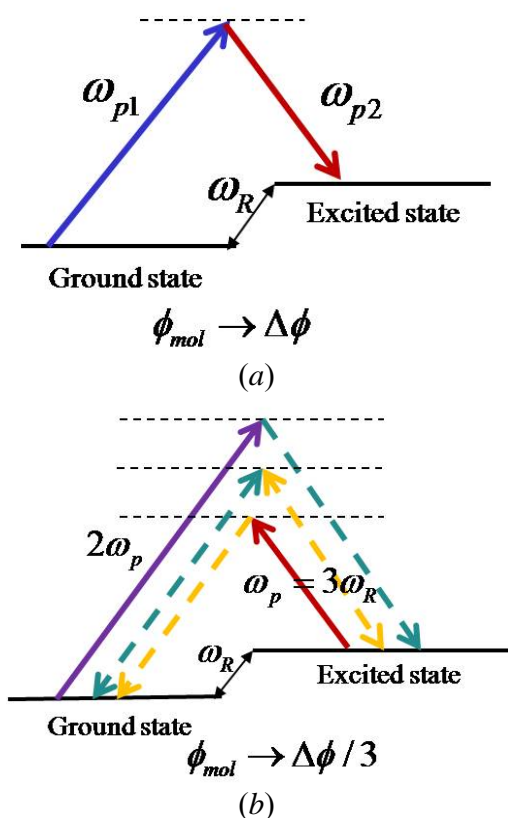

Figure 5.20. Phase locking the Raman comb. (a) auxiliary beam overlapped with first-order Stokes. (b) our proposed scheme, where blue pump will spectrally overlap with third-order anti-Stokes of red pump.

We did the following experiment to determine the exact resonant frequency, since 375 THz (800 nm in wavelength) is only a rough estimation according to the known

hydrogen Raman transition frequency. We use a strong red beam (no blue beam) to generate the Raman comb in one fiber filled with 100 PSI hydrogen in its loading cell, and filter out the third-order anti-Stokes line at around 400 nm. In the other fiber, no hydrogen is filled and only a blue pump, which is directly generated from the BBO crystal, is transmitted through the fiber. We spatially overlap this blue pump and the third-order anti-Stokes generated by the red pump in the other fiber, and record the interference fringes on one visible line-scan camera while tuning the red pump laser around 800 nm.

Since the amplitude and phase of the third-order anti-Stokes is fluctuating, the visibility of the recorded interference fringes at one certain laser wavelength is also changing. We analyze each fringe by using the sinusoidal fit that is described in the previous section (Figure 5.8), and extract the amplitude of the fit. For one wavelength point, we obtain the average of the interference amplitudes of 100 fringes, and plot this average amplitude as a function of the wavelength. The result is shown in Figure 5.21.

We can see that the resonant wavelength is clearly shown at 802.2150 nm. This, in turn, can be used to deduce the Raman vibrational frequency shift of hydrogen molecule. We found it to be 4155.16 cm^{-1}, very close to the one used as a standard value (4155.23 cm^{-1}) [37]. After we found this resonant wavelength, we coupled both the blue and red pumps into two fibers. Since the proposed phase locking uses a third-order effect, it requires the blue pump's power as high as the red pump's. The experiment setup (Figure 5.15) in the "two-color experiment" section is no longer suitable, because the blue pump's power is limited by how much Regen output is split onto BBO crystal. We are

currently modifying the setup, basically to allow us to use full Regen output onto the BBO crystal to generate the blue pump. In this way, we believe the blue pump will be strong enough so that we can observe the phase-locked comb.
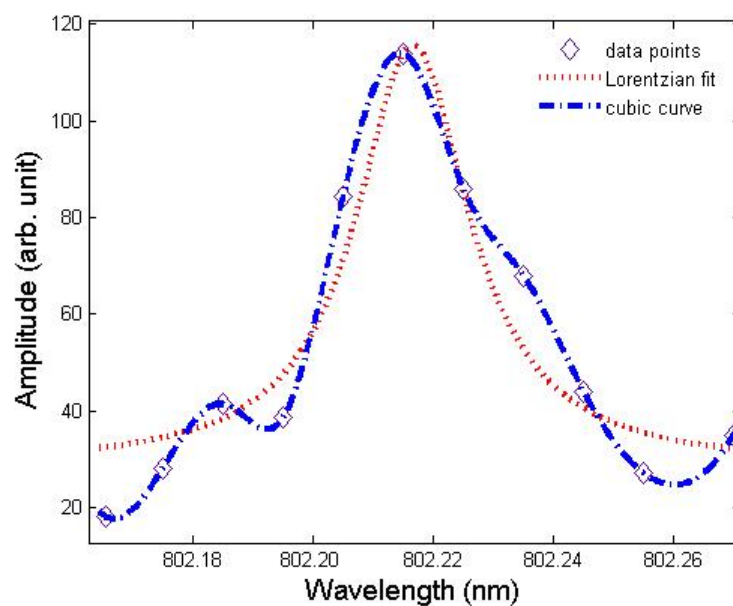

Figure 5.21. Average amplitude of interference fringes as a function of wavelength tuning

CHAPTER VI

CONCLUSIONS

With the help of hollow-core photonic crystal fiber, Raman optical frequency comb generation now looks achievable with relatively low-power table-top setups. In our experiment, we have demonstrated that, with one stage of amplification, a Ti:Sapphire laser is capable to generate more than 20 rotational or 4 vibrational comb lines at the energy level of 10 micro-joules per pulse. The total frequency span of the optical Raman comb is multiple octaves, where the highest frequency is a factor of 2 or larger than the lowest frequency.

In comparison, conventional Raman comb experiments carried out using meter-long high-pressure hydrogen tubes requires Q-switched high-power lasers with fixed output wavelength. he frequency tuning capability of Ti:Sapphire laser will then have another comparative advantage, that is, it will allow the generated Raman comb to cover all frequencies from blue to infrared region. To reach the deep blue region (< 350 nm), one can first frequency double the Ti:Sapphire laser output, as described in our two-color experiment, and then generate the Raman frequency comb from the frequency-doubled light.

An individual Raman comb line can be used as a reliable laser source, if the Raman comb is phase stabilized by coherent seeding. The portability and easy construction of the gas-filled HCPCF will make the Raman comb a very useful light source for those applications requiring multiple lasers.

Our goal of using the Raman optical frequency comb is to synthesize atto-second pulses, which are short enough for illuminating an electron's motion. Since we only use a single pump pulse, all Stokes and anti-Stokes lines are generated from quantum vacuum fluctuations. By simply making an analogy between first-order Raman generation and the four-wave mixing (FWM) process, we speculate that there are phase correlations in the generated first-order Stokes and anti-Stokes fields. However, in Raman scattering, the molecular vibration needs to take into consideration, which is neglected in standard FWM theory. Our speculation is confirmed by first using quantum theory to model the Raman process, and then calculating the value of an anti-correlation coefficient under the initial conditions directly reflecting the quantum initiation of the comb lines. This anti-correlation coefficient not only predicts that the energy of first-order Stokes and anti-Stokes are fluctuating in the same manner, but their phases sum to a constant from shot to shot. This quantum initiated phase correlation has never been observed in experiment before, nor has anyone attempted to illustrate it. Our collaborators in University of Bath first observed this phase correlation [66], and later we confirmed it by using 200 pico-second Raman pump pulses generating H_2 vibrational comb lines [67].

In our experiments, we set up an interferometer that contains two quantum initiated Raman optical frequency combs. These two Raman combs are regarded as identical,

since they are pumped by pump pulses with identical properties, the same HCPCF type and length are used, and the same hydrogen gas pressure is used. The outputs of the interferometer are interference fringes of pairs of comb lines having the same order, which were filtered from the two Raman combs. The high visibility of these interference fringes shows that the Raman combs are generated in near transform limited pulses. By recording the single-shot interference fringes of first-order Stokes and anti-Stokes simultaneously from the two outputs of the interferometer, and observing their movements from one pump shot to another, we illustrate the expected phase correlation between first-order sidebands. Using the same method, we can also show that phase correlation also exists for higher order sidebands. This phase correlation can be explained by a self-consistent Raman modulator model, where hydrogen molecules are excited by a pump pulse and act as a phase modulator to all comb lines.

The Raman modulator model is a simple and useful guideline for predicting the mechanism of Raman comb generation. We tested the idea of Raman modulator model by setting up a two color experiment. This experiment illustrates that the molecular vibration created in the quantum initiated Raman scattering process has a well defined (that is, constant throughout the pulse) phase, but that the value of this phase is random. This random phase determines the phase of generated Stokes and anti-Stokes fields. If any other light field is scattered by the molecular coherence, its scattered field will obtain this random phase shift, the same as if the light is being phase modulated by the molecular coherence.

This discovery of phase correlation in Raman comb lines leads us to develop a new method for phase locking the comb. According to our understanding from the Raman modulator model, phase locking the comb is equivalent to stabilizing the phase of molecular coherence. If the Raman pump is tuned to an integer multiple of the natural frequency (ω_{13}) of molecular vibration (or rotation), then its second harmonic and itself, whose frequency difference will also be multiple integer times ω_{13}, will force the molecules to vibrate in a well defined phase related to their phase difference. People have demonstrated this phase locking effect in hydrogen gas when the pump frequency equals ω_{13}, the hydrogen vibrational frequency, and we are currently carrying out an experiment where the pump frequency will be three times ω_{13}. This frequency happens to fall into the Ti:Sapphire region, around 800 nm in wavelength. If our experiment is successful, the phasing-locking scheme will be greatly simplified because when different Raman active medium is used, it will no longer be limited by the availability of lasers operating at Raman transition frequency.

APPENDIX A

DETAILED EXPRESSION FOR CALCULATING ANTI-

CORRELATION COEFFICIENT

Here we give the detailed expressions for the correlation coefficient C that is defined in equation (3-5), and for the intensity of the first-order Stokes and anti-Stokes fields, by using the solution of equation (3-2) and the initial conditions of equation (3-4). The Stokes intensity is:

$$
\begin{aligned}
I_s(L,\tau) &= \left\langle E_{-1}^{(-)}(L,\tau)E_{-1}^{(+)}(L,\tau) \right\rangle \\
&= \frac{\left|\alpha_{2,a}\right|^2}{AN}\left|E_0(\tau)\right|^2 \int_0^L dz' \left|G_{13}(z';\tau,0)\right|^2 + \frac{2\pi\hbar\omega_{+1}\left|\alpha_{2,s}\alpha_{1,a}\right|^2}{Ac}\left|E_0(\tau)\right|^2 \int_0^\tau d\tau' \left|E_0(\tau')\right|^2 \left|G_{12}(L;\tau,\tau')\right|^2
\end{aligned}
\tag{A1}
$$

The anti-Stokes intensity is:

$$
I_a(L,\tau) = \left\langle E_{+1}^{(-)}(L,\tau)E_{+1}^{(+)}(L,\tau) \right\rangle = \frac{2\pi\hbar\omega_{-1}\left|\alpha_{1,s}\alpha_{2,a}\right|^2}{Ac}\left|E_0(\tau)\right|^2 \int_0^\tau d\tau' \left|E_0(\tau')\right|^2 \left|G_{21}(L;\tau,\tau')\right|^2
\tag{A2}
$$

The product of Equation (A1) and (A2) gives the denominator of correlation coefficient C, and its numerator is:

$$
\left|\left\langle E_{-1}^{(-)}(L,\tau)E_{+1}^{(-)}(L,\tau) \right\rangle\right|^2 = \left|\frac{2\pi\hbar\omega_{+1}\left|\alpha_{1,s}\right|^2 \alpha_{2,s}\alpha_{2,a}^*}{Ac}\left|E_0(\tau)\right|^2 \int_0^\tau d\tau' \left|E_0(\tau')\right|^2 G_{11}(L;\tau,\tau')G_{12}^*(L;\tau,\tau')\right|^2
\tag{A3}
$$

Since the operators $E_{-1}^{(-)}(L,\tau)$ and $E_{+1}^{(-)}(L,\tau)$ commute, the numerator can also be expressed

by changing their order:

$$
\left| \left\langle E_{+1}^{(-)}(L,\tau) E_{-1}^{(-)}(L,\tau) \right\rangle \right|^2
$$

$$
= \left| -\frac{\alpha_{2,s}\alpha_{2,a}^*}{AN} \left| E_0(\tau) \right|^2 \int_0^L dz' G_{13}(z';\tau,0) G_{23}^*(z';\tau,0) \right.
$$

$$
\left. -\frac{2\pi\hbar\omega_{-1}\left|\alpha_{1,a}\right|^2 \alpha_{2,s}\alpha_{2,a}^*}{Ac} \left| E_0(\tau) \right|^2 \int_0^\tau d\tau' \left| E_0(\tau') \right|^2 G_{12}(L;\tau,\tau') G_{22}^*(L;\tau,\tau') \right|^2
$$

(A4)

We can then ensure the precision of our calculations by comparing the values of equation

(A3) and (A4).

APPENDIX B

PULSE MEASURING DEVICE

This is an independent project that I have worked in parallel with my main research topic in Raman optical frequency comb generation. Our goal of this project is to characterize the amplitude and envelope phase of mode-lock laser pulses whose duration is approximately 100 pico-seconds. These pulses cannot be measured by conventional pulse characterization devices, such as FROG [68], because their spectrum spreading is too small to be measured accurately.

First of all, we need to define what we mean by the envelope phase of an optical pulse. This phase is the temporal phase of the slowly-changing envelope of the electric field. Mathematically, the optical pulse can be written as:

$$E(t) = \left| E(t) \right| e^{i\phi(t)} e^{i\omega_0 t} .$$

where ω_0 is the optical frequency at about 400 THz, $\phi(t)$ is the phase that we want to measure, and $\left| E(t) \right|$ is the amplitude.
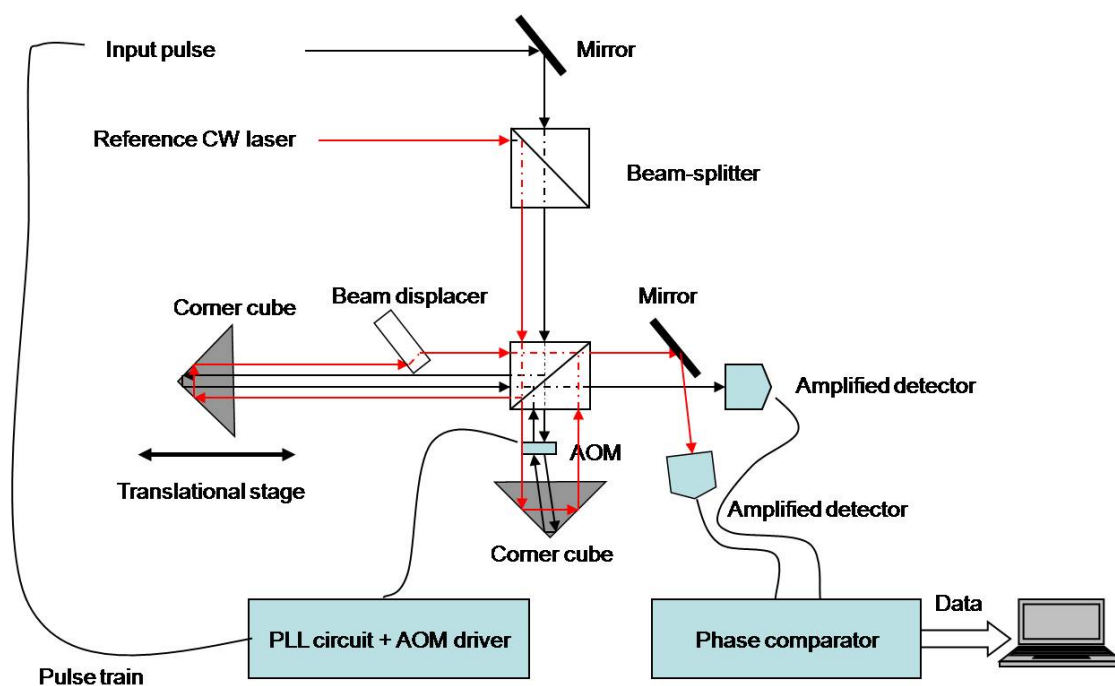
Figure B.1. Device setup

The scheme we use to characterize the electric field is shown in Figure B.1. The target optical pulse is indicated by black arrows. The setup is basically a Michelson interferometer, where the target pulse is split into two identical parts. One end mirror (corner cube) of the interferometer is put on a translational stage, so that an adjustable delay between two arms can be achieved. In the alignment of the other arm, an AOM is placed into the optical path of the target pulse. The pulse is first deflected by the AOM, and then retro-reflected back by a corner cube, hitting the AOM again. The 2nd deflection from AOM will be parallel to the incoming pulse. Therefore, by carefully aligning the positions of the two corner cubes, we can spatially overlap the two reflections from each

corner cube on the beamsplitter. The output of the interferometer is then detected by an amplified detector (Thorlabs PDA100A).

Double passing through the AOM is actually spectrally shearing [69] the optical pulse, which means the resultant pulse is identical to the original pulse except that it is frequency shifted by certain amount (Ω). In another hand, the Michelson interferometer output, usually called auto-correlation signal, is well known as the Fourier transform of the power spectrum of the pulse. We then can show that the signal on amplified detector is:

$$f(\delta) = \left[\int d\omega \left| E(\omega)E(\omega+\Omega) \right| e^{i\Delta\phi(\omega)} e^{i\omega\delta} \right] e^{i\omega_0\delta} + c.c., \qquad \text{(B-1)}$$

where $\delta = \Delta L / c$ is the delay between the two arms of the interferometer. It contains the information of interest, i.e., the slowly-varying phase term (in frequency domain):

$$\Delta\phi(\omega) = \phi(\omega) - \phi(\omega+\Omega) . \qquad \text{(B-2)}$$

It is our purpose of this experiment to retrieve this phase difference $\Delta\phi(\omega)$ from the detected signals (equation B-1) on the amplified detector, which can be measured as a function of the delay δ. A well established concatenation method then can be used to retrieve the spectral phase $\phi(\omega)$ [69].

In theory, if we can obtain the quantity shown in the bracket of equation B-1, that is,

$$I(\delta) \equiv \int d\omega \left| E(\omega)E(\omega+\Omega) \right| e^{i\Delta\phi(\omega)} e^{i\omega\delta} \equiv \left| I(\delta) \right| e^{i\varphi(\delta)}, \qquad \text{(B-3)}$$

then we will be able to obtain $\Delta\phi(\omega)$ after a simple Fourier transform of $I(\delta)$.

In doing so we need to demodulate the signal $f(\delta)$ from its fast oscillation of $e^{i\omega_0\delta}$. This prompted us to use an auxiliary beam that is output from a stabilized He-Ne laser, shown as the red curve in Figure B-1. This auxiliary beam passes through the same interferometer and is detected by another amplified detector, but is not deflected from the AOM. Also, in order to spatially overlap the auxiliary beam at the output of the interferometer, we place a beam displacer (thick optical parallel window) to introduce a lateral walk-off in one arm. Remember, we cannot adjust corner tubes at this time because they have already been set to ensure the spatial overlap of the target pulse (black curve in Figure B.1).

This auxiliary beam is acting as a reference, which is always needed to define a "phase". In experiment, we scan the translational stage from negative to positive delay with a constant speed v. The signals detected by both amplified detectors are sent into a phase comparator, which gives the phase difference between them. In theory, this phase difference is:

$$\Delta = (\frac{2\pi}{\lambda_0} - \frac{2\pi}{\lambda_{ref}})\delta + \varphi(\delta) \qquad (B-4)$$

If we sample the delay with equal interval of time, dt, then we can replace the delay with $\delta = 2v\,dt$, where v is the scanning speed. The first term in (B-4) will be then linear, and its coefficient is given by:

$$\gamma = 4\pi v(\frac{1}{\lambda_0} - \frac{1}{\lambda_{ref}}) \, .$$

Therefore, after we obtain the experimental raw data from phase comparator, we first do a linear fit, and the slope of the fit can be used to deduce the central wavelength λ_0 of the target pulse. The residue value after subtracting the linear fit then gives the $\varphi(\delta)$, the phase term of $I(\delta)$. Amplitude of $I(\delta)$ can be directly obtained from the amplitude of interference signal from the amplified detector.

In Figure B.2, we plot the measurement result of Spectra-Physics Tsunami laser, whose output (about 200 ps) is shown in Figure 4.6. The AOM is driven by a phase lock loop circuit that is designed to lock the frequency at the Tsunami laser's repetition rate, about 80 MHz. By double passing through the AOM, the frequency shift of the shearing laser is about 160 MHz. The estimated spectra width of the optical pulse is 2.2 GHz. The ration between frequency shift and spectra width is about 7%, within the recommended value of typical SPIDER technique [63].

The Fourier transform of auto-correlation data in Figure B.2(a) gives the power spectrum of the optical pulse and the spectral phase. They are shown in Figure B.2(b) and Figure B.2(c).
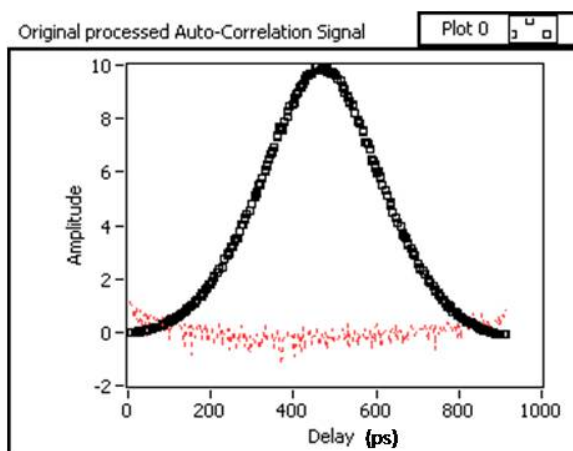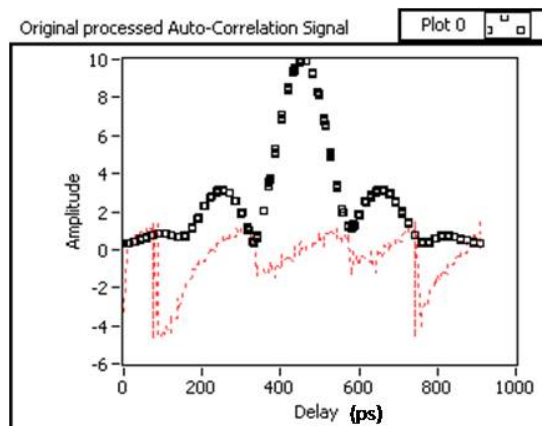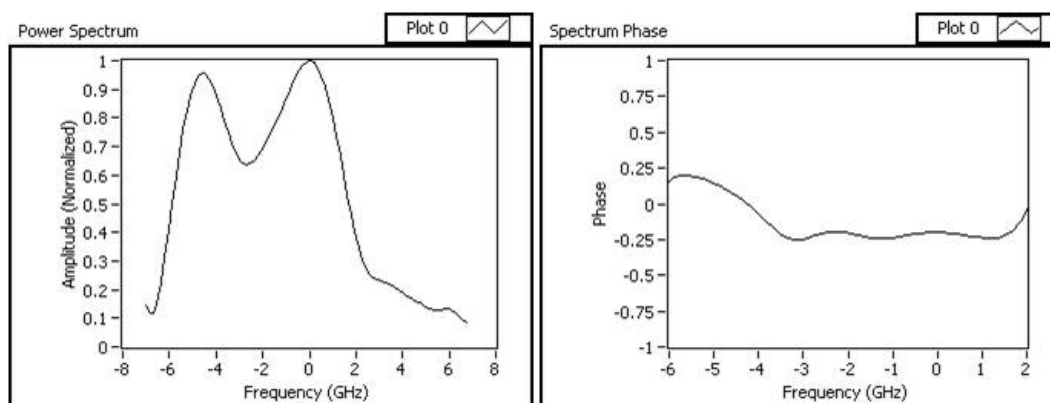
(a)
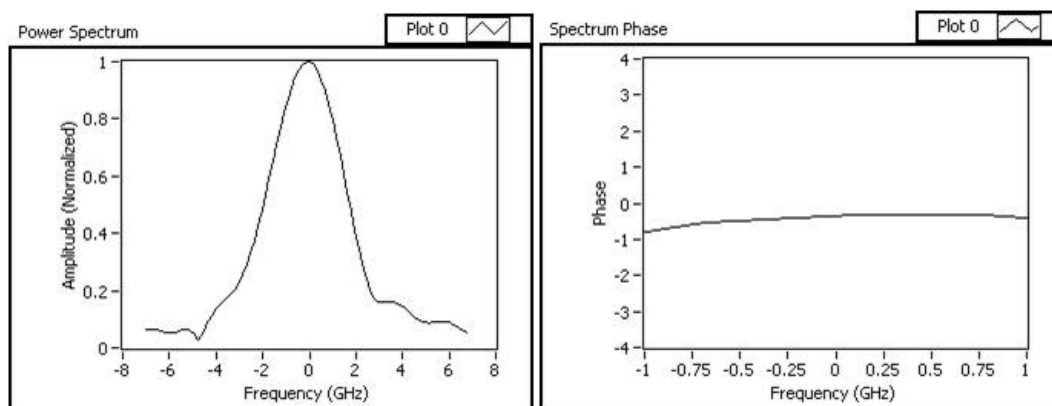
(b)   *(c)*

Figure B.2. Measuring Tsunami's output pulse: (*a*) Auto-correlation amplitude (black curve) and phase (red curve); (*b*) Retrieved power spectrum; (*c*) Spectral phase.

We also tried to measure the same optical pulse after it transmitted through an etalon. The etalon is 6 mm thick, and coated to 90% reflectivity (both sides). The position of etalon was adjusted so that there was minimum optical power transmitted through, measured by a power meter. The experiment result is shown in Figure B.3.

(a)

(b)   *(c)*

Figure B.3. Measuring Tsunami's output pulse after passing through an etalon with minimum transmitting power: (*a*) Auto-correlation amplitude (black curve) and phase (red curve); (*b*) Retrieved power spectrum; (*c*) Spectral phase.

The double-peak structure in retrieved power spectrum (Figure B.3(b)) highly agrees with the etalon's spectral trimming behavior. It can be explained as the peak of the

original optical pulse (Figure B.2(b)) is highly attenuated by the etalon, but its left tail is on resonant with etalon's transmission peak. The retrieved spectral phase (Figure B.3(c)) shows similar flat structure as the one in Figure B.2(c). This is not surprising because etalon in this setting would not introduce any phase change.

We adjusted the position of the etalon so that there was maximum optical power transmitted through it. The measurement result is shown in Figure B.4. Note that we cannot measure the auto-correlation signal with full span of delays, because it was limited by the scanning range of our translational stage.

The power spectrum (Figure B.4-b) we obtained under high transmission condition again agrees with the theoretical predictions. Its width is narrower than the one shown in Figure B.2-b. This is because the slope of the original spectrum is trimmed by the etalon. However, we expect to see a small dip in retrieved spectral phase around zero frequency, but there is no such structure shown in Figure B.4-c. This discrepancy indicates that further improvements in the experimental devices are needed. For example, the scanning speed v of translational stage needs to stay close to constant, and/or the wavelength λ_{eff} of the He-Ne laser needs to be stabilized in a better way.

I would like to thank Dr. Walmsley for useful discussions about SPIDER technique.
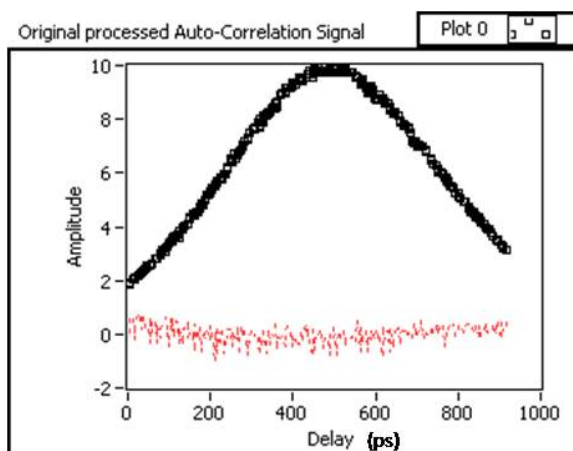
(a)
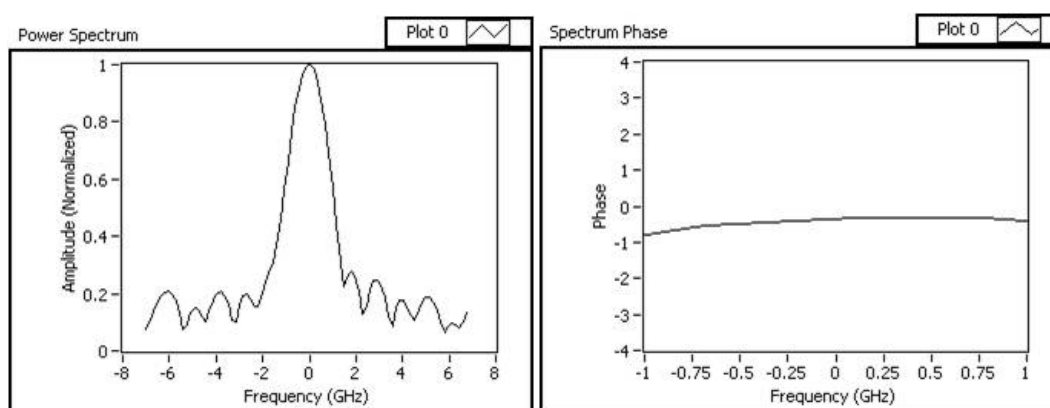
(b)   *(c)*

Figure B.4. Measuring Tsunami's output pulse after passing through an etalon with maximum transmitting power: (*a*) Auto-correlation amplitude (black curve) and phase (red curve); (*b*) Retrieved power spectrum; (*c*) Spectral phase.

BIBLIOGRAPHY

[1] M. Kourogi, K. Nakagawa and M. Ohtsu, "Wide-span optical frequency comb generation for accurate optical frequency difference measurement," IEEE J. Quant. Electron. **29**, 2693-2701 (1993)

[2] H. A. Haus, "Short Pulse Generation," in Compact Sources of Ultrashort Pulses, edit by I. N. Duling III, Cambridge University Press (1995)

[3] D. J. Kuizenga and A. E. Siegman, "FM and AM Mode Locking of the Homogeneous Laser - Part I: Theory," IEEE J. of Quantum Electron. **6**, 694 (1970)

[4] H. A. Haus, "A Theory of Forced Mode Locking," IEEE J. Quant. Electron. **11**, 323 (1975)

[5] T. Udem, J. Reichert, R. Holzwarth, and T. W. Hansch, "Accurate measurement of large optical frequency differences with a mode-locked laser," Opt. Lett. **24**, 881 (1993)

[6] T. Udem, J. Reichert, T. W. Hansch, and M. Kourogi, "Absolute optical frequency measurement of the cesium $D2$ line," Phys. Rev. A **62**, 031801 (2000)

[7] Telle, H. R., G. Steinmeyer, A. E. Dunlop, J. Stenger, D. H. Sutter, and U. Keller, "Carrier-envelope offset phase control: A novel concept for absolute optical frequency control and ultrashort pulse generation," Appl. Phys. B: Lasers Opt. **69**, 327 (1999)

[8] J. Ranka, R. Windeler and A. Stentz, "Visible continuum generation in air-silica microstructure optical fibers with anomalous dispersion at 800 nm," Opt. Lett. **25**, 25 (2000)

[9] S. A. Diddams, D. Jones, Jun Ye, S. Cundiff, J. Hall, J. Ranka, R. Windeler, R. Holzwarth, Th. Udem and T. W. Hansch, "Direct link between microwave and optical frequencies with a 300 THz femtosecond laser comb," Phys. Rev. Lett. **84**, 5102 (2000)

[10] Th. Udem, J. Reichert, R. Holzwarth and T. W. Hansch, "Absolute optical frequency measurement of the Cesium D1 line with a mode-locked laser," Phys. Rev. Lett. **82**, 3568 (1999)

[11] S. A. Diddams, Th. Udem, J. C. Berquist, E. A. Curtis, R. E. Drullinger, L. Hollberg, W. M. Itano, W. D. Lee, C. W. Oates, K. R. Vogel and D. J. Wineland, "An optical clock based on a single trapped $^{199}Hg^{+}$ ion," Science **293**, 825 (2001)

[12] Nobelprize.org

[13] M. Drescher, M. Hentschel, R. Kienberger, G. Tempea, C. Sipelmann, G. A. Reider, P. B. Corkum and F. Krausz, "X-ray pulses approaching the attosecond frontier," Science **291**, 1923 (2001)

[14] P. M. Paul, E. S. Toma, P. Breger, G. Mullot, F. Auge, Ph. Balcou, H. G. Muller and P. Agostini, "Observation of a train of attosecond pulses from high harmonic generation," Science **292**, 1689 (2001)

[15] M Drescher et al, "Time-resolved atomic inner-shell spectroscopy," Nature **419**, 803 (2002)

[16] A. Baltuska, Th. Udem, M. Ulberacker, M. Hentschel, E. Goulielmakis, Ch. Gohle, R. Holzwarth, V. S. Yakovlev, A. Scrinzi, T. W. Hansch and F. Krausz, "Attosecond control of electronic processes by intense light fields," Nature **421**, 611 (2003)

[17] Hiroyuki Kawano, Yasuyuki Hirakawa and Totaro Imasaka, "Generation of High-Order Rotational Lines in Hydrogen by Four-Wave Raman Mixing in the Femtosecond Regime," IEEE J. Quant. Electron. **34**, 260 (1998)

[18] M. Y. Shverdin, D. R. Walker, D. D. Yavuz, G. Y. Yin and S. E. Harris, "Generation of a Single-Cycle Optical Pulse," Phys. Rev. Lett. **94**, 033904 (2005)

[19] Takayuki Suzuki, Masataka Hirai and Masayuki Katsuragawa, "Octave-Spanning Raman Comb with Carrier Envelope Offset Control," Phys. Rev. Lett. **101**, 243602 (2008)

[20] M. G. Raymer, I. A. Walmsley, J. Mostowski and B. Sobolewska, "Quantum theory of spatial and temporal coherence properties of stimulated Raman scattering," Phys. Rev. A **32**, 332 (1985)

[21] I. A. Walmsley and M. G. Raymer, "Observation of Macroscopic Quantum Fluctuations in Stimulated Raman Scattering," Phys. Rev. Lett. **50**, 962 (1983)

[22] C. V. Raman and K. S. Krishnan, "A new type of secondary radiation," Nature **121**, 501 (1928)

[23] G. Placzek, "The Rayleigh and Raman scattering," in Handbuch der Radiologie, Band VI, edited by E. Marx (1934)

[24] G. Eckhardt, R. W. Hellwarth, F. J. McClung, S. Schwarz, D. Weiner and E. Woodbury, "Stimulated Raman scattering from organic liquids," Phys. Rev. Lett. **9** 455, (1962)

[25] D. J. Gardiner, "Practical Raman spectroscopy," Springer-Verlag (1989)

[26] Y. R. Shen, "Quantum statistics of nonlinear optics," Phys. Rev. **155**, 921 (1967)

[27] M. G. Raymer and I. A. Walmsley, "The quantum coherence properties of stimulated Raman scattering," in Progress In Optics, edited by E. Wolf, Vol. XXVIII, 180 (1990)

[28] Walmsey and M. G. Raymer, "Experimental study of the macroscopic quantum fluctuations of partially coherent stimulated Raman scattering," Phys. Rev. A **33**, 382 (1986)

[29] L. M. Duan, M. D. Lukin, J. I. Cirac and P. Zoller, "Long-distance quantum commnunication with atomic ensembles and linear optics," Nature **414**, 413 (2001)

[30] C. H. van der Wal, M. D. Eisaman, A. Andre, R. L. Walsworth, D. F. Phillips, A. S. Zibrov and M. D. Lukin, "Atomic memory for correlated photon states," Science **301**, 196 (2003)

[31] C. W. Chou, H. de Riedmatten, D. Felinto, S. V. Polyakov, S. J. van Enk and H. J. Kimble, "Measurement-induced entanglement for excitation stored in remote atomic ensembles," Nature **438**, 828 (2005)

[32] T. Chaneliere, D. N. Matsukevich, S. D. Jenkins, S. Y. Lan, R. Zhao, T. A. B. Kennedy and A. Kuzmich, "Quantum interference of electromagnetic fields from remote quantum memories," Phys. Rev. Lett. **98**, 113602 (2007)

[33] S. Harris, "Electromagnetically Induced Transparency," Physics Today **50**, 36 (1997)

[34] K. F. Reim, J. Nunn, V. O. Lorenz, B. J. Sussman, K. C. Lee, N. K. Langford, D. Jaksch and I. A. Walmsley, "Towards high-speed optical quantum memories," Nature Phtonics **4**, 218 (2010)

[35] S. E Harris and A. V. Sokolov, "Subfemtosecond Pulse Generation by Molecular Modulation," Phys. Rev. Lett. **81**, 2894 (1998)

[36] W. Chen, Zhi-Ming Hsieh, Shu Wei Huang, Hao-Yu Su, Chien-Jen Lai, Tsung-Ta Tang, Chuan-Hsien Lin, Chao-Kuei Lee, Ru-Pin Pan, Ci-Ling Pan and A. H. Kung, "Sub-Single-Cycle Optical Pulse Train with Constant Carrier Envelope Phase," Phys. Rev. Lett. **100**, 163906 (2008)

[37] Zhi-Ming Hsieh, Chien-Jen Lai, Han-Sung Chan, Sih-Ying Wu, Chao-Kuei Lee, Wei-Jan Chen, Ci-Ling Pan, Fu-Goul Yee, and A. H. Kung, "Controlling the Carrier-Envelope Phase of Raman-Generated Periodic Waveforms," Phys. Rev. Lett. **102**, 213902 (2009)

[38] F. Couny, F. Benabid and P. S. Light, "Large-pitch Kagome-structured hollow-core photonic crystal fiber," Optics Letters **31**, 3574 (2006)

[39] F. Couny, F. Benabid, P. J. Roberts, P. S. Light and M. G. Raymer, "Generation and Photonic Guidance of Multi-Octave Optical Frequency Combs," Science **318**, 1118 (2007)

[40] M. G. Raymer and J. Mostowski, "Stimulated Raman scattering: Unified treatment of spontaneous initiation and spatial propagation," Phys. Rev. A **24**, 1980 (1981)

[41] Hermann A. Haus, "Electromagnetic Noise and Quantum Optical Measurements," Springer (2000), Chapter 12

[42] W. Wasilewski and M. G. Raymer, "Pairwise entanglement and readout of atomic-ensemble and optical wave-packet modes in travelling wave Raman interactions," Phys. Rev. A **73** 063816 (2006)

[43] J. S. Bell, "Speakable and unspeakable in quantum mechanics," Cambridge University Press (1987)

[44] E. Shchukin and W. Vogel, "Universal measurement of quantum correlations of radiation," Phys. Rev. Lett. **96**, 200403 (2006)

[45] W. Ji, C. Wu, S. J. van Enk and M. G. Raymer, "Mesoscopic entanglement of atomic ensembles through nonresonant stimulated Raman scattering", Phys. Rev. A **75**, 052305 (2007)

[46] D. T. Smithey, M. Beck, M. G. Raymer and A. Faridani, "Measurement of the Wigner distribution and the density matrix of a light mode using optical homodyne tomography: Application to squeezed states and the vacuum," Phys. Rev. Lett. **70**, 1244 (1993)

[47] M. G. Raymer, "Quantum state entanglement and readout of collective atomic-ensemble modes and optical wave-packets by stimulated Raman scattering," J. Mod. Optics, **51**, 1739–1759 (2004)

[48] S. Ya. Kilin, "Transient Anti-Stokes Stimulated Raman Scattering: the Possibility of Observing Quantum Macroscopic Fluctuations," Europhys. Lett. **5**, pp 419-424 (1988)

[49] M. D. Duncan, R. Mahon, J. Reintjes and L. L. Tankersley, "Parametric Raman gain suppression in D_2 and H_2," Optics Letters **11**, 803 (1986)

[50] M. Belsley, D. T. Smithey, K. Wedding and M. G. Raymer, "Observation of extreme sensitivity to induced molecular coherence in stimulated Raman scattering," Phys. Rev. A **48**, 1514 (1993)

[51] S.J. Kuo, D.T. Smithey, and M.G. Raymer, "Spatial Interference of Macroscopic Light Fields from Independent Raman Sources, " Phys. Rev. A (Rapid Commun.) **43**, 4083 (1990)

[52] I. A. Walmsley, M. G. Raymer, T. Sizer II, I. N. Duling III and J. D. Kafka, "Stabilization of Stokes pulse energies in the nonlinear regime of stimulated Raman scattering," Opt. Commun. **53**, 137 (1985)

[53] C. Wu, M. G. Raymer, Y. Y. Wang and F. Benabid, "Quantum theory of phase correlations in optical frequency combs generated by stimulated Raman scattering," to be published in Phys. Rev. A (2010)

[54] Robert W. Boyd, "Nonlinear Optics," Academic Press 2003, Chapter 10

[55] Supporting online material for reference 37

[56] J. Mostowski and M. G. Raymer, "Quantum Statistics in Nonlinear Optics," Chapter 5 in "Contemporary Nonlinear Optics," Edited by G. P. Agrawal and R. W. Boyd, Academic Press (1992)

[57] J. C. Knight, T. A Birks, P. St. J. Russell and D. M. Atkin, "All-silica single-mode optical fiber with photonic crystal cladding," Optics Letters **21**, 1547 (1996)

[58] R. F. Cregan, B. J. Mangan, J. C. Knight, T. A. Birks, P. St. J. Russell, P. J. Roberts and D. C. Allan, "Single-mode photonic band gap guidance of light in air," Science **285**, 1537 (1999)

[59] J. H. Neumann and E. Wigner, "On the behavior of eigenvalues in adiabatic processes," Phys. Z. **30**, 465 (1929)

[60] F. H. Stillinger, D. R. Herrick, "Bound state in the continuum," Phys. Rev. A **11**, 446 (1975)

[61] Andrew Funk Ph. D. Dissertation, University of Oregon library (2004)

[62] P. Lallemand, P. Simova and G. Bret, "Pressure-induced line shift and collisional narrowing in hydrogen gas determined by stimulated Raman emission," Phys. Rev. Lett. **17**, 1239 (1966)

[63] F. Benabid, G. Antonopoulos, J. C. Knight and P. St. J. Russell, "Stokes Amplification Regimes in Quasi-cw Pumped Hydrogen-Filled Hollow-Core Photonic Crystal Fiber," Phys. Rev. Lett. **95**, 213903 (2005)

[64] Mandel and Wolf, "Optical coherence and quantum optics," Cambridge University Press (1995)

[65] Hiroyuki Otsuka, Tomohiro Uchimura, and Totaro Imasaka, "Phase locking in four-wave Raman mixing for generation of an ultrashort laser pulse," OPTICS LETTERS **29**, 400 (2004)

[66] Y. Y. Wang, F. Couny, P. S. Light and F. Benabid, "Self and Mutual Coherence of Raman Frequency Comb Generated in Large Pitch HC-PCF Filled With H_2," CLEO/QELS 2009 (CTuB4)

[67] Chunbai Wu, Erin Mondloch, M. G. Raymer, Y. Y. Wang, F. Couny and F. Benabid, "Spontaneous phase anti-correlations in Raman optical frequency comb generation," CLEO/QELS 2010 (QTuA5)

[68] D. Kane and R. Trebino, "Characterization of arbitrary femtosecond pulses using frequency-resolved optical gating," IEEE J. Quant. Electron. **29**, 571 (1993)

[69] C. Iaconis and I. A. Walmsley, "Self-referencing spectral interferometry for measuring ultrashort optical pulses," IEEE J. Quant. Electron. **35**, 501 (1999)